1 UNIVERSITY OF CALIFORNIA, SAN DIEGO

2 **Characterization and Modeling of Ion Transport Kinetics in p-Si Photovoltaic Modules**

3 A dissertation submitted in partial satisfaction of the
4 requirements for the degree
5 Doctor of Philosophy

6 in

7 NanoEngineering

8 by

9 Erick Rolando Martinez Loran

10 Committee in charge:

11 Professor Prabhakar R. Bandaru, Chair
12 Professor David P. Fenning, Co-Chair
13 Professor Shadi Dayeh
14 Professor Oscar Vazquez-Mena
15 Professor Javier Garay
16

17 2020

18 Copyright

19 Erick Rolando Martinez Loran, 2020

20 All rights reserved.

21
22
23
24

The dissertation of Erick Rolando Martinez Loran is approved, and it is acceptable in quality and form for publication on microfilm:

____

____

____

____
Co-Chair

____
Chair

University of California, San Diego

2020

DEDICATION

25 To my family, who has supported me through this journey.

EPIGRAPH

The world stands out on either side

No wider than the heart is wide;

Above the world is stretched the sky,–

No higher than the soul is high.

—Edna St. Vincent Millay

TABLE OF CONTENTS

32 Signature Page iii

33 Dedication iv

34 Epigraph v

35 Table of Contents vi

36 List of Figures xii

37 Acknowledgements xiv

38 Vita and Publications xvi

39 Abstract xviii

40 Chapter 1 Introduction 1
41 1.1 What is Potential-Induced Degradation? 2
42 1.2 Root cause of PID 4
43 1.3 Origin of Na contamination 5
44 1.4 Electric Potential in the module 6
45 1.5 Sodium Transport 7
46 1.6 Summary 8

47 Chapter 2 Na transport kinetics in the module stack 9
48 2.1 Approximate voltages in the module stack 10
49 2.2 Transport of Na in EVA 11
50 2.2.1 Experiment 12
51 2.2.2 Results 12
52 2.3 Summary 14

53 Chapter 3 Transport of Na in SiN_x 15
54 3.1 Characterization of drift-diffusion kinetics using C-V measurements . . 16
55 3.2 Trap-corrected bias-temperature-stress method 16
56 3.2.1 Flatband fitting 17
57 3.3 Kinetics of ion diffusion and drift in SiN_x 18
58 3.4 Experiment 20
59 3.5 Results 22
60 3.6 Characteristic Na^+ transit time 25
61 3.7 Conclusions 27

62 Chapter 4 Finite Element Model of Mobile-Ion Kinetics . . . 29
63 4.1 Modeling mobile charge kinetics in MIS structures . . . 30
64 4.2 Finite Element Method Implementation of the PNP coupled system . . 32
65 4.3 Modeling charge transport in SiO_2 . . . 34
66 4.4 Behavior before the characteristic transit time . . . 40
67 4.5 Na transport in stacks of materials . . . 41
68 4.6 Conclusions . . . 45

69 Chapter 5 Device degradation modeling . . . 46
70 5.1 Introduction . . . 46
71 5.2 Modeling Na migration kinetics . . . 50
72 5.3 Device simulations . . . 52
73 5.4 Bounding the value of the diffusion coefficient of Na in the SF . . . 56
74 5.5 Finite Source Analysis . . . 59
75 5.6 Summary . . . 67

76 Chapter 6 Summary and Suggestions for Future
77 Work . . . 69
78 6.1 Applications of PID kinetics quantification and modeling . . . 70
79 6.2 Future work . . . 71
80 6.2.1 Quantification of composition-dependent transport in SiN_x . . . 71
81 6.2.2 Incorporation of environmental factors . . . 71
82 6.2.3 Three-dimensional considerations . . . 72
83 6.2.4 PID-recovery . . . 72
84 6.2.5 Incorporation of SiN_x trap kinetics . . . 73

85 Appendix A Derivation for the characteristic time for drift-diffusion . . . 75

86 Appendix B Derivation of the spatial part of Nernst-Planck equation in the weak form . . 77

87 Appendix C Derivation of the TR-BDF2 time-stepping in the weak form . . . 80

88 Appendix D Writing the weak form of Laplacian terms . . . 82

89 References . . . 83

List of Abbreviations

AC Alternating current.

Al-BSF Aluminum back-surface field.

ARC Anti-reflective coating.

BTS Bias-temperature-stress.

C-V Capacitance-voltage.

DC Direct current.

EDX Energy dispersive X-ray spectroscopy.

EVA Ethylene-vinyl acetate.

FEM Finite element method.

HRTEM High-resolution transmission electron microscopy.

J-V Current-density-voltage.

MIS Metal-insulator-semiconductor.

n-Si *n*-type silicon.

n-Si *p*-type silicon.

n^+-Si Highly-doped *n*-type silicon.

PDE Partial differential equation.

PECVD Plasma-enhanced chemical vapor deposition.

PID Potential-induced degradation.

PID-s Potential-induced degradation of the shunting type.

PNP Poisson-Nernst-Planck.

PV Photovoltaic.

SF Stacking Fault.

SIMS Secondary-ion mass spectroscopy.

ToF-SIMS Time-of-flight secondary-ion mass spectroscopy.

XPS X-ray photoelectron spectroscopy.

List of Symbols

ϵ_0	Permittivity of free space
ϵ_r	Relative permittivity
μ	Mobility (ionic or electronic)
∇	The Nabla operator
ϕ	Electric Potential
$\mathbf{E}$	Electric field
C	Concentration
k_B	Boltzmann's constant
q	Elementary charge
Q_S	Image charge in the semiconductor.
R_{sh}	Shunt resistance
T	Temperature
V	Voltage

130 V_{FB} Flatband voltage

LIST OF FIGURES

131 Figure 1.1: Schematic of a PID degraded silicon solar panel 3
132 Figure 1.2: *J-V* signature of a p-Si module affect by PID-s. 4
133 Figure 1.3: Stacking fault decoration schematic illustrating the mechanism behind shunt-
134 ing in p-Si devices. 5
135 Figure 1.4: Schematic of a voltage divider model corresponding to the stack of materials
136 at the front of Si solar module. 7

137 Figure 2.1: Schematic of transport of Na across the different materials in the module stack 10
138 Figure 2.2: Representative Na drift-diffusion profile obtained by SIMS of a metal-EVA-
139 metal structure intentionally contaminated with Na 13

140 Figure 3.1: Schematic of the BTS setup used to quantify Na^+ migration in SiN_x. 20
141 Figure 3.2: Flatband shift as a function of time and temperature with and without the
142 trapping correction 23
143 Figure 3.3: Arrhenius relationship for the diffusivity of Na^+ in SiN_x evaluated by the
144 trapping-corrected BTS method 25
145 Figure 3.4: Characteristic Na transit time in a 65 nm-thick SiN_x film as a function of the
146 module temperature and electric field across the dielectric. 26

147 Figure 4.1: Simulated image charge in the semiconductor of a MIS structure as a function
148 of time. 35
149 Figure 4.2: Selected concentration profiles corresponding to the image charge plotted in
150 Fig. 4.1. 37
151 Figure 4.3: Simulated V_{FB} as a function of time for a SiO_2 MIS structure 38
152 Figure 4.4: Concentration profiles as a function o f time, as modeled by (a) a FEM sim-
153 ulation of the full Poisson-Nernst-Planck coupled system (PNP) and (b) the
154 approximate solution at short times 41
155 Figure 4.5: Simulated concentration profiles as a function of time across a SiN^x/Si mate-
156 rial stack. 44

157 Figure 5.1: Proposed modeling framework aimed at predicting PID-s and engineering
158 PID-robust PV modules. 47
159 Figure 5.2: Boundary conditions used for Na transport simulations in p-Si PV modules. . 49
160 Figure 5.3: Schematic of the Aluminum Back Surface used to simulate the module degra-
161 dation. 51
162 Figure 5.4: Schematic of a metallic shunt introduced in the n^+-Si emitter of the PV module
163 to model PID-s 54
164 Figure 5.5: Simulated PID-s kinetics degradation for device stressed at 85 °C under a
165 voltage equivalent to 0.5 $MV\,cm^{-1}$ 55
166 Figure 5.6: Simulated PID-s progression as a function o Na diffusivity in the stacking fault 57
167 Figure 5.7: Arrhenius relationship for the diffusion coefficient of Na in Si, as estimated
168 from fitting SIMS profiles of thermally diffused Na in n-Si wafers 57
169 Figure 5.8: Simulated PID-kinetics as a function of D_{SF} (indicated by the color scale). . . 61

170 Figure 5.9: Simulated PID-kinetics as a function of the surface concentration of Na at the
171 source S (indicated by the color scale). 62
172 Figure 5.10: Simulated PID-kinetics as a function of the rate of ingress of Na at the source
173 k (indicated by the color scale) 62
174 Figure 5.11: Simulated PID-kinetics as a function of the magnitude of the electric field in
175 SiN_x E (indicated by the color scale). 63
176 Figure 5.12: Simulated PID-kinetics as a function of the magnitude of the surface mass
177 transfer coefficient h at the SiN_x/Si interface (indicated by the color scale). . . . 64
178 Figure 5.13: Estimated time required to reach a 5 % performance degradation in a p-Si
179 PV module due to potential induced degradation as a function of the transport
180 parameters. 65

ACKNOWLEDGEMENTS

I would like to express my gratitude to all the people who contributed to this work.

In the first place, I would like to acknowledge my co-advisors Professor David P. Fenning and Prof. Prabhakar Bandaru for their support and guidance during the course of my doctoral program. I am thankful as well with my committee members for their valuable feedback.

I am specially grateful with the National Council of Science and Technology in Mexico (CONACyT) and The University of California Institute for Mexico and the United States (UC MEXUS) for the doctoral fellowship I was awarded with, which supported me through the PhD program. In the same way, I am grateful with the Department of Energy (DOE) and the Solar Energy Technology Office (SETO) for providing funding for this project and awarding me with a Graduate Student Researcher position that financed me through the final stages of my PhD.

I would also like to express my gratitude to the collaborators at Arizona State University, Mariana Bertoni and Rico Meier who made this work possible. I would like to specially thank Guillaume von Gastrow, who has been instrumental in many levels to this work and, Jacob Clenney for all the support in sample preparation and characterization.

I would like to acknowledge all the people that made contributions to this work in all capacities. Among them Jonathan Scharf, whose contribution has been catalytic to the project; Rishi Kumar for all the help with the hardware in the lab; Maryam Sarkhoush for all the assistance to configure the environment for the device simulations. Nirjhar Sarkar and Serdar Yavuz for being restless minds, always open to discuss and do research; all Fenning Lab members: Pedram Abassi, Deniz Cakan, Taewoo Kim, Moses Kodur, Xueying Li, Grace Luo, Manas Likhit, Aditi Mhatre, Shreya Rengarajan, Ethan Jing, Zachary Dorfman, Tulika Rastogi and Ernesto Magaña, for all the

useful input during group discussions; all Bandaru Lab members: Anna Alexander, Peng Chen, Yongliang Dong, Bei Fan, Hidenori Yamada, Zichen Zhang for their thoughtful insights during group meeting presentations. Special thanks to Flavio Fernando Contreras Torres for the most fruitful discussions and collaborative work, and to Leonid Serkin for proof-reading this manuscript.

I would also like to thank all the people that, though not directly have made this enterprise possible and joyful. Thank you Alireza Kargar, Fatih Canbazoglu, Rajaram Narayanan, Cihan Kuru.

I am extremely thankful with my most cherished friends, Adrian, Benjamin, Flavio, Leonid, Luis, Paco, Victor, and many others who have shared their wisdom and ears all these years.

Finally, I would like to thank, in a very special way my parents who have supported me through all the stages of this journey, my life partner Barbra and our boy, Oren. You make all this effort worthwhile.

VITA

2012	B. S. in Physics, Universidad Nacional Autónoma de México
2014	M. S., in Materials Science and Engineering, Universidad Nacional Autónoma de México
2020	Ph. D. in NanoEngineering, University of California, San Diego

PUBLICATIONS

1. **E. Martinez-Loran**. G. von Gastrow, J. Clenney, R. Meier, P. Bandaru, Mariana I. Bertoni, D.P. Fenning. under the title “Finite Element Simulation of Potential Induced Degradation Kinetics in p-Si Solar Modules”, *IEEE . Photovolt.* (In Preparation), (2020)

2. **E. Martinez-Loran**, G. von Gastrow, J. Clenney, J. D. Scharf, R. Meier, M. Bertoni, D. Fenning, and P. Bandaru, “Numerical solution to Poisson-Nernst-Planck equations for ion transport in MIS structures and solar cells”, *J. Appl. Phys.* (In Preparation), (2020).

3. G. von Gastrow, **E. Martinez-Loran**†, J. Scharf, J. Clenney, R. Meier, P. Bandaru, M. Bertoni, and D. Fenning, “Quantification of sodium ion migration in SiN_x by flatband-potential monitoring atdevice operating temperatures”, *Phys. Status Solidi A.* (2020).

4. D. Ban, Y. Liu, Z. Wang, S. Ramachandran, N. Sarkar, Z. Shi, W. Liu, A. Karkisaval, **E. Martinez-Loran**, F. Zhang, G. Glinskii, P. Bandaru, C. Fan, and R. Lal, “Direct DNA Methylation Profiling with an Electric Biosensor”, *ACS Nano* **14**, 6743–6751 (2020).

5. E. Alvarez-Zauco, H. Sobral, and **E. Martinez-Loran**, “Morphological, optical and electrical characterization of the interfaces in fullerene-porphyrin thin films”, *J. Nanosci. Nanotechnol.* **20**, 1732-–1739 (2020).

6. G. v. Gastrow, J. Scharf, J. Clenney, **E. M. Loran**, R. Meier, M. I. Bertoni, and D. P. Fenning,“Evaluation of carrier trapping in SiN_x towards ion migration measurements”, in *2019 IEEE 46th Photovoltaic Specialists Conference (PVSC)* (2019), pp. 2017–2020.

7. S. Yavuz, **E. M. Loran**†, N. Sarkar, D. P. Fenning, and P. R. Bandaru, “Enhanced environmental stability coupled with a 12.5% power conversion efficiency in an aluminum oxide-encapsulated n-graphene/p-silicon solar cell”, *ACS Appl. Mater. Interfaces* **10**, 37181–37187 (2018).

8. T. Kim, A. Kargar, Y. Luo, R. Mohammed, **E. Martinez-Loran**, A. Ganapathi, P. Shah, and D. P.Fenning, “Enhancing C_2-C_3 production from CO_2 on copper electrocatalysts via a potential-dependent mesostructure”, *ACS Appl. Energy Mater.* **1**, 1965–1972 (2018).

9. F. F. Contreras-Torres, A. Rodriıguez-Galvan, C. E. Guerrero-Beltran, **E. Martinez-Loran**, E.V Vazquez-Garza, N. Ornelas-Soto, and G. Garcia-Rivas, “Differential cytotoxicity and internalization of graphene family nanomaterials in myocardial cells”, *Materials Science and Engineering*: **C73**, 633–642 (2017).

10. A. Rodriguez-Galvan, **E. Martinez-Loran**, J. J. Naveja, N. Ornelas-Soto, V. A. Basiuk, and F. F. Contreras-Torres, “In-situ metallization of thermally-treated tobacco mosaic virus using silver-nanoparticles”, *J. Nanosci. Nanotechnol.* **16**, 4740–4747 (2017).

11. M. Rodriguez-Delgado, N. Ornelas-Soto, **E. Martinez-Loran**, C. Hernandez-Luna, A. Garcia-Garcia, and F. F. Contreras-Torres, “Enhanced enzymatic activity of laccase (from *Pycnoporus sanguineus* CS43) immobilized on sputtered nanostructured gold thin films”, *J. Nanosci. Nanotechnol.* **17**, 939–946 (2017).

12. J. J. Naveja, F. F. Contreras-Torres, A. Rodriguez-Galvan, and **E. Martinez-Loran**, “Computational simulation of tumor surgical resection coupled with the immune system response to neoplastic cells”, *Journal of Computational Medicine*, N/A (2014).

13. F. F. Contreras-Torres and **E. Martinez-Loran**, “DNA insertion in and wrapping around carbon nanotubes”, *WIREs Comput Mol Sci* **1**, 902–919 (2011).

13. **E. Martinez-Loran**, E. Alvarez-Zauco, V. A. Basiuk, E. V. Basiuk, and M. Bizarro, “Fullerenethin films functionalized by 1,5-diaminonaphthalene: preparation and properties”, *J. Nanosci.Nanotechnol.* **11**, 5569–5573 (2011)

† The author of this Thesis/Dissertation was co-first author in this publication

ABSTRACT OF THE DISSERTATION

Characterization and Modeling of Ion Transport Kinetics in p-Si Photovoltaic Modules

by

Erick Rolando Martinez Loran

Doctor of Philosophy in NanoEngineering

University of California San Diego, 2020

Professor Prabhakar R. Bandaru, Chair

Though generally reliable, silicon solar modules can be subject to unforeseen degradation, leading to a duty life shorter than the expected 25-year life cycle. Potential-induced degradation (PID) has proven difficult to characterize and study. This dissertation is dedicated to developing a physical model to understand the kinetics of PID of the shunting type, and explain the factors that may lead to the design of PID-robust modules.

A bias-temperature stress (BTS) methodology to study ion migration in dielectric films is presented, which accounts for the contribution of bulk traps in the dielectric. Using this method, an Arrhenius relationship for the diffusivity of Na^+ in SiN_x is determined, for which the prefactor is $D_0 = 1.4 \times 10^{-14}\,\mathrm{cm^2/s}$, and the activation energy is $E_a = 0.14\,\mathrm{eV}$, with a 95 % confidence interval of [0.07, 0.21] eV. Based on this result, we bound the transit time of sodium ions, through highly resistive SiN_x anti-reflective coatings, within 1 h and 2 d, under temperature and electric fields relevant to PV operation.

A numerical solution to the coupled Poisson-Nernst-Planck system of equations is presented, based on the finite element method (FEM), that can accurately simulate ionic transport in dielectrics and stacks of materials. The FEM implementation adequately describes the accumulation of charge in the semiconductor interface of metal-insulator-semiconductor capacitors (MIS). Using this model, we evaluate diffusion coefficients of Na^+ in SiO_2 under BTS conditions.

A methodology to simulate PID degradation in PV modules is derived, which uses the result from the ion transport model to simulate the characteristic J-V of the devices. PID is adequately described by the presence of metallic shunt at the *p*-*n* junction of the cell, for which, the metal conductivity depends on the sodium concentration. An upper bound for the diffusivity of Na in stacking faults that result in PID is estimated to be $10^{-14}\,\mathrm{cm}^2/\mathrm{s}$, based on comparison of the simulated PID time series with experimental reports of PID-s.

1 | Introduction

The photovoltaic industry has made outstanding progress over the last decades to bring the promise of a low-carbon economy closer than ever. One of the main advantages of photovoltaic energy is the low cost of operation inherent to silicon photovoltaic (PV) modules, which largely compensates for the considerable initial investment of solar developments. Silicon PV modules are required to operate with minimal power degradation over an average lifespan of 25 years in order to meet commercial warranties [1, 2]. Driven by this concern, reliability studies have become a subject of interest. Several procedures have been developed to test the reliability of modules under normal operation and under accelerated conditions. The latter are devised to forecast the performance of PV modules over the course of many years; provided that the acceleration protocols adequately relate to long term PV module operation. While some of the mechanisms of degradation seem evident (e.g. mechanical failure, loss of transparency of the encapsulant, delamination, shattering, among others) and have been addressed, the type of degradation studied in this dissertation is intrinsically more complex and remediation requires comprehensive knowledge of the properties of all the materials in the module.

A brief introduction on potential-induced degradation of the shunting type is be given in this chapter, followed by an overview, in chapter 2, of the transport of Na in PV modules.

In chapter 3, a quantification methodology for the transport of Na in silicon nitride (SiN_x) is be presented. It is be shown that, for low ionic concentrations with respect to the applied electric stress, the kinetics of Na transport can be described as a diffusion-advection problem. A methodology to quantify ion migration in SiN_x metal-insulator-semiconductor (MIS) capacitors is be demonstrated. A detailed analysis on the characteristic transit time is be presented, beyond which accumulation at the semiconductor interface occurs and leakage of Na to the silicon can occur at a larger scale.

In chapter 4, a finite element solution to the coupled Poisson-Nernst-Planck system of equations is derived, which is used to model transport of charged species in metal-insulator-semiconductor devices and other stacks of materials, beyond the assumptions of low contaminant concentration with respect to the applied electrical stress. A comparison with experimental data is given which agrees well with the predictions of the model.

In chapter 5, a modeling framework is presented, which mechanistically describes the kinetics of PID-s degradation in p-Si modules, based on the bill of materials in the PV module and the operating conditions. Based on the results of the model, and comparison with PID reports, an upper bound for the diffusion coefficient of Na in the stacking fault is be estimated.

1.1 What is Potential-Induced Degradation?

Solar panels incorporate several individual solar cells connected in series, in order to achieve typical load requirements of several hundreds to thousands of volts. Fig. 1.1, shows a simplified schematic of a solar module, where each individual cell is connected in series to achieve a load of 1000 V. As these devices are mounted on a metal frame that is grounded, the voltage

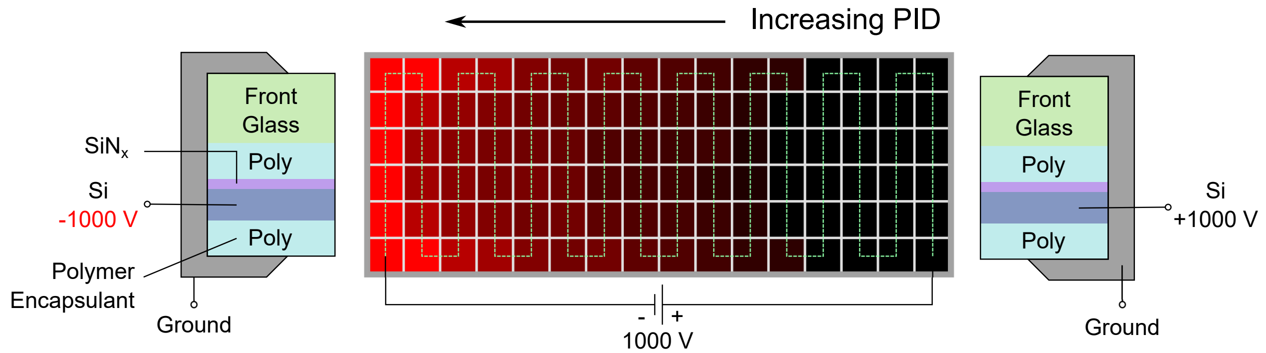

Figure 1.1: Schematic of a PID degraded silicon solar module. Reliability tests reveal that several cells close to the frame on the side of the string with negative floating polarity, are subject PID failure.

332 differential between the metal frame ($V = 0$) and the floating potential of the cells becomes con-
333 siderable at the extremes of the array. Also in Fig. 1.1, a simplified schematic of the cross-section
334 of a mono-facial module is shown, consisting of a solar cell with a SiN_x anti-reflective coating
335 (ARC), encapsulated within a polymer (typically ethylene-vinyl acetate or EVA), and a glass win-
336 dow on the front side, usually made from soda lime glass. It has been observed that the cells
337 subject to a more negative potential with respect to the metal frame suffer from degradation in the
338 output power [3–5]. This degradation mode is called potential-induced degradation (PID) and is
339 known to affect *n*-type silicon (n-Si) and *p*-type silicon (n-Si) devices differently. In the n-Si case,
340 it has been reported that degradation is the result of surface polarization and is almost completely
341 reversible [6], whereas in p-Si, the degradation is due to a reduction in the shunt resistance R_{sh} of
342 the device [5] as is illustrated in Fig 1.2. While recovery has been documented for p-Si modules
343 affected by PID [5, 7–15], in general, only partial recovery is observed, and it requires the appli-
344 cation of a temperature stress and/or inverting the polarity of the voltage between the cell and the
345 frame. This makes the study of this type degradation on p-Si of special interest, and is the focus of
346 this research.

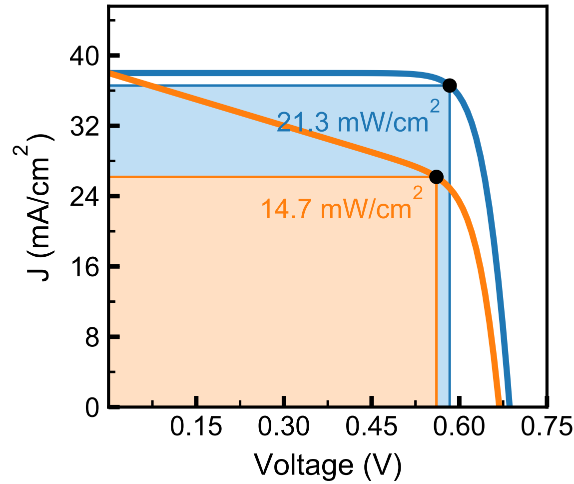

Figure 1.2: *J-V* signature of a p-Si module affect by PID-s.

347 PID in p-Si occurs as a result of several factors facilitating the formation of electrical shunts
348 in the emitter of the device. Initial investigations suggested corrosion played an important role in
349 degradation [3], which led to the characterization of leakage currents across the module stack,
350 aimed at determining the physical pathways of the degradation process [5, 6, 16, 17]. These
351 experiments helped to identify ionic currents and, particularly, sodium ions (Na^+) as the main
352 factor involved in PID in p-Si solar modules [17, 18].

353 1.2 Root cause of PID

354 The mechanism by which Na induces shunting has been elucidated by a combination of en-
355 ergy dispersive X-ray spectroscopy (EDX) and high-resolution transmission electron microscopy
356 (HRTEM) studies performed at the Fraunhoffer Center for Silicon Photovoltaics, which showed
357 incorporation of Na inside stacking faults (SFs) in the silicon emitter, on severely shunted regions
358 of PID-affected devices [9, 12, 13, 19]. These findings indicate that Na introduces a large con-

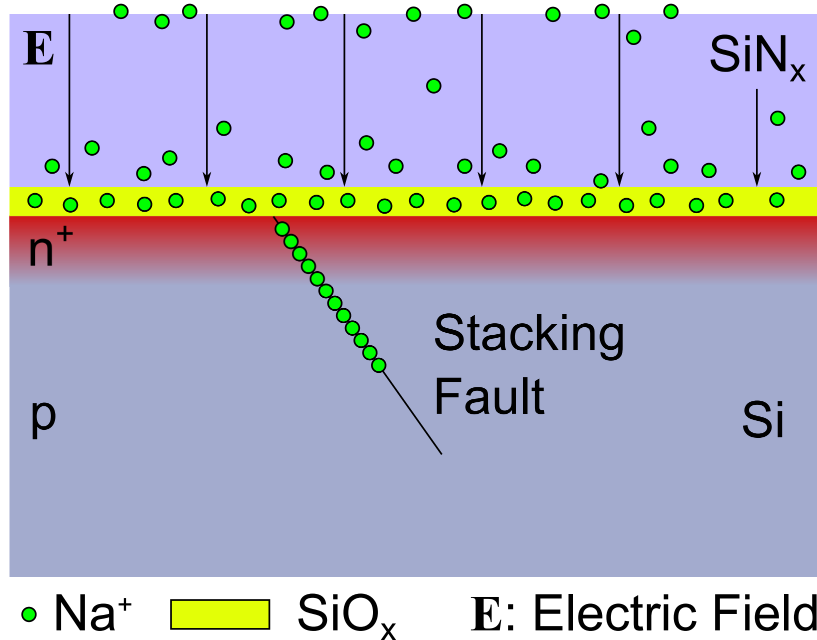

Figure 1.3: Stacking fault decoration schematic illustrating the mechanism behind shunting in p-Si devices. Adapted from Ref. [12]

359 centration of defect states in the band energy diagram, within the p-n junction of a solar cell,
360 which induce undesirable recombination. These defects are ultimately responsible for a substan-
361 tial decrease in R_{sh} [9]. The mechanism is illustrated in Fig. 1.3, where it is depicted how ionic
362 Na is transported through the SiN_x anti-reflective coating of the module, driven by the electric
363 field. Then, a large concentration of Na builds up at the interfacial silicon oxide film, followed
364 by in-diffusion to the stacking faults in the silicon emitter. Once a critical concentration of Na is
365 accumulated in the SF, the defect results in shunting of the junction of the solar cell. Therefore this
366 mode of degradation is referred to as PID of the shunting type or PID-s.

367 1.3 Origin of Na contamination

368 The front cover glass has been pointed out as the most likely source of Na ions in the mod-
369 ule stack [7, 18, 20, 21], mediated by an activation process involving temperature and humidity

370 [21, 22]. Nevertheless, PID-s has been reported to occur in the absence of a front cover glass
371 [23] and even in the absence of the polymer encapsulant, when the electric field is supplied by a
372 corona discharge [24, 25]. Evidence of Na contamination has been reported within the EVA poly-
373 mer encapsulant specially close to the surface of SiN_x [26]. This suggests that Na contamination
374 introduced during the module lamination. Nevertheless, introduction of Na contamination from
375 the front cover glass can not be ruled out, especially in combination with high contents of moisture
376 and elevated temperatures.

377 1.4 Electric Potential in the module

378 The magnitude of the electric field in the module stack and, specifically in the SiN_x film
379 determines to a large extent the ingress of Na in the emitter of the device and hence, susceptibility
380 to PID-s. The potential drop across the module stack has been explained by a voltage divider model
381 [27]. This model assumes that the main path of current occurs through a circuit of series resistors
382 corresponding to the glass, polymer encapsulant, and SiN_x layers, as shown in Fig. 1.4. Since the
383 highly doped emitter (n^+-Si) has a resistivity in the order of mΩ cm, its contribution can be safely
384 neglected. The leakage current I_{leak} is given by

$$I_{\text{leak}} = \frac{V_{\text{stress}}}{R_{\text{module}}} = \frac{AV_{\text{stress}}}{\sum_{n=1}^{3} \rho_n l_n}, \tag{1.1}$$

385 where V_{stress} is the voltage stress applied to the module stack, $R_{\text{module}} = R_{\text{glass}} + R_{\text{poly}} + R_{\text{SiN}}$, A is
386 the area of the device and ρ_n, l_n are the electrical resistivity and thickness of the nth-layer ($1 \rightarrow$
387 glass, $2 \rightarrow$ encapsulant, $3 \rightarrow SiN_x$). Then, the voltage drop V_n at each material is given by

$$V_n = I_{\text{leak}} R_n = \frac{\rho_n l_n}{\sum_{m=1}^{3} \rho_m l_m} V_{\text{stress}} \tag{1.2}$$

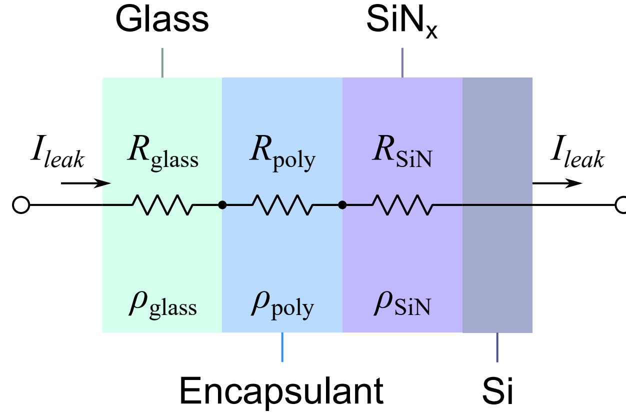

Figure 1.4: Schematic of a voltage divider model corresponding to the stack of materials at the front of Si solar module.

388

389 ## 1.5 Sodium Transport

390 While some phenomenological models to describe the kinetics of PID-s have been proposed
391 [14, 28, 29], in order to provide adequate solutions to prevent PID-s, a mechanistic understanding
392 of the processes behind the shunt formation is required. In that sense, very few attempts have been
393 made to propose a physical description of PID-s kinetics [15]. Transport of Na^+ in the module
394 stack is governed by Nernst-Planck equation

$$\frac{\partial C(\mathbf{x},t)}{\partial t} = -\nabla \cdot \mathbf{J} = -\nabla \cdot [-D\nabla C - \mu C \nabla \phi(\mathbf{x},t)], \tag{1.3}$$

395 where $C(x,t)$ is the concentration of Na^+ in units of ions per unit volume, as a function of the
396 position $\mathbf{x}$ and time t, $\mathbf{J}$ represents the total flux in units of ions per unit area per time, D is the
397 diffusion coefficient of Na^+ in the material in units of unit area per time, $\mu = qD/k_BT$ is the ionic
398 mobility in units of $\mathrm{cm}^2/\mathrm{V/s}$, q is the elementary charge, k_B is Boltzmann's constant, T is the
399 absolute temperature and $\phi(\mathbf{x},t)$ is the electric potential.

400 We shall see that, due to the discontinuity of the properties (e.g. diffusion coefficient, equi-
401 librium Na concentration), numerical integration generally is required, except for a very limited
402 subset of conditions where coarse approximations can simplify the problem [15].

403 1.6 Summary

404 Engineering solutions to alleviate PID-s requires a mechanistic model to describe the pro-
405 cesses behind shunt formation. While understanding of the mechanisms leading to loss of per-
406 formance has remarkably advanced over the past decade, the kinetics of degradation still needs
407 clarification. Phenomenological models can successfully predict some of the trends and timescales
408 for PID degradation but fail to correlate material properties that can be used to engineer PID-robust
409 silicon modules.

410 The motivation of this work is to propose a physical model that mechanistically explains
411 potential-induced degradation in the solar module. The overarching goal is to parametrize the
412 kinetics of PID-s and explain the factors that make a module PID-robust.

413 # 2 | Na transport kinetics in the module stack

414 The decoration of stacking faults in the n^+-Si emitter of the PV module follows the transport
415 of Na contamination through the different materials in the module stack. This process is driven by
416 the large voltage differential between the frame and the cell at the extremes of the array. Transport
417 is governed by Nernst-Planck equation (1.3)

$$\frac{\partial C(\mathbf{x},t)}{\partial t} = \nabla \cdot (D \nabla C) + \mu C \nabla \cdot \nabla \phi(\mathbf{x},t) + \mu \nabla C \cdot \nabla \phi(\mathbf{x},t), \tag{2.1}$$

418 Eqn. (2.1) needs to be solved for each material and coupled with adjacent materials by means of
419 adequate boundary conditions. This is illustrated in Fig. 2.1 where the module stack is schemati-
420 cally drawn alongside with the potential drop due to the applied voltage stress on the layer stack.

421 The first difficulty in this approach is the fact that the values of the diffusion coefficient of
422 Na in the module stack are either not available for the materials, or are extrapolated from measure-
423 ments performed at temperatures not relevant to PID [30–32]. It is required that characterization of
424 Na kinetics is performed under conditions as close as possible to operational, or with accelerated
425 testing.

426 As a first approximation, we assume that Na^+ in the front cover glass is accessible directly
427 at the glass/encapsulant interface in such a way that release is not rate limiting. This is in agreement
428 with the assumption that Na^+ transport is a temperature- and humidity- activated process in soda

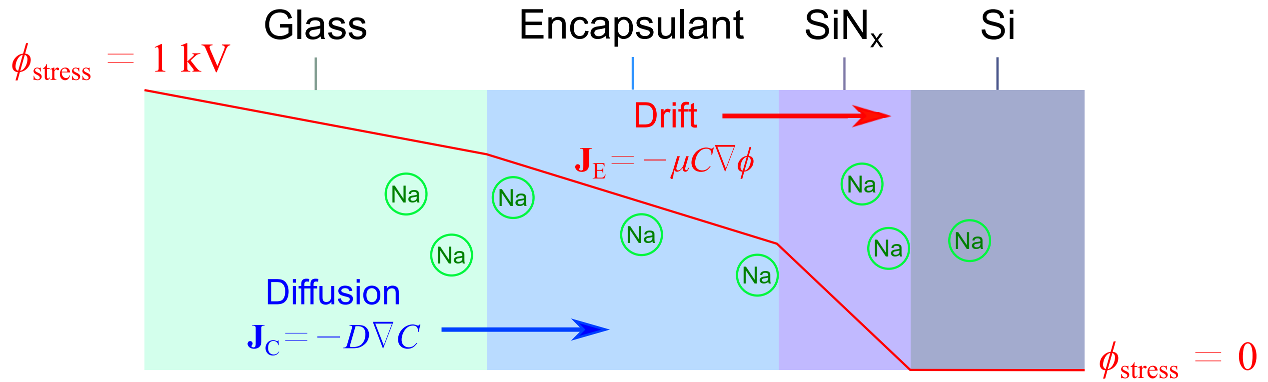

Figure 2.1: Schematic of transport of Na across the different materials in the module stack. According to the voltage divider model, application of a voltage stress over the module leads to a potential drop of different magnitude in each material. The resulting electric field induces a drift term that adds to the otherwise diffusive transport through the materials. The potential in the silicon emitter is neglected due to the large conductivity of this region, hence transport is assumed to occur just by diffusion in Si.

429 lime glass [21, 22]. In other words, we assume that the front cover glass plays the role of a source
430 of ions at the glass/encapsulant interface, which reduces the number of materials on which Eq.
431 (2.1) needs to be solved.

432 We also assume that the electric field $\mathbf{E} = -\nabla\phi$ is normal to the glass/encapsulant interface.
433 Furthermore, it is be assumed that diffusion can be approximated as a one-dimensional problem
434 which simplifies the computation without loss of generality.

435 2.1 Approximate voltages in the module stack

436 As discussed in Sec. 1.4, the potential drop in each material depends on the resistivity and
437 thickness of all of the other materials in the module stack. Table 2.1 shows typical literature values
438 of the resistivities and thicknesses of the different materials in the module stack. The estimated
439 electric field is based upon an applied stress voltage of $V_{stress} = 1000\,\mathrm{V}$. Notice that the real values
440 of the resistivities can be subject to orders of magnitude variations depending on the specific pro-

Table 2.1: Typical thicknesses and resistivities of the materials in a c-Si module

Layer	Material	Thickness[e](cm)	Resistivity (Ωcm)	Estimated E (kV/cm)[a]
1	Glass[b]	0.32	3×10^{12}	–
2	EVA[c]	4.5×10^{-2}	$10^{12} – 10^{15}$	$10^{-1} – 10^{4}$
3	SiN_x[d]	75×10^{-7}	$10^{4} – 10^{19}$	$10^{-2} – 10^{5}$

[a] Assuming a stress voltage of 1000 V.
[b] Ref. [34]
[c] Ref. [3, 34]
[d] Fit to the ohmic regime in Ref. [27] and Ref. [33].
[e] Ref. [34]

441 cessing conditions of the materials, as well as on the relative humidity and temperature [3, 22, 27].
442 In particular, electronic transport in SiN_x processed by plasma-enhanced chemical vapor deposi-
443 tion (PECVD) can range between 10^4 to 10^{19} Ωcm depending on the Si/N ratio introduced during
444 deposition [33].

445 2.2 Transport of Na in EVA

446 The widespread use of EVA as encapsulant in Si solar modules makes it important to de-
447 termine the impact of Na^+ transport in this polymer. Induced-coupled plasma (ICP) measurements
448 have successfully identified Na contamination in Si modules within the EVA encapsulant, close to
449 the SiN_x ARC, even prior to PID test [26]. To validate this assumption, Na drift-diffusion exper-
450 iments were performed in metal-EVA-metal structures to determine the penetration depth of Na
451 under conditions as close as possible to the ones referenced in Table 2.1.

2.2.1 Experiment

Metal-insulator-metal (MIM) structures were prepared by coating aluminum foil with EVA. Prior to the coating, aluminum foil is cleaned with acetone, isopropyl alcohol and deionized water. After curing, the exposed surface of EVA was intentionally contaminated with Na by thermally evaporating NaCl at $\sim$800 °C. After contamination, silver paste was deposited onto the contaminated surface to complete the MIM structure. The thickness of EVA was determined from multiple point measurement using scanning electron microscopy (SEM). The average value of the thickness of EVA is 440 µm.

The MIM structures were put on a hot plate at 80 °C and subject to a voltage stress of 100 V, equivalent to 2.3 kV/cm (roughly one third of the value estimated in Table 2.1). Three repetitions were performed for the same conditions. Relative humidity was not monitored.

The samples were sent to the National Renewable Energy Laboratory to perform time-of-flight secondary-ion mass spectroscopy characterization (ToF-SIMS). After contact removal, the samples were rinsed in deionized water to remove excess Na. For ToF-SIMS analysis the samples were sputtered from the side onto which Na contamination was introduced.

2.2.2 Results

Fig. 2.2 shows a representative SIMS profile of a sample stressed at 80 °C and 2.3 kV/cm for 12 h. Due to the large concentration of ions at the interface, a large memory effect is observed in the concentration profile, due to re-dposition of Na during sputtering. During this timescale, Na reached a depth of $\sim$15 µm, beyond which, the concentration drops below detectable limits. By fitting the concentration profile to Eq. (3.7), we estimated a diffusion coefficient of 4×10^{-14} cm^2/s.

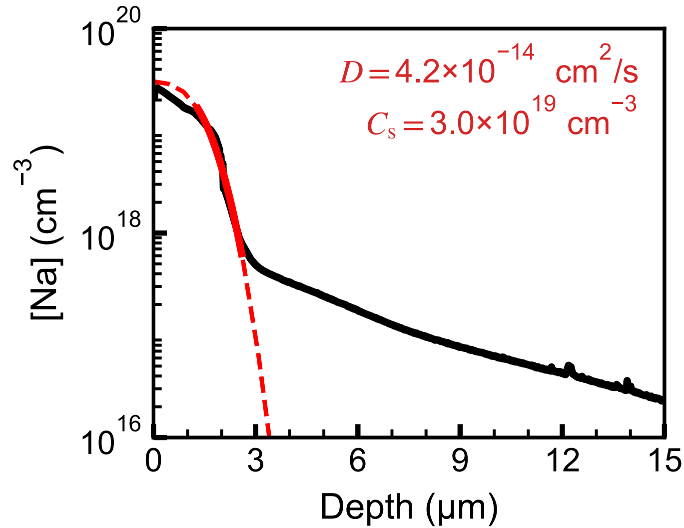

Figure 2.2: Representative Na drift-diffusion profile obtained by SIMS of a metal-EVA-metal structure intentionally contaminated with Na on one of the ends stressed for 12 h under an electric field of 2.3 kV/cm at a temperature of 80 °C.

473 Using Eq. (3.9), we determined that the characteristic Na transit time, for a 300 μm thick EVA
474 encapsulant stressed at $7\,\mathrm{kV\,cm^{-1}}$ is $\approx$ 36 h. This finding contrasts with the trends on the nor-
475 malized power output observed on PID-susceptible devices from reports of p-Si devices stressed
476 under similar conditions [5, 35–38], and those from normalized R_{sh} [24, 39–41] for which a 5 %
477 degradation of the initial condition occurs within an average time of $\approx$13 h. While Eq. (3.7) does
478 not consider the contribution of the ionic concentration to the electric potential, the net effect of
479 this is to screen the applied electric stress. This means that, when considering the image charge
480 effect of the ion distribution, drift decreases considerably close to the source. This result indicates
481 that transport in EVA has a limited impact in the kinetics of PID. Given this result, we think that
482 transport of Na to the cell interface occurs during lamination, or that Na is already present on cell

2.3 Summary

The typical electrical stress in each material of the PV module was estimated using a voltage divider model, for which a potential drop ranging from $10^{-2}\,\mathrm{V\,cm^{-1}}$ to $10^{4}\,\mathrm{V\,cm}$ in the SiN_x film was estimated. Drift-diffusion experiments in EVA showed that Na^+ is not expected to traverse the full depth of the encapsulant at significant concentrations to cause PID-s in the timescales within which degradation is typically reported on PID-prone devices. This finding is in agreement with reports suggesting the presence of Na^+ on the surface of SiN_x prior to PID tests. It is possible that damp-heat tests at a high relative humidity (85 % RH) lead to electrochemical reactions that are not accounted for in the scope of this work. Nevertheless, changes in the conductivity of EVA associated to different levels of water content and temperature might have an impact on the magnitude of the electric field in SiN_x.

3 | Transport of Na in SiN_x

Sodium moves through SiN_x as an ionic species subject to the kinetics described by Eq. (3.7). In this chapter we show that transport in SiN_x is very sensitive to the magnitude of the applied electric potential, as well as the average concentration of Na^+. We also establish a number of conditions within which, we can simplify Eq. (3.7), in order to derive analytical approximations that allow us to characterize the drift-diffusion kinetics of Na contamination in dielectrics. While some reports suggest that SiN_x films of the sort used in solar modules can act as barriers against mobile charge contamination [42–44], there is also evidence that, under an electric field of 0.5 MV/cm, sodium can drift across an 80 nm thick layer of SiN_x in just 25 min at 80 °C [32]. Given the large variations in the resistivities of the different materials in p-Si modules, electric fields of the order of 0.5 MV/cm can't be discarded. Therefore, accurate knowledge of Na kinetics in silicon nitride under typical module operating conditions is necessary.

3.1 Characterization of drift-diffusion kinetics using C-V measurements

Mobility of ionic charge in dielectrics has been addressed in the past by means of transient current measurements [45–48]. This method assumes that mobile charges drift over the entire length of the dielectric during the measurement. This assumption is adequate for ions with mobilities fast enough to enable drift across the dielectric within the time scale of the experiment or less [48]. Nevertheless, ions with lower diffusivities might not satisfy this criterion, especially at low temperatures. In contrast, methods relying on the determination of the flatband voltage (V_{FB}) from capacitance-voltage (C-V) methods, enable the detection of ion migration in dielectrics on a broader temperature range. Among these methods, the bias-temperature-stress (BTS) method has been widely used to determine ionic migration [43–45, 49–52].

3.2 Trap-corrected bias-temperature-stress method

In the standard BTS method, ionic contribution to flatband voltage measurements can be obfuscated by carrier trapping effects and hence, modifications are required to adequately quantify ion kinetics. A signature due to trapping effects has in fact been identified in dielectrics that are known to have a large density of trap centers, including SiN_x [49, 53, 54] and high-*k* dielectrics such as hafnium oxide [55]. Conflation of flatband shift due to carrier trapping in ionic mobility measurements results in incorrect attribution of drift characteristics as seen in porous SiO_x [51], which precludes reliable analysis of migration in the dielectric. We developed a time-resolved

525 capacitance-voltage method which incorporates a kinetics model to estimate the ionic diffusivity
526 in dielectrics. We used this method to quantify the diffusion coefficient of Na^+ in SiN_x which is
527 necessary to study the ingress of Na in the emitter of p-Si modules leading to PID.

528 3.2.1 Flatband fitting

529 In the BTS method, the barrier for ionic diffusion is lowered by providing a thermal stress
530 (i.e. heating the device above room temperature) and an electrical stress, by applying an electro-
531 static potential V_{stress} to the dielectric.The flatband voltage at time t with respect to its value at $t = 0$
532 is determined by integration of Poisson's equation in the dielectric

$$\frac{d^2\phi}{dx^2} = -q\frac{n(x,t)}{\epsilon_{\text{ins}}}, \quad n(x,t) \equiv z_{\text{ion}}C(x,t) + z_{\text{traps}}n_{\text{traps}}(x,t), \tag{3.1}$$

where z_{ion}, z_{traps} are the valency of ionic species and traps respectively ($z_{\text{ion}} = 1$, for Na^+ and $z_{\text{traps}} = \pm 1$, depending on the type of carrier captured), $C(x,t)$, $n_{\text{traps}}(x,t)$ are the concentration of mobile ions and occupied traps respectively, and ϵ_{ins} is the permittivity of the dielectric. Eq. (3.1) is integrated from a position in the insulator to the position $x = L$, located at the surface of the semiconductor. The boundary conditions assumed are that the band bending and the potential vanish at the silicon surface in the flatband condition ($d\phi/dx \to 0$ and $\phi \to 0$ as $x \to L$) and, that $\phi(x = 0) = V_{\text{FB}} - W_{\text{ms}}$; where W_{ms} represents the difference between the work function of the metal and that of the semiconductor. This leads to the general expression for V_{FB} [56]:

$$V_{\text{FB}}(t) = W_{\text{ms}} - \frac{q}{\epsilon_{\text{ins}}}\int_0^L x' n(x',t)dx'. \tag{3.2}$$

533 Assuming that the concentration of Na^+ and occupied traps is negligible at $t = 0$, we can define the
534 shift in flatband voltage as

$$\Delta V_{\mathrm{FB}}(t) \equiv V_{\mathrm{FB}}(t) - V_{\mathrm{FB}}(t=0) = \underbrace{-\frac{q}{\epsilon_{\mathrm{ins}}}\int_0^L x' C(x',t)dx'}_{\Delta V_{\mathrm{FB}}^{\mathrm{ion}}(t)} \overbrace{-\frac{q z_{\mathrm{traps}}}{\epsilon_{\mathrm{ins}}}\int_0^L x' n_{\mathrm{traps}}(x',t)dx'}^{\Delta V_{\mathrm{FB}}^{\mathrm{traps}}(t)}, \quad (3.3)$$

535 which is independent of W_{ms} and captures the effect of occupied traps in the dielectric.

536 Eq. (3.3) also implies that, if ions and traps do not interact, their contribution can be
537 decoupled which is the basis of the trapping correction.

538 The ionic contribution to the flatband voltage shift $\Delta V_{\mathrm{FB}}^{\mathrm{ion}}(t)$ can be now estimated by sub-
539 tracting the component due to electronic trapping $\Delta V_{\mathrm{FB}}^{\mathrm{traps}}(t)$, measured on devices without inten-
540 tional ion contamination $C(x,t) = 0$, from the flatband voltage shift measured on ion-contaminated
541 devices:

$$\Delta V_{\mathrm{FB}}^{\mathrm{ion}}(t) = \Delta V_{\mathrm{FB}}(t) - \Delta V_{\mathrm{FB}}^{\mathrm{traps}}(t). \quad (3.4)$$

542 3.3 Kinetics of ion diffusion and drift in SiN_x

543 The kinetics of ion transport is then obtained by relating $\Delta V_{\mathrm{FB}}^{\mathrm{ion}}(t)$ to the ionic concentration
544 as prescribed by Eq. (2.1). From Eq. (3.1), we see that the electric potential is a function of the
545 ionic and trap concentrations in the dielectric itself, which implies that Nernst-Planck and Poisson's
546 equations are coupled. Nevertheless, at times less than a critical value τ_c, beyond which accumu-
547 lation of ions at the interface leads to surface charges induce $E = Q/\epsilon$ comparable with V_{stress}/L,
548 the concentration can assume a limiting constant value $C(x) = C$. In such a case, the solution to

549 the ionic component of (3.1) is simply $\phi = -(q/\epsilon_{\text{ins}})L^2C$. This means that for concentrations

$$C \ll C_{\text{th}} \equiv \frac{2\epsilon_{\text{ins}}}{qL^2}V_{\text{stress}} \tag{3.5}$$

550 the magnitude of the ionic charge distribution is much less than the applied electric potential, and
551 the electric field can be assumed to be V_{stress}/L. The Na-contaminated SiN_x films prepared for this
552 work were analyzed using X-ray photoelectron spectroscopy (XPS) which has a detection limit of
553 $5\times10^{18}\,\text{cm}^{-3}$ and no signal corresponding to Na was detected. In comparison, the magnitude of
554 the applied voltage is 8.6 V over a 86 nm thick layer of SiN_x ($\epsilon_r \approx 7$), which sets the right hand side
555 of (3.5) on the order of $10^{18}\,\text{cm}^{-3}$, indicating that, indeed C is low compared to V_{stress} and hence,
556 $E = -\nabla\phi \to V_{\text{stress}}/L$. This allows us to assume a constant drift velocity $v_\text{d} = -\mu\partial_x\phi = zqDE/k_\text{B}T$
557 and remove Laplacian term in (2.1):

$$\frac{\partial C(x,t)}{\partial t} = \frac{\partial}{\partial x}\left(D\frac{\partial C}{\partial x}\right) - v_\text{d}\frac{\partial C}{\partial x}, \tag{3.6}$$

558 where we have reduced the problem to one-dimension. The advection term in (3.6) can be elimi-
559 nated by introducing the moving reference frame [57, 58]

$$x' = x - v_\text{d}, \quad t' = t,$$

560 which transforms Eq. (3.6) to a pure diffusion equation in the primed reference frame. We assume
561 a constant source of ions at the surface of SiN_x: $C(x=0,t) = C_\text{s}$ and a closed boundary at the
562 Si interface: $[-D\partial_x C + v_d C]_{x=L} = 0$. Given these assumptions, we can now define the analytical
563 solution of Eq. (3.6) for this set of boundary conditions, before the onset of accumulation ($t < \tau_c$,
564 discussed in Sec. 3.6) as follows

$$C(x,t) = \frac{C_\text{s}}{2B}\left[\text{erfc}\left(\frac{x-\mu Et}{2\sqrt{Dt}}\right) + \text{erfc}\left(-\frac{x-2L+\mu Et}{2\sqrt{Dt}}\right)\right], \tag{3.7}$$

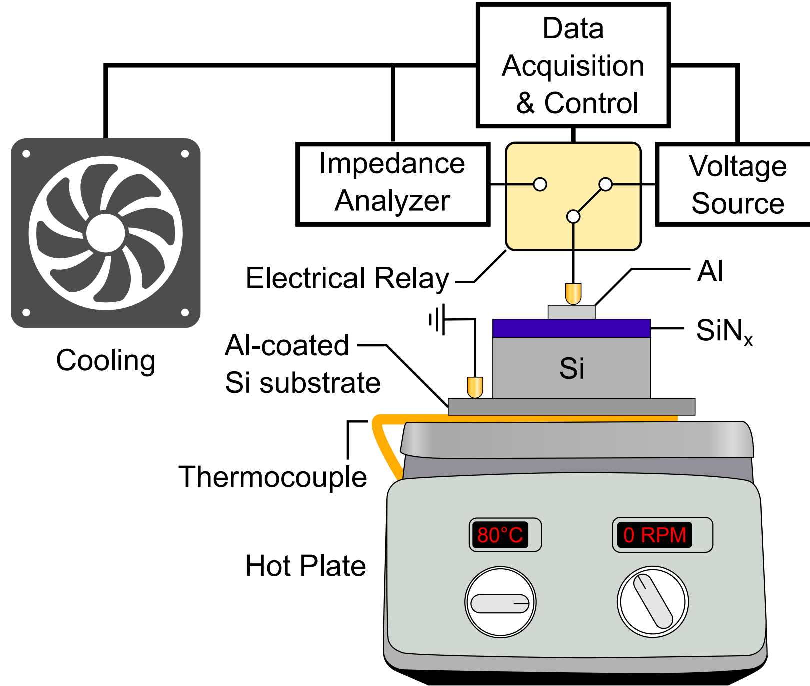

Figure 3.1: Schematic of the BTS setup used to quantify Na^+ migration in SiN_x.

565 with a normalization constant $B \equiv \operatorname{erfc}\left(-\mu E t / 2\sqrt{Dt}\right)$.

566 The diffusivity of ionic species D and concentration of ions at the source C_s can be deter-
567 mined from the experimental ΔV_{FB} by fitting the theoretical flatband shift obtained from (3.3) and
568 (3.7) to the experimental flatband shift obtained through (3.4).

569 The fitting is performed using trust-region reflective nonlinear least squares. The uncer-
570 tainty of the fitted parameters is taken from the 95 % confidence intervals estimated from the co-
571 variance matrix of the fit and using the t-student distribution.

572 3.4 Experiment

573 Metal-insulator-semiconductor (MIS) structures were fabricated on n-type silicon (100)
574 wafers with a resistivity of 2.7 Ω cm. The wafers were cleaned with acetone, ethanol and isoporpyl

575 alcohol and then cleaned with RCAI and RCAII procedures, followed by a 1 % hydrofluoric acid
576 dip. SiN_x films were grown on the polished side of the wafer using PECVD with a NH_3/SiH_4 ratio
577 of 7. This ratio was chosen to obtain high SiN_x resistivity [59] to ensure a significant potential drop
578 across the dielectric, which leads to drift times within reasonable timescales in the experiments.
579 Additionally, SiO_2 films were grown by dry oxidation at a temperature of 1100 °C. The thickness
580 and refractive index of the as-grown films were mapped using spectroscopic ellipsometry. An
581 average thickness of 86 nm and an average index of refraction of 1.89 at 600 nm were estimated
582 for the SiN_x. The dielectric layers were subsequently cleaned with isopropyl alcohol and ethanol to
583 remove surface contaminants and the back surface was swabbed with hydrofluoric acid. Aluminum
584 gate electrodes of approximately 200 nm were deposited by thermal evaporation onto SiN_x. The
585 electrodes were defined by a shadow mask with 1 mm diameter circles and a pitch of 2.54 mm.
586 A layer of aluminum was deposited on the bottom side of the wafer to produce the back contact.
587 In devices with intentional contamination, 25 nm of NaCl were thermally evaporated at 800 °C,
588 followed by the deposition of the gate without breaking vacuum.

589 An in-situ C-V setup with automated BTS capabilities was developed to perform migration
590 studies. As illustrated in Fig. 3.1, the temperature stress is provided by a temperature-controlled
591 hotplate with feedback from a thermocouple directly placed underneath the sample. A software-
592 controlled relay was used to switch between stressing and measuring modes in order to periodically
593 monitor ΔV_{FB} as a function of stress BTS time. Contact to the back of the sample was achieved by
594 placing the sample on an Al-coated silicon wafer, which provides adequate thermal distribution.
595 Contact to the Al-coated wafer and the gate was achieved by means of Au-plated spring-loaded
596 contacts. The system applied BTS stress to the MIS capacitors in 1 or 4 h intervals using a pro-
597 grammable hotplate and a Keithley 2401 source meter to apply a direct current (DC) bias. It has

been reported that an electric field on the order of $1\,\mathrm{MV\,cm^{-1}}$ is required to observed PID in silicon PV modules, which contrasts with the voltage-divider estimation in Table 2.1. The reason for this discrepancy is unknown [60], but it could be attributed to large variations in the electrical properties introduced during the PECVD deposition of SiN_x. An electric field of $1\,\mathrm{MV\,cm^{-1}}$, is adequate for our experiments since it satisfies Eq. (3.5) and was thus applied to the MIS structures during migration experiments, in agreement with other studies [32]. After each BTS interval, a fan (Fig. 3.1) was used to cool down the devices to room temperature within 15 min. Once cooled, C-V curves were acquired with a HP4194A impedance analyzer at 1 MHz, to ensure that ions were unaffected by the 100 mV (peak to peak) alternating current (AC) signal from the impedance analyzer. During the C-V acquisition, the DC voltage was swept from −8.6 to 8.6 V and each measurement was averaged 32 times with a dwell time of 5 ms per point. The flatband voltage as a function of BTS time was estimated from the C-V curves using a second-derivative method described in Ref. [61].

3.5 Results

The need to correct for traps in the dielectric to obtain the ionic component to ΔV_{FB} is showin in Fig. 3.2. In devices without intentional Na contamination, ΔV_{FB} increases as a function of time, which is explained by an increase in negative charge in the dielectric according to (3.3). This effect originates from electron trapping as demonstrated in a previous study [54], and can be further quantified by integrating Frenkel-Poole emission current [63]. A first-order kinetics model [64] was used to determine a trapping time constant of 2.5 h. Because each C-V sweep is completed in 2 min, it is not expected that the DC bias from the C-V measurement influences

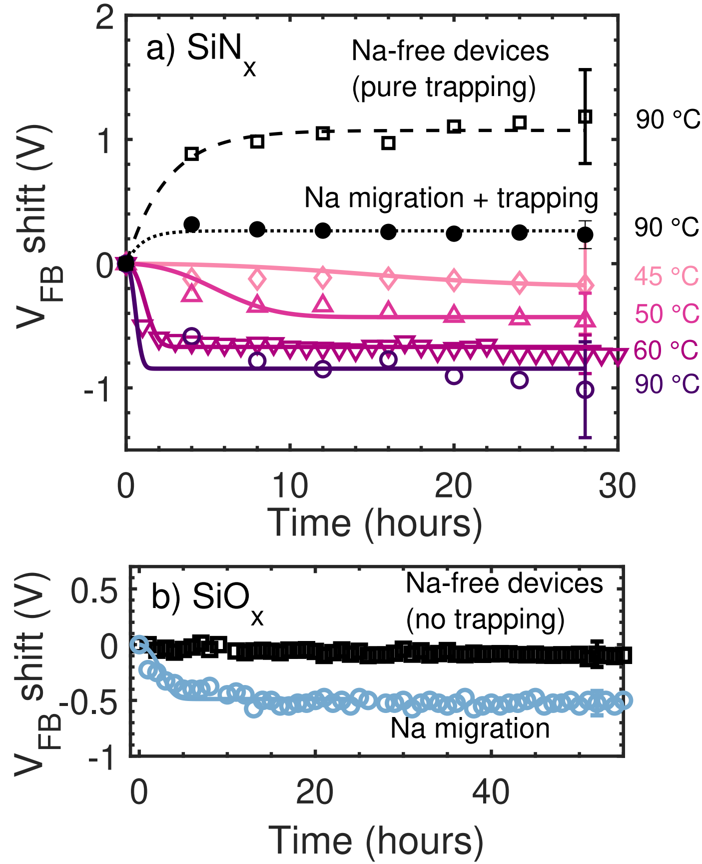

Figure 3.2: Flatband shift as a function of time and temperature: (a) in SiN_x capacitors stressed at $1\,MV\,cm^{-1}$. An example of raw flatband shift including both Na^+ and trapping is shown in black empty squares with a dotted line as a guide to the eye. Trapping-corrected flatband voltage shifts are shown at different temperatures. The fits obtained from the Nernst-Planck migration model are depicted by solid lines. (b) SiO_2 capacitors without trapping correction (pure ionic shift) in both Na-free and Na-contaminated devices at $0.5\,MV\,cm^{-1}$ and 50 °C. Reproduced from Ref. [62]

619 the flatband shift. The raw ΔV_{FB} signal (before trapping correction) in a Na-contaminated sample
620 is shown in solid black circles in Fig. 3.2, which includes the contributions from both, electron
621 trapping (negative charging) and Na migration (positive charging). To account for charge due
622 electron trapping in SiN_x [49, 53, 54], we estimated ΔV_{FB}^{traps} by averaging the flatband shift from
623 four Na-free devices and subtracted its contribution from ΔV_{FB}, as prescribed by Eq. (3.4). After
624 applying this correction, a negative flatband shift is observed as a function of time, as expected from
625 the ingress of positive ions into the dielectric. Note that the error bars originate from variations in

626 the concentration of trapped charge in Na-free devices used in the estimation of $\Delta V_{\mathrm{FB}}^{\mathrm{traps}}$. Overall,
627 our trapping-corrected data captures the resulting ΔV_{FB} in Na-contaminated devices across device-
628 relevant temperatures.

629 To confirm the applicability of the trapping-corrected BTS method to isolate ion migration,
630 experiments were conducted on thermal SiO_2 capacitors, which are known to exhibit very little
631 to no carrier trapping in the bulk of the dielectric compared to SiN_x [49, 63, 65]. Fig. 3.2 shows
632 the measured ΔV_{FB} without trapping correction in Na-free and Na-contaminated SiO_2 capacitors.
633 As expected, we observed little-to-no variation in the flatband voltage in control samples without
634 intentional Na contamination. In Na-contaminated SiO_2 capacitors, a flatband shift of $\approx 0.5\,\mathrm{V}$ was
635 detected without the need for trapping correction. This trend is well fit by our ion migration model.
636 This result confirms that the experimental conditions and detection method are suitable to detect
637 ion migration within the timescales of the experiment.

638 Using the described trapping-corrected BTS method, we determined the Arrhenius relation-
639 ship for the migration of Na^+ in SiN_x by averaging the diffusivities of measurements collected over
640 4–8 devices at each temperature. Fig. 3.3 shows the extracted diffusivities of Na^+ in SiN_x at differ-
641 ent temperatures together with the 95 % confidence interval. The results of the fit to the Arrhenius
642 relationship give a diffusion coefficient prefactor of $D_0 = 1.4 \times 10^{-14}\,\mathrm{cm^2/s}$ with a 95 % confi-
643 dence interval of $[1.2 \times 10^{-15}, 1.6 \times 10^{-13}]\,\mathrm{cm^2/s}$ and an activation energy of $E_a = 0.14\,\mathrm{eV}$, with
644 a 95 % confidence interval of [0.07, 0.21] eV. Note that the deviation from the higher-temperature
645 results of Wilson et al. [32] indicates a large difference in the activation energy compared to the
646 range of temperatures in this work.

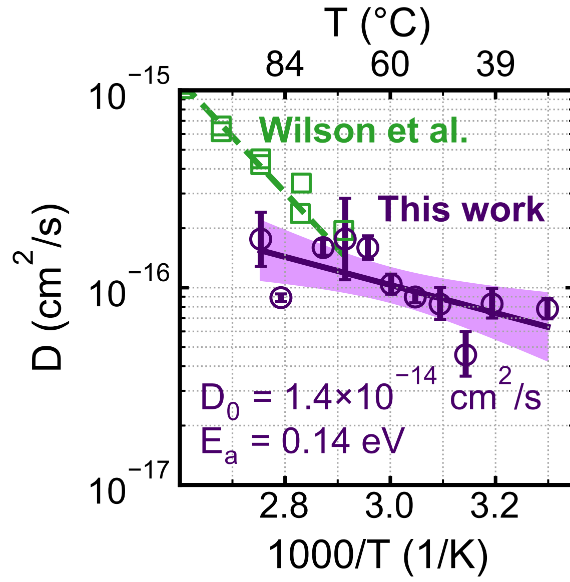

Figure 3.3: Arrhenius relationship for the diffusivity of Na^+ in SiN_x evaluated by the trapping-corrected BTS method and by Wilson et al. [32], using a Kelvin-probe-based method. The estimated prefactor for the diffusion coefficient is $D_0 = 1.4 \times 10^{-14}\,\mathrm{cm}^2/\mathrm{s}$ with a 95 % confidence interval of $[1.2 \times 10^{-15},\ 1.6 \times 10^{-13}]\ \mathrm{cm}^2/\mathrm{s}$. The estimated activation energy is $E_a = 0.14\,\mathrm{eV}$, with a 95 % confidence interval of [0.07, 0.21] eV.

647
3.6 Characteristic Na^+ transit time

648 To provide context to the results of the ion-migration experiments with respect to PID-s, we
649 estimate how the Na^+ concentration at the SiN_x/Si interface changes over time. Since Na transport
650 can eventually lead to PID-s, we consider the characteristic time τ_c at which Na^+ drifts across the
651 dielectric, as the solution to the equation

$$L = 2\sqrt{D\tau_c} + \mu E \tau_c \tag{3.8}$$

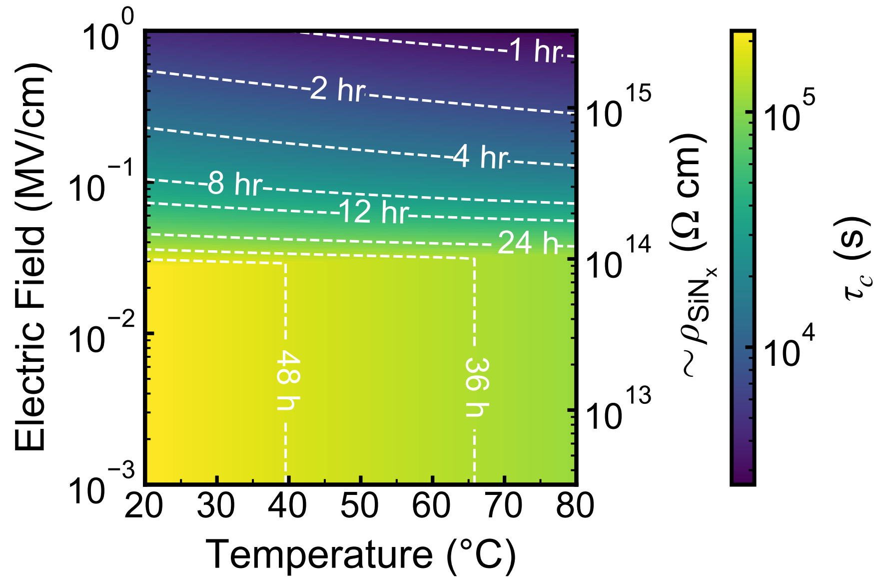

Figure 3.4: Characteristic Na transit time in a 65 nm-thick SiN_x film as a function of the module temperature and electric field across the dielectric.

If the magnitude of the electric field in SiN_x is low with respect to the diffusive term, $-D\nabla^2 C \ll \mu EC$, then $\tau_c \to L^2/D$. If the drift term dominates $\tau_c \to L/\mu E$. This can be expressed as

$$\tau_c = \inf\left\{t = \frac{L^2}{D}, \quad t = \frac{L}{D}\left(\frac{v_{\mathrm{th}}}{E}\right) + \frac{2}{D}\left(\frac{v_{\mathrm{th}}}{E}\right)^2\left\{1 \pm \left[1 + \left(\frac{E}{v_{\mathrm{th}}}\right)L\right]^{1/2}\right\} \middle| t \in \mathbb{R}^+\right\}, \tag{3.9}$$

652 where $v_{\mathrm{th}} = k_{\mathrm{B}}T/q$ is the thermal voltage. The complete derivation of Eq. (3.9) is shown in
653 Appendix A.

654 Fig. 3.4 shows the characteristic transit time across a typical nitride thickness of 65 nm as
655 a function of the module temperature and electric field across the SiN_x in ranges relevant to solar
656 module operation. The range of values selected for the electric field in SiN_x account for a large
657 variability on the resistivities of the materials in the module [3, 12, 22, 33, 34, 66]. To estimate
658 the values on the resistivity axis in Fig. 3.4 we consider a borosilicate glass with a resistivity
659 $\rho_{\mathrm{glass}} \approx 3 \times 10^{12}\,\Omega\,\mathrm{cm}$ [67], ethylene-vinyl acetate EVA with a resistivity $\rho_{\mathrm{EVA}} \approx 5 \times 10^{13}\,\Omega\,\mathrm{cm}$
660 and a voltage differential of 1000 V, to estimate the silicon nitride resistivity corresponding to

661 the electric field in the left axis. Under such conditions, Na migration through the dielectric can
662 occur between a few hours to a few days depending primarily on the potential drop across SiN_x.
663 Such times are lower than the observed degradation times after accelerated experiments at high
664 temperature and in the field [38, 68]. However, τ_c only reflects the transport across SiN_x and does
665 not represent the actual time to PID in the full module stack.

666 It is worth considering scenarios in which the assumptions made to derive Eq. (3.7) do
667 not longer hold, namely (1) large ion concentrations $C_s \approx 2\epsilon_{ins}V_{stress}/qL^2$ where the distribution of
668 mobile ions does affect the local potential within the dielectric, (2) long stress times: $t > \tau_c$ where
669 the flatband potential becomes sensitive to the accumulation of ions at the dielectric/semiconductor
670 interface, and (3) finite sources of ions.

671 3.7 Conclusions

672 We derived a method to quantify Na^+ diffusion kinetics in SiN_x using a drift-diffusion
673 model to analyze the corresponding flatband voltage shift in MIS structures. We developed a C-V
674 setup for measuring MIS capacitors under BTS. We developed a model to correct nonidealities
675 from charge trapping in the dielectric. This description of a C-V based approach to parametrize
676 ion migration should allow reliable quantification of ion diffusion kinetics broadly in dielectrics.
677 We presented an analytical approximation to bound the transport times of Na^+ in SiN_x within the
678 context of PID. We showed that migration through PV-relevant, 65 nm-thick silicon nitride films
679 can occur within a few days in field-operating conditions. We can easily extend this study to a
680 variety of SiN_x of different compositions and electrical properties. Furthermore, quantification of
681 the transport kinetics from this study is especially significant to determine the overall kinetics of

682 PID-s in the full module stack.

683 Part of Chapter 3 has been published in *Phys. Status Solidi A*. under the title "Quantifi-
684 cation of sodium ion migration in SiN_x by flatband-potential monitoring atdevice operating tem-
685 peratures", by G. von Gastrow, **E. Martinez-Loran**, J. Scharf, J. Clenney, R. Meier, P. Bandaru,
686 M. Bertoni, and D. Fenning. The dissertation/thesis author was an author of equal contribution,
687 together with G. von Gastrow and J. Scharf.

4 | Finite Element Model of Mobile-Ion Kinetics

Sodium contamination is known to be deleterious to semiconductor devices since the early days of the semiconductor industry. The need to mitigate this problem opened the way for studying mobile charge transport in dielectrics commonly used in the industry [42–45, 69–73]. In silicon photovoltaic (PV) modules, Na contamination has been determined as the root cause for PID-s, and linked to failure within a timescale of a few hours to a few days under accelerated testing [5, 24, 35, 36, 38, 39, 41, 74]. In section 3.3 we described a simplified model to estimate the kinetics of Na^{+} migration under the limiting case of short migration times ($t < \tau_c$) and low ionic concentrations with respect to the applied electric field ($C \ll 2\epsilon_{\mathrm{ins}}/qL^2$). In this chapter, as general solution to Eq. (2.1) is presented, using only a limited set of assumptions. We then expand the model to accommodate for a flux of ions out of the dielectric and into the semiconductor. This is useful in modeling PID-s kinetics on p-Si modules.

701 ## 4.1 Modeling mobile charge kinetics in MIS structures

702 The conditions assumed to derive an analytical approximation to Eq. (3.6) are generally not
703 held for long-time experiments nor for a wider range of mobile charge concentrations, as would
704 be expected for PID-s in the case of Si PV modules [23, 75, 76]. In metal-insulator-semiconductor
705 (MIS) structures, the concentration of ions near the metal gate induces an image charge in the
706 metal, with the opposite sign of the ion. The resulting electric field points in the negative direction
707 of x, leading to a diffusion dominated region in the vicinity of the metal gate [69]. It is also typi-
708 cal to assume a closed boundary at the dielectric/semiconductor interface [56, 69], which leads to
709 ion accumulation at that interface due to ion drift towards the semiconductor. Just as in the metal
710 gate, accumulation of ions at the dielectric/semiconductor interface induces an image charge of
711 the opposite sign in the semiconductor –which we measure as $\Delta V_{\mathrm{FB}}^{\mathrm{ion}}$ in Eq. (3.4), but in this case
712 the resulting image charge acts on the same direction of the applied electric field. This effect was
713 first reported by Snow et al. [69], where the authors introduced a boundary layer approximation to
714 estimate the image charge in the semiconductor. This approach has the advantage of avoiding the
715 need to solve the coupled Poisson-Nernst-Planck (PNP) system of equations. Nevertheless, this
716 model does not mechanistically account for the image charge effect at the source and semiconduc-
717 tor interfaces or the depletion of ions near the gate. In such cases the Poisson's equation for the ion
718 distribution:

$$\nabla \cdot \nabla \phi_{\mathrm{ion}} = -\frac{zqC(x,t)}{\epsilon_{\mathrm{ins}}} \tag{4.1}$$

719 needs to be solved self-consistently with (2.1). Analytical solutions to Poisson-Nernst-Planck
720 equations are available just for a few limiting cases, namely, low applied voltages and binary

721 electrolytes close to charge neutrality [77–80]. In this chapter, we present a finite-element-method
722 (FEM) solution to the Poisson-Nernst-Planck coupled system of equations. This methodology has
723 the advantage of fully describing the kinetics of ion migration in MIS structures and providing a
724 framework to model transport across stacks of materials. This is specially useful, for instance to
725 describe ion ingress leading to shunt formation in PID-s.

726 The boundary conditions for Eq. (4.1) can be set by estimating the image charges induced
727 by the ion distribution. The contribution of image charge of ionic origin $Q_{\text{ion}} = q\int_0^L C(x',t)dx'$ to
728 the drift term in Eq. (2.1) arises from Na^+ charge being imaged at both, the metal gate Q_G and
729 the semiconductor Q_S interfaces of the MIS structure. The surface charge distribution of image
730 charges due to ionic migration are determined by [56, 69]:

$$Q_G = q\int_0^L \left(\frac{x'-L}{L}\right) C(x',t)dx' \leq 0 \tag{4.2a}$$

$$Q_S = -q\int_0^L \left(\frac{x'}{L}\right) C(x',t)dx' \leq 0, \tag{4.2b}$$

731 with L the thickness of the dielectric. It follows that $-Q_{\text{ion}} = Q_G + Q_S$. The electric fields
732 associated with these charge distributions have opposite directions inside the dielectric:

$$-\nabla\phi_{\text{ion}}\big|_{x=0} = \mathbf{E}_{\text{ion,G}} = \hat{\mathbf{x}}\frac{q}{\epsilon_{\text{ins}}}\int_0^L \left(\frac{x'-L}{L}\right) C(x',t)dx' \tag{4.3a}$$

$$-\nabla\phi_{\text{ion}}\big|_{x=L} = \mathbf{E}_{\text{ion,S}} = -\hat{\mathbf{x}}\frac{q}{\epsilon_{\text{ins}}}\int_0^L \left(\frac{x'}{L}\right) C(x',t)dx' \tag{4.3b}$$

733

734 Thus, for $\mathbf{E} = E\hat{\mathbf{x}}$, the image charge field at the gate opposes the external electric field,
735 while the image charge field at the semiconductor interface adds to it. Eq. (4.3) can be introduced

736 as the boundary conditions to Poisson's equation

$$\nabla\phi(x=0)\cdot\hat{\mathbf{n}}_{\mathrm{G}} = E_{\mathrm{stress}} + \frac{q}{\epsilon_{\mathrm{ins}}}\int_0^L \left(\frac{x'-L}{L}\right) C(x',t)\,dx' \tag{4.4a}$$

$$\nabla\phi(x=L)\cdot\hat{\mathbf{n}}_{\mathrm{S}} = -E_{\mathrm{stress}} - \frac{q}{\epsilon_{\mathrm{ins}}}\int_0^L \left(\frac{x'}{L}\right) C(x',t)\,dx', \tag{4.4b}$$

737 where $\hat{\mathbf{n}}_G = -\hat{\mathbf{x}}$ and $\hat{\mathbf{n}}_S = \hat{\mathbf{x}}$ are the normal vectors to the gate and semiconductor surfaces enclosing
738 the insulator volume in the MIS structure.

739 4.2 Finite Element Method Implementation of the PNP cou-
740 pled system

741 The general solution to the Poisson-Nernst-Planck system requires integration over the
742 space and time. Spatial integration is relatively straightforward using the finite element method.
743 The general approach to impose the boundary conditions require writing the spatial part of the
744 partial differential equation (PDE) as an integral equation (i.e. the "weak form"), which has the
745 advantage of reducing the computational load of evaluating second order spatial derivatives [81,
746 82]. This formulation also allows us to easily introduce both, the Dirichlet and Neumann bound-
747 ary conditions [81]. Time integration must be addressed by a finite difference scheme using the
748 solutions computed by the FEM solver.

749 Among the different time integration schemes, the two-step trapezoidal-second order back-
750 ward difference (TR-BDF2) method has proven to be very reliable for semiconductor modeling
751 [83, 84] because of its strong stability [83–86] compared to other time stepping approaches like
752 the Crank-Nicholson method, which is known to introduce spurious oscillations if un-damped [87].

753 The TR-BDF2 advances the system

$$\frac{\partial C}{\partial t} = F[C(t), \phi(t), t] \tag{4.5}$$

754 from t_n to $t_{n+1} = t_n + \Delta t_n$ in two steps [83, 84]. In Eq. (4.5), F corresponds in this case to the right
755 hand side of (2.1). The first step consists of a trapezoidal time integration by which the system is
756 advanced from t_n to $t_{n+\gamma} = t_n + \gamma \Delta t_n$ $(0 < \gamma < 1)$:

$$C^{n+\gamma} - \gamma \frac{\Delta t_n}{2} F^{n+\gamma} = C^n + \gamma \frac{\Delta t_n}{2} F^n. \tag{4.6}$$

757 The system is then advanced from $t_{n+\gamma}$ to t_{n+1} using the second order differentiation (BDF2):

$$C^{n+1} - \frac{1-\gamma}{2-\gamma} \Delta t_n F^{n+1} = \frac{1}{\gamma(2-\gamma)} C^{n+\gamma} - \frac{(1-\gamma)^2}{\gamma(2-\gamma)} C^n. \tag{4.7}$$

758 In equations (4.6) and (4.7) we have used the notation $C^{n+\gamma} = C(x, t_n + \gamma \Delta t_n)$ and $C^{n+1} = C(x, t_n +$
759 $\Delta t_n)$, for the discretization of time.

760 The derivation of the weak form for the coupled system is shown in Appendix C. For the
761 TR step, the system is advanced by

$$\int_\Omega u_c^{n+\gamma} v_c d\Omega - \gamma \frac{\Delta t_n}{2} \left(A_{\mathrm{NP}}^{n+\gamma} + A_{\mathrm{P}}^{n+\gamma} \right) = \int_\Omega u_c^n v_c d\Omega + \gamma \frac{\Delta t_n}{2} (A_{\mathrm{NP}}^n + A_{\mathrm{P}}^n), \tag{4.8}$$

762 and, for the BDF2 time step we get

$$\int_\Omega u_c^{n+1} v_c d\Omega - \frac{1-\gamma}{2-\gamma} \Delta t_n \left(A_{\mathrm{NP}}^{n+1} + A_{\mathrm{P}}^{n+1} \right) = \frac{1}{\gamma(2-\gamma)} \int_\Omega u_c^{n+\gamma} v_c d\Omega - \frac{(1-\gamma)^2}{\gamma(2-\gamma)} \int_\Omega u_c^n v_c d\Omega. \tag{4.9}$$

763 In Eqs. (4.8) and (4.9), u_c and u_p are trial functions for C and ϕ, respectively, v_c, v_p are
764 test functions for C and ϕ, respectively, and A_{NP} and A_{P} are the linear forms corresponding to the
765 the weak form of $F[C(t), \phi(t), t]$ in Eq. (4.5), and the weak formulation of Poisson's equation,

766 respectively (See Appendix B):

$$A_{\mathrm{NP}} = -D\int_{\Omega}\nabla u_c\cdot\nabla v_c d\Omega + D\int_{\partial\Omega}(\nabla u_c\cdot\hat{\mathbf{n}})\,v_c ds - \mu\int_{\Omega}u_c\nabla u_p\cdot\nabla v_c\Omega + \mu\int_{\partial\Omega}(\nabla u_p\cdot\hat{\mathbf{n}})\,u_c v_c ds \tag{4.10a}$$

$$A_{\mathrm{P}} = -\int_{\Omega}(\nabla u_p\cdot\nabla v_p)\,d\Omega + \int_{\partial\Omega}(\nabla u_p\cdot\hat{\mathbf{n}})\,v_p ds + \frac{q}{\epsilon_{\mathrm{ins}}}\int_{\Omega}u_c v_p d\Omega \tag{4.10b}$$

767

768 4.3 Modeling charge transport in SiO_2

769 To validate the model, we ran transport simulations in SiO_2, to reproduce the experimental
770 trends described by Snow et al. [69]. An initial distribution of Na^+ with a surface concentration
771 $Q_0 = 29\times10^{11}\,/\mathrm{cm}^{-2}$, uniformly distributed over the first 140 Å of a 0.2 µm-thick layer of SiO_2
772 was assumed. The diffusion coefficient of Na^+ was set to $5\times10^{-16}\,\mathrm{cm}^2/\mathrm{s}$ and no-flux boundary
773 conditions for the concentration where set to

$$-D\nabla C - \mu C\nabla\phi = 0 \tag{4.11}$$

774 at $x = 0$ and $x = L = 0.2\,\mu\mathrm{m}$. The gradient of the potential $\nabla\phi$ is obtained self-consistently from
775 (4.4). For the electric potential we set $\phi(x=0) = 10\,\mathrm{V}$ and $\phi(x=L) = 0$. As an initial condition,
776 we set a uniform finite concentration of ions in the layer to a negligible value (we used $C \to$
777 $10^{-20}\,/\mathrm{cm}^3$) and a linear potential drop within the dielectric, consistent with a potential at the gate
778 of $\phi(x=0) = 10\,\mathrm{V}$.

779 Equations (4.8) and (4.9), together with the boundary conditions are solved self consis-
780 tently. At each time step, $\nabla\phi$ was estimated from (4.4), by integrating the latest concentration
781 profile. The mesh was refined closed to the boundaries with a minimum element size $\Delta x = 1.67\,\text{Å}$

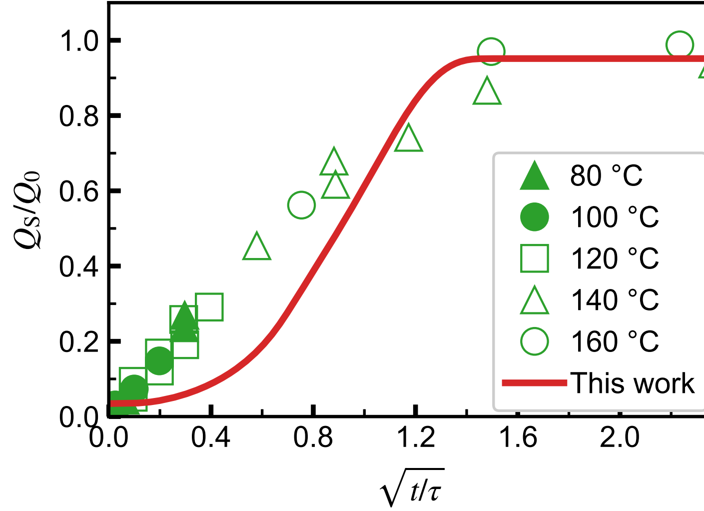

Figure 4.1: Simulated image charge in the semiconductor of a MIS structure as a function of time. Experimental points are taken from Snow et al. [69].

782 and a maximum element size $\Delta x = 6.67\,\text{Å}$. The time step was set to a fixed value of $\Delta t = 50\,\text{s}$ to
783 reduce time truncation error in the TR-BDF2 integration as much as possible. The solution was
784 computed using FEniCS [82, 88] and the auxiliary numerical tools for this framework [89–94].
785 The results for a $\sim 6.25\,\text{h}$ drift-diffusion simulation at a $140\,^\circ\text{C}$ temperature stress are shown in
786 Fig. 4.1. The normalized image charge in the semiconductor as a function of dimensionless time
787 t/τ, predicted by the model is plotted in red, together with the experimental excess surface charge
788 in the semiconductor, reported by Snow et al. [69]. The model successfully predicts a linear rela-
789 tionship of Q_S/Q_0 as a function of $\bar{t} = \sqrt{t/\tau}$ for $\bar{t} \lessapprox 1.4$, after which the curvature changes and
790 the surface concentration saturates. This is consistent with the boundary layer approximation [69].
791 From the boundary layer theory [69]

$$|\frac{Q_S}{Q_0}| \approx \frac{4}{\pi^{3/2}}\left(\frac{t}{\tau}\right)^{1/2}, \text{ for } t \ll \tau \tag{4.12}$$

$$|\frac{Q_S}{Q_0}| \approx 1 - \frac{8}{\pi^2}\exp\left(\frac{t}{\tau}\right), \text{ for } t \gg \tau, \tag{4.13}$$

792 with

$$\tau \equiv 4x_1^2/\pi^2 D.$$

793 The value of x_1 in Eq. (4.14) corresponds to the thickness of the boundary layer. Eq. (4.12) es-
794 tablishes the slope and time constant for the linear and exponential regime. Deviation from the
795 experimental slope arises from a different constant of proportionality originating from (1) the dis-
796 crepancy introduced by the boundary layer width x_1 which is no longer a constant in the numerical
797 simulation and, (2) on the effective magnitude of the electric field when taking the superposition
798 of the applied electric stress and the electric potential due to the ion concentration.

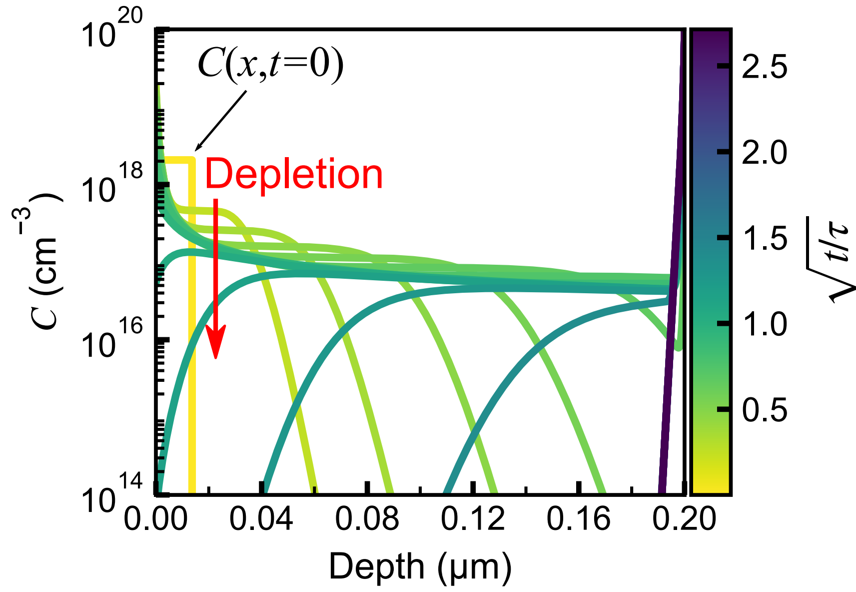

Figure 4.2: Selected concentration profiles corresponding to the image charge plotted in Fig. 4.1.

799 In Fig. 4.2, a selection of concentration profiles used to compute the image charge in
800 Fig. 4.1 is plotted as a function of time indicated in color scale. Shown in yellow is the shape
801 of the initial concentration profile. At early times, we notice that the initial profile is pulled in
802 opposite directions: the image charge at the gate pulls in the negative direction of x, and the applied
803 bias drifts the ions in the positive direction. Because of the balancing effect of the image charge
804 potential and the applied bias, the region closest to the gate is in fact dominated by diffusion. As a
805 consequence of the image charge effect drifting Na^+ driving ions towards the gate, and the applied
806 bias driving ions towards the Si interface, the concentration around the original profile depletes.
807 Then, the magnitude of $\mu \mathbf{E} C$ decreases, leading to slower transit times during the early stages of
808 the simulation, as is evidenced in the region for $t \lessapprox 0.25\,\mathrm{h}$ in Fig. 4.1. At intermediate times,
809 Na^+ piles up at the semiconductor interface driven by the applied bias and the local image charge
810 effect at that interface. Ions are lost from the region around the vicinity of the gate to the drift

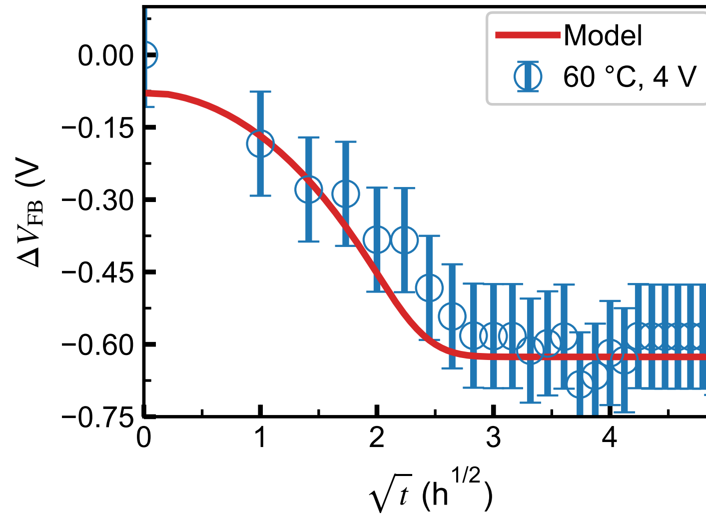

Figure 4.3: Simulated V_{FB} as a function of time for a SiO_2 MIS structure using $D = 4 \times 10^{-17}\,\mathrm{cm^2/s}$. Empty circles indicate the experimental results of samples stressed at 60 °C under a bias of 4 V.

811 dominated region, driven by a large concentration gradient close to this interface. This causes
812 further depletion of the gate interface, which is identified by profiles with positive concentration
813 gradients moving towards the semiconductor interface. This result quantitatively describes the
814 kinetics of Na migration in MIS structures, suggesting that the initial concentration profile might
815 lay further into the bulk of SiO_2 (leading to lower initial concentration which in turn reduces image
816 charge effect at the gate).

817 To provide further validation of the model with more recent experimental data, following
818 the experiment by Snow et al. [69], we prepared SiO_2 MIS capacitors by dry oxidation of n-type
819 Si (100) wafers at a temperature of 1100 °C. Prior to oxidation, the silicon wafers were cleaned
820 with acetone, ethanol and isopropyl alcohol, followed by RCAI and RCAII cleaning procedures.
821 The thickness of the SiO_2 layer was mapped by spectroscopic ellipsometry. An average thickness
822 of 100 nm was measured. Sodium contamination was introduced by thermal evaporation at 800 °C

823 from a NaCl source, followed by contact deposition without breaking the vacuum. The rate of
824 deposition of the NaCl layer was monitored using a quartz microbalance up to value of 25 nm.
825 A pattern of $\sim$ 1 mm diameter circles with a pitch of 2.54 mm was deposited using a shadow
826 mask. Approximately 200 nm of aluminum were deposited as front and back contacts. The bottom
827 surface of the wafer was swabbed with hydrofluoric acid prior to metallization.

828 The as-prepared samples were subject to a bias-temperature stress of 60 °C and 4 V in
829 intervals of 1 h. Between stress intervals, the samples were cooled down to room temperature and
830 capacitance-voltage measurements were collected. The flatband voltage shift ΔV_{FB} was extracted
831 as described in our previous work [62].

832 To simulate the transport of Na^+ in the SiO_2 MIS capacitor, we used a $Q_0 = 1.4 \times 10^{11}\,\mathrm{cm}^{-2}$.
833 This value was selected based on a quick estimation of the expected saturation $V_{\mathrm{FB}} \approx -0.6\,\mathrm{V} \approx$
834 $-Q_0/\epsilon_{\mathrm{ins}}L$ from the experimental results. A diffusivity of $4 \times 10^{-17}\,\mathrm{cm}^2/\mathrm{s}$ was used to match the
835 temporal dependence of ΔV_{FB}. For comparison, this value is two orders of magnitude larger than
836 the one we would expect from the extrapolation of the Arrhenius relationship reported by Frischat
837 [95] taken within the range of 170 °C to 250 °C for commercial SiO_2 glasses. The initial concentra-
838 tion profile was set to reach a 25 nm depth from the gate, in accordance to the monitored thickness
839 during NaCl evaporation. As can be seen in Fig. 4.3, the simulated profile matches well the exper-
840 imental data within errorbars. For consistency with Fig. 4.1, the results were plotted against $t^{1/2}$.
841 In this representation, a quadratic dependence of ΔV_{FB} is indicative of drift-dominated transport.

4.4 Behavior before the characteristic transit time

In section 3.6, the concept of characteristic transit time was introduced to account for a simplified behavior whenever the concentration was below the threshold value $C_{\text{th}} \equiv 2\epsilon_{\text{ins}}/qL^2V_{\text{stress}}$. To cross reference our transport model with this behavior at short times and under low concentrations we modified the boundary conditions to accommodate for a constant source of ions at the gate. Then, we ran simulations on a MIS structure with a thickness of 80 nm at a temperature of 80 °C, with an applied bias of 4 V. The corresponding concentration profiles as a function of time are shown in Fig. 4.4, where the drift-diffusion time is indicated in color scale. Fig. 4.4(a) illustrates the transport kinetics at short times as modeled by the numerical solution to Poisson-Nernst-Planck coupled system with a constant source and a closed boundary at the semiconductor interface. The estimated characteristic time for this system is $\tau_c \approx 8.4\,\text{h}$, beyond which the concentration profile begins to pile up at the semiconductor interface, due to the effect of drift and accumulation of negative image charges in the semiconductor. As expected from the boundary conditions, we do not see depletion at the metal gate interface, in contrast with the closed system described is Section 4.3. In fact, when $t < \tau_c$, this boundary condition behaves identically to the approximation at short times given by (3.7), shown in Fig. 4.4(b). A variation of only 2.8 mV in V_{FB} at $t = \tau_c$ was estimated between the two models, which is less than the thermal voltage $k_{\text{B}}T \approx 30\,\text{mV}$ at the simulated temperature. This is expected due to the fact that, for the given bias and thickness, our threshold concentration is $C_{\text{th}} \approx 5 \times 10^{17}\,\text{cm}^{-3}$, compared to our average concentration of $10^{16}\,\text{cm}^{-3}$.

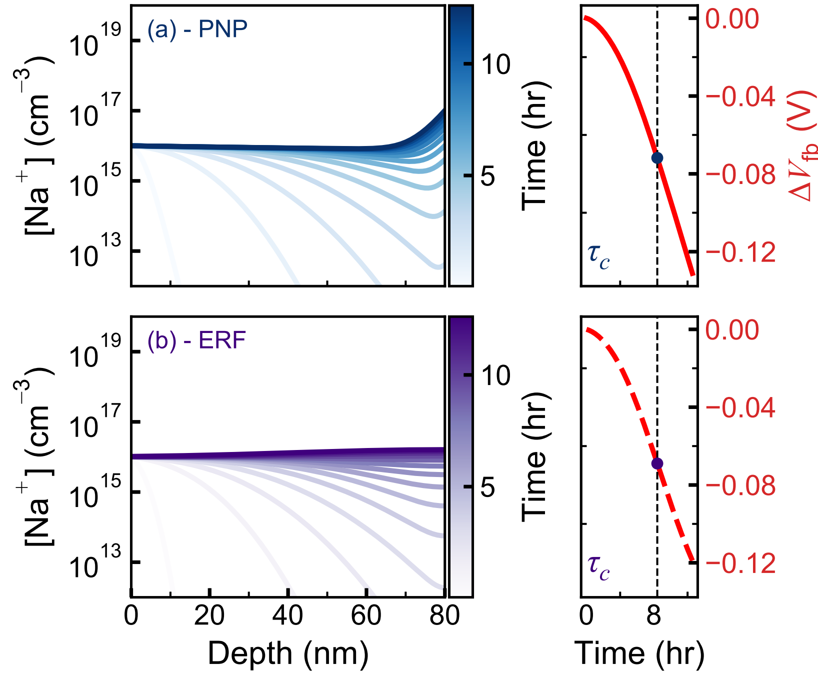

Figure 4.4: Concentration profiles as a function of time, indicated in color scale, modeled by (a) a FEM simulation of the full Poisson-Nernst-Planck coupled system (PNP) and (b) the approximate solution (ERF) at short times given by (3.7). To the right of each pane is plotted the corresponding ΔV_{FB} due to the ionic charge distribution as a function of time. In the same plot is indicated the characteristic transit time within the approximation described in Sec. 3.6. The difference between the estimated V_{FB} at $t = \tau_c$ is of only 2.8 mV.

862 ## 4.5 Na transport in stacks of materials

863 The finite element implementation of the present model can be easily re-formulated to study
864 the kinetics of transport of ionic species in stacks of materials. We can model the transport of Na^+
865 through the dielectric and into the silicon, by treating both systems independently, and connecting
866 them with a flux boundary condition. Given the discontinuity in the diffusion coefficients, impurity
867 equilibrium concentrations and electrical properties in the layer stack, segregation needs to be
868 considered. To account for impurity segregation at the dielectric/semiconductor interface we use a

869 phenomenological, first order kinetics description of the flux [96]:

$$J_s \equiv h\left(C_{\text{ins}}(L,t) - \frac{C_{\text{Si}}(L,t)}{m}\right), \tag{4.14}$$

870 where L is the thickness of the insulating film, $C_{\text{ins}}(L,t)$, $C_{\text{Si}}(L,t)$ are the impurity concentrations
871 defined in the insulator and in the semiconductor, respectively, h is the surface mass transfer coef-
872 ficient given in units of distance over unit time, and

$$m \equiv \left(\frac{C_{\text{Si}}}{C_{\text{ins}}}\right) \quad \text{in equilibrium} \tag{4.15}$$

873 is the segregation coefficient.

874 The total flux at $x = L$ from the dielectric side is given by

$$-D_{\text{SiN}}\nabla C - \mu C\nabla\phi = \mathbf{J}_s. \tag{4.16}$$

875 Because silicon is assumed to have an electrical resistivity several orders of magnitude
876 less than the insulating films (from $\sim 10^{-3}\,\Omega\,\text{cm}$ to $\sim 10^{5}\,\Omega\,\text{cm}$, compared to typical insulating
877 resistivities on the order of $10^{11}\,\Omega\,\text{cm}$), it is possible to neglect drift in silicon. As it turns out, in
878 PV devices, the high doping concentration of the emitter side puts an upper bound on the resistivity
879 of Si on the order of $10^{-2}\,\Omega\,\text{cm}$. Hence, transport in silicon is governed by pure diffusion. And
880 the total flux at $x = L$ from the side of silicon is given by

$$-D_{\text{Si}}\nabla C = \mathbf{J}_s. \tag{4.17}$$

881 Eqs. (4.16) and (4.17) are introduced easily as Neumann boundary conditions on the surface
882 element terms ds in Eq. (4.10).

883 Incoming flux at the metal gate interface can also be easily instrumented in the model by
884 considering a source of ions with surface concentration S given in atoms per unit area flowing in

885 to the insulating layer at a rate k in units of inverse time:

$$J_{\text{source}} = kS \tag{4.18}$$

886 To account for the finite size of the source, we consider that the source is depleted after a time $1/k$
887 after which we set $J_{\text{source}} = 0$.

888 To demonstrate transport through stacks of materials, we simulated the kinetics of Na^+
889 through the SiN_x/Si stack by means of Eqs. (4.8) and (4.9), and setting the boundary conditions
890 defined by equations (4.16), (4.17) and (4.18). The thickness of the SiN_x was set to 75 nm, in
891 accordance to typical values used in PV modules [27]; and the thickness of silicon was set to 1 µm
892 which is long enough to be considered infinite within the timescale of the simulation (96 h) for
893 the selected value of the diffusivity of Na in Si. We set the temperature to 85 °C and considered
894 a diffusivty of Na^+ in SiN_x of $\sim 4\times10^{-16}\,\text{cm}^2/\text{s}$ in accordance to our trapping-corrected BTS
895 estimates (Gastrow et al. [62]), and a value of $10^{-16}\,\text{cm}^2/\text{s}$ for the diffusivity of Na in Si. The latter
896 is larger than the expected values of $\sim 10^{-21}\,\text{cm}^2/\text{s}$ from extrapolation of experimental Arrhenius
897 curves taken at temperatures above 1000 °C [97], but lower than the bounds estimated based upon
898 typical failure times of PID-s affected PV modules, which put an upper bound of $\sim 10^{-7}\,\text{cm}^2/\text{s}$
899 [98]. An electric stress of 75 mV was applied, corresponding to an electric field of 10^4 V cm,
900 which is in range with the estimations from the voltage divider model shown in Table 2.1, for
901 low resistivity nitrides. For the source term, we chose a surface concentration of $S = 10^{10}\,\text{cm}^{-2}$
902 which is two orders of magnitude less than the values corresponding to intentional contamination
903 in [32, 69], and a rate of ingress $k = 10^{-5}\,\text{s}^{-1}$, for which the source is partially depleted within the
904 simulation time of $\sim 3.5\times10^5$ s (96 h). For the segregation flux, we used a surface mass transfer
905 coefficient of $h = 10^{-12}\,\text{cm}\,\text{s}^{-1}$ and a segregation coefficient $m = 1$. The results are plotted in

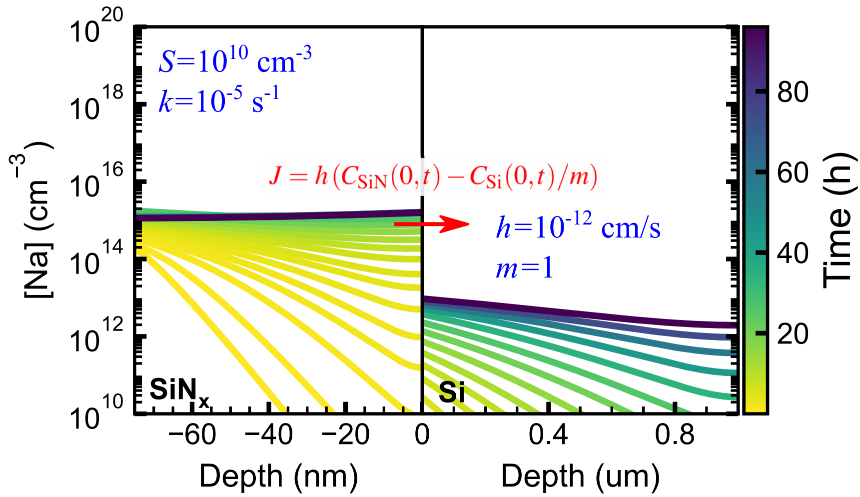

Figure 4.5: Simulated concentration profiles as a function of time across a SiN^x/Si material stack.

Fig. 4.5, where the concentration profiles are shown as a function of time in color scale. Notice that, because the flux at the source is maintained constant and the rate is $k = 10^{-5}\,\mathrm{s}^{-1}$, depletion becomes evident after the $\sim 28\,\mathrm{h}$. In fact, the concentration profile almost flattens within the SiN_x over the course of the simulation. Furthermore, because the diffusion coefficient in the silicon is set to a higher value ($10^{-14}\,\mathrm{cm}^2/\mathrm{s}$) with respect to the value in SiN_x ($4 \times 10^{-16}\,\mathrm{cm}^2/\mathrm{s}$), Na^+ is transferred to silicon and is diffused into the bulk of Si relatively easily. Additionally, due to the low magnitude of the electric field in SiN_x, no accumulation of Na is observed at the SiN_x/Si interface, and ionic transport in the dielectric film is dominated by diffusion, as can be observed in Fig. 4.5, by the slopes of the concentration profiles.

915 ## 4.6 Conclusions

916 We developed a model to simulate the kinetics of ion diffusion in MIS devices. Validation
917 with experimental results resulted in good agreement of the simulated trend of the image charge
918 in the semiconductor interface. Reference with BTS experiments also results in agreement of the
919 predicted ΔV_{FB} due to ion migration. Under the limiting case of low concentration and short times,
920 we verified that the solution can be correctly approximated using a constant electric field which
921 simplifies to a pure diffusion problem, as described in Sec. 3.3. The estimated solution to Poisson-
922 Nernst-Planck coupled system yields all the information required to study ion transport kinetics
923 with respect to the the charge distribution. This is especially important to visually understand
924 the assumptions behind boundary layer theory and extend upon it. Our model allows for direct
925 extrapolation to other type of dielectric structures and material stacks which are of interest for
926 modeling reliability of semiconductor devices.

927 Chapter 4, in part, is being prepared for submission in the *Journal of Applied Physics*
928 under the title "Numerical Solution to Poisson-Nernst-Planck Equations for Ion Transport in MIS
929 structures and Solar Cells" by E. Martinez-Loran, G. von Gastrow, J. Clenney, F. Contreras-Torres,
930 R. Meier, M.I. Berton, P. Bandaru and D.P. Fenning. The dissertation/thesis author was the primary
931 investigator and author of this paper.

5 | Device degradation modeling

The photovoltaic industry has made huge efforts to engineer efficient and reliable solar modules and to test the long-term performance of modules. Reliability tests have shown potential-induced degradation can lead device failure before the average warranty time in silicon solar modules [1, 3–5]. Over the last decade, much work has been put to standardize reliability tests [5, 7, 14, 24, 27, 68, 99–102] and to develop predictive models to estimate the progression of PID [14, 15, 68].

5.1 Introduction

Power law models have demonstrated some use to describe the loss in power output, [21, 36, 38, 68] albeit with limitations on the applicability to weeks-long simulations. Since PID in p-Si solar modules has been ascribed to electrical shunting of the emitter, empirical models describing the progression of the shunt resistance R_{sh} have phenomenologically described the progression of R_{sh} with stress time, and even incorporated environmental conditions [14, 29, 103]. More recently Schulze et al. [15], proposed a simplified drift-diffusion model of a shunt that adequately fits the PID progression and recovery in R_{sh} for p-Si modules. While this model provides insights into the physical parameter space that impacts ion transport and can potentially be engineered to

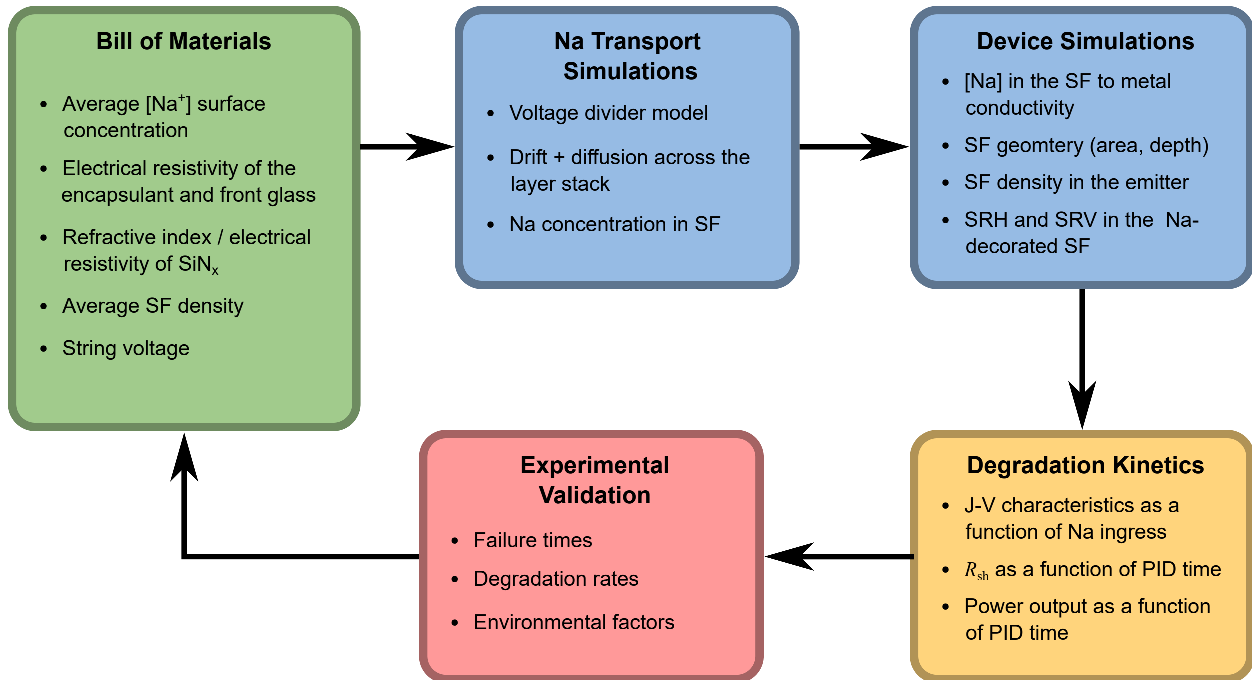

Figure 5.1: Proposed modeling framework aimed at predicting PID-s and engineering PID-robust PV modules.

948 reduce PID, the introduced level of simplification weakens the connection to describe engineerable
949 parameters, which can be determined through the bill of materials.

950 The assumed mechanism behind PID-s in p-Si PV modules is that Na contamination from
951 different depths in the module migrates to the silicon emitter where it is responsible for shunting
952 behavior [5, 9, 12, 13, 18, 19]. Microscopy analyses have established that Na-decorated {111}
953 stacking faults in p-type silicon lead to the formation of electrical shunts in the emitter of the solar
954 cell leading to PID [12, 19]. It has been proposed that the introduction of Na in these defects occurs
955 through electric-field assisted transport, whereupon Na contamination in the silicon nitride (SiN_x)
956 anti-reflective coating of the solar cell moves towards the emitter of the solar cell [12]. Once Na
957 reaches silicon, it tends to concentrate in the {111} stacking faults [9, 12, 13, 19]. These defects
958 shunt the p-n junction and result in the loss of carrier collection efficiency [9, 12, 19, 104].

959 In this chapter we describe a mechanistic model to describe the formation of the electrical

960 shunts in the module which takes in to account the full kinetics of ion transport formulated in
961 Chapter 4. The present model allows to parametrize the power output degradation and R_{sh} in terms
962 of intrinsic properties, like the diffusion coefficients of Na in the different layers, and engineerable
963 parameters like the resistivity of the encapsulant layer and the incorporation of blocking layers
964 between the SiN_x and the Si emitter.

965 The overarching goal of this modeling framework is to develop a full physical analysis
966 aimed at understanding the impact of the properties of the materials in the PV modue, the operating
967 voltages, and environmental conditions in PID-s. As proposed in Fig. 5.1, this iterative analysis
968 allows a comprehensive study of the multiple factors leading to PID-s. This methodology will
969 provide guidance to optimize the bill of materials for PID-robust PV modules. The proposed inputs
970 of the model are the electrical resistivity of the front-cover glass, encapsulant layer and SiN_x. As
971 a proxy for the electrical resistivity of SiN_x, refractive index measurements have shown good
972 correlation with PID-s resistance [5, 27, 59, 74, 105, 106]. Also of interest, is the average surface
973 concentration of stacking fault defects in the emitter of the module and, the string voltage, which
974 determines to what extent ions drift towards the emitter. These parameters can be used in transport
975 simulations to model the ingress of Na through the module stack and determine the concentration
976 profile of Na in the stacking faults. The Na concentration in the defect and this information,
977 together with the area of the shunt and density of defects is mapped to a shunt conductivity and
978 the kinetics model is used by a device simulation tool that determines the current-voltage (J-V)
979 characteristic of the PV module. The kinetics of degradation is then estimated by analyzing the
980 J-V characteristic of the device. Simulated R_{sh} and power output is subsequently validated against
981 experimental data.

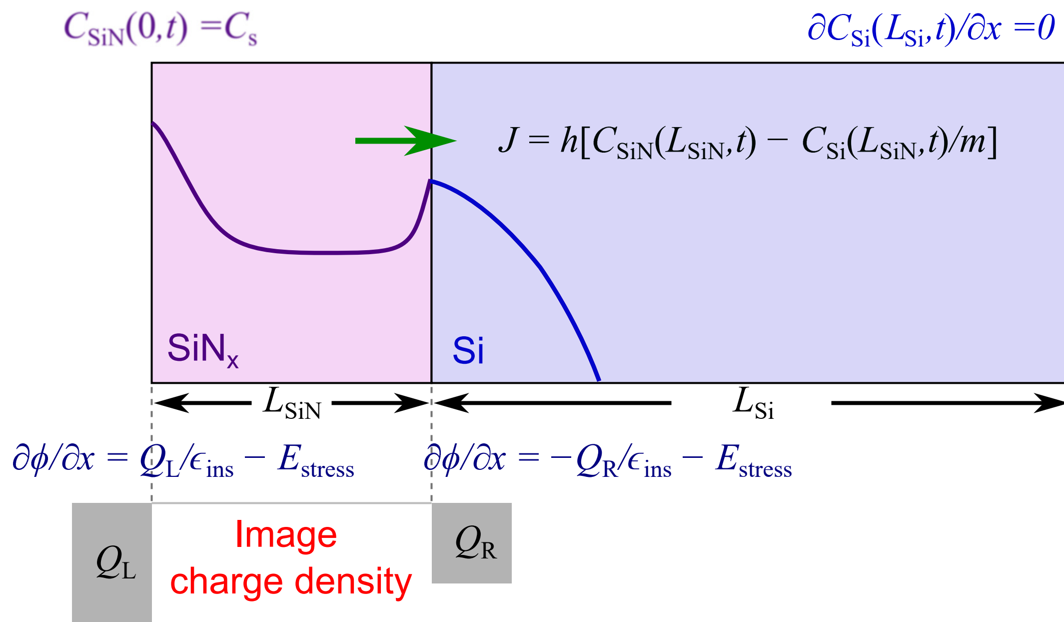

Figure 5.2: Boundary conditions used for Na transport simulations in p-Si PV modules. As a first approximation we set a constant source boundary condition at the EVA/SiN_x located at $x = 0$. At the bottom of Si, located at $x = L_{Si}$, a zero-flux boundary condition is imposed. The two materials are connected by a first order kinetics segregation flux boundary condition. The boundary condition for the electric potential is determined by the electric field induced by the image charges at the EVA and Si interfaces, due to the Na^+ concentration in SiN_x.

5.2 Modeling Na migration kinetics

In PID-s, Na contamination is assumed to reach the n^+-Si emitter of the PV module, where it "decorates" the stacking faults, after migrating through the encapsulation and the SiN_x anti-reflective coating. The process is driven by the large potential difference between the cell at a floating negative potential $V \geq 1000\,\mathrm{V}$ and the metal frame which is grounded at $V = 0$ [5, 12].

We assume that the electric field in the module stack can be estimated on the basis of the voltage divider introduced in Sec. 1.4. In Table 2.1, we show typical ranges of the equivalent electric field in each material of the PV module, based on typical values of the thickness.

The origin of Na contamination in solar modules has been historically ascribed to the front cover soda-lime glass [4, 5, 7]. For instance, it has been shown that replacement of soda-lime glass with a quartz glass widow mitigates pseudo fill factor losses in Si modules subject to damp heat-PID tests [7, 18]. Nevertheless, more recent reports show that PID can occur in the absence of a front-cover glass and even in the absence of an encapsulant [23–25]. This suggests that Na contamination might have been introduced during lamination of the module. This hypothesis has been supported by the presence of Na contamination within EVA, particularly, close to the EVA/SiNx interface, prior to PID testing [26]. In Sec. 2.2 we provided further evidence that, migration through the EVA might have a limited impact on PID-s due to the fact that Na does not drift through the whole thickness of the encapsulant in the time scale of PID degradation. Therefore, we assume that Na contamination is present at the EVA/SiN_x prior to PID stressing.

It is assumed that PID-s occurs by Na contamination present at the EVA/SiN_x interface being drifted through the SiN_x anti-reflective coating and diffused into the n^+-Si emitter of the PV

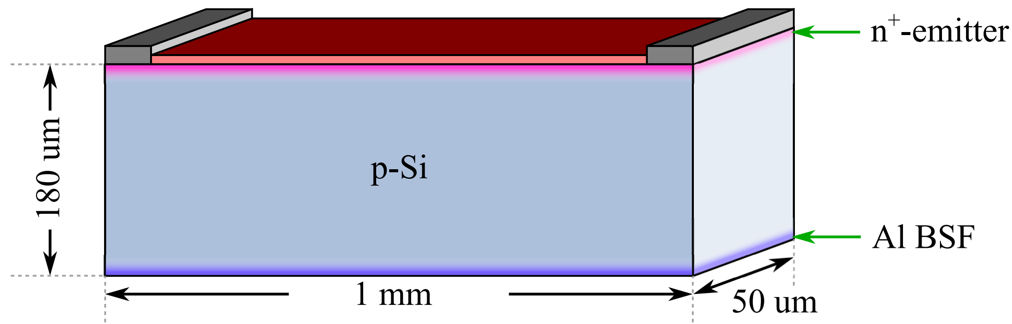

Figure 5.3: Schematic of the Aluminum Back Surface used to simulate the module degradation.

module. Transport in SiN_x is governed by drift and diffusive flux. The relative contribution of the drift and diffusive terms is determined by the magnitude of the electric field in the SiN_x.

Transport is then simulated using the FEM modeling framework described in Sec. 4.5. The boundary conditions that we used are described in Fig. 5.2. For small source concentrations, we assume that a constant source boundary condition can suffice to describe ion ingress at the EVA/SiN_x interface. At the bottom of the Si simulation volume, we impose a zero-flux boundary condition. Transport is modeled independently in each layer with a coupling boundary condition given by a first order kinetics segregation flux [96]. The electric field is assumed to be negligible in the n^+-Si emitter, hence transport is well described by pure diffusion in this material. In SiN_x, the electric stress is usually non-negligible and transport is governed by Nernst-Planck's equation. Due to the introduction of Na^+, the electric potential is determined by the superposition of the applied bias and the potential induced by the Na^+ charge distribution. Therefore, as discussed in Sec. 3.6, the complete solution for times $t > \tau_c$ is coupled to the solution of Poisson's equation for the charge distribution in SiN_x. We set the Neumann boundary conditions to the electric potential self-consistently, based on the determination of the image charges at the EVA and Si interface due to the Na^+ concentration profile.

5.3 Device simulations

To determine the amount of degradation as a function of Na ingress into the silicon substrate, we model the effect of introducing an electrical shunt in the emitter of a typical p-Si, aluminum back surface field (Al-BSF) PV module. The schematic of the simulated devices is shown in Fig. 5.3. The boron concentration in the base, emitter phosphorus concentration and Al-BSF concentration used in the simulation are listed in Table 5.1. Both, the emitter and Al-BSF are defined using a Gaussian concentration profile which reaches a value of $10^{16}\,\mathrm{cm}^{-3}$ at a depth of 300 nm from the front and back surfaces, respectively. Device simulations are performed using Synopsys Sentaurus FEM solver[1]. Carrier generation is estimated using OPAL[2] at 1 Sun, considering an SiN_x anti-reflective coating of 75 nm. Shockley-Read-Hall bulk recombination is activated and a bulk lifetime of 5 ms. The selected bulk lifetime is consistent with several reports of high quality float zone Si wafers at the same level of doping [107]. The surface recombination velocity at the SiN_x/Si interface was estimated using Altermatt's parametrization [108], and Fermi–Dirac statistics is activated to account for the large doping concentration at the emitter.

To model PID-s, we introduce a metallic structure within the emitter of the cell as illustrated in Fig. 5.4. We define the conductivity profile along the SF according to the spreading resistance measurements taken by Korol [97] on Na-implanted silicon. To avoid introducing spurious shunting at early stages of the simulation due to the presence of a metallic structure, we neglected the regions of the shunt with conductivity less than $10^{-10}\,\mathrm{S\,cm}^{-1}$. Concentration profiles as a function of time were modeled according to the parameters in Table 5.1.

[1]http://www.synopsys.com/home.aspx

[2]https://www2.pvlighthouse.com.au/calculators/OPAL 2/OPAL 2.aspx

Table 5.1: Parameters used to model transport across the SiN_x/Si stack.

Parameter	Symbol	Value	Units
Simulation temperature	T	85	°C
Thickness of SiN_x	L_{SiN}	75	nm
Thickness of Si	L_{Si}	1	µm
Electric field in SiN_x	E_{SiN}	0.5	$MV\,cm^{-1}$
Electric field in Si	E_{Si}	0	$V\,cm^{-1}$
Diffusion coefficient of Na^+ in SiN_x [a]	D_{SiN}	4×10^{-16}	cm^2/s
Concentration of the source	C_s	10^{16}	cm^{-3}
Doping concentration in the p-Si base	N_A	10^{16}	cm^{-3}
Doping concentration in the n-Si emitter	N_D	10^{19}	cm^{-3}
Al-BSF doping level	N_D	10^{19}	cm^{-3}
Surface mass transfer coefficient at the SiN_x/Si interface	h	10^{-12}	$cm\,s^{-1}$
Segregation coefficient at the SiN_x/Si interface	m	1.0	-

[a] Based on high resistivity SiN_x measurements Gastrow et al. [62].

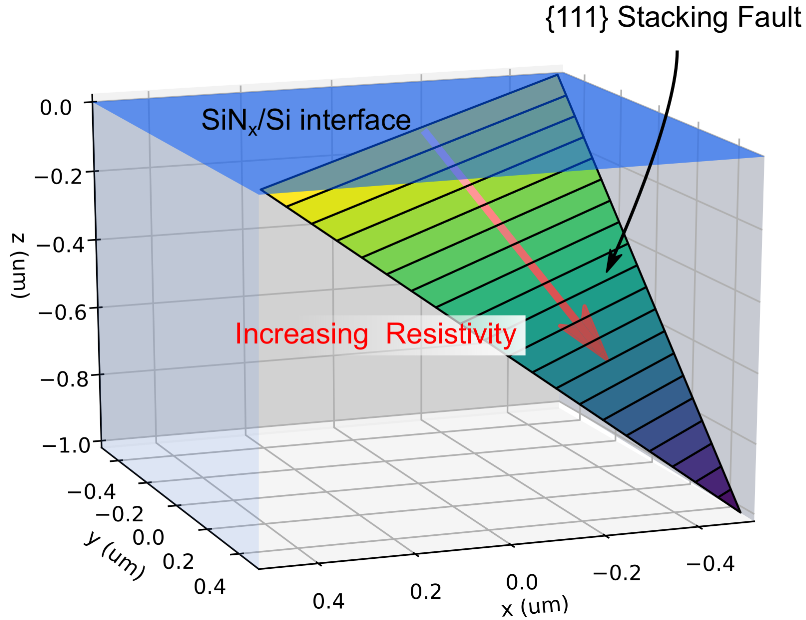

Figure 5.4: Schematic of a metallic shunt introduced in the n^+-Si emitter of the PV module to model PID-s. The triangular plane represents a metallic region over a {111}-stacking fault, with a resistivity profile determined by the Na concentration.

1039 Fig. 5.5 shows a PID-s kinetics simulation for a device stressed at 85 °C under a voltage
1040 equivalent to $0.5\,\mathrm{MV\,cm^{-1}}$, according to the parameters described in Table 5.1. Fig. 5.5(a) shows
1041 the corresponding concentration profiles in the module stack used in the determination of the shunt
1042 conductivity and subsequently, to simulate the J-V characteristic. Due to the small value of the
1043 surface mass transfer coefficient ($h = 10^{-12}\,\mathrm{cm\,s^{-1}}$), sinking into the emitter occurs at a slower
1044 rate, compared to the rate at which ions drift within the SiN_x. This leads to a build-up in the
1045 concentration on the SiN_x side of the SiN_x/Si, which reaches concentrations up to $\sim 10^{19}\,\mathrm{cm^{-3}}$.
1046 For the selected value of the diffusion coefficient of Na in the SF, Na reaches concentrations $\gtrapprox$
1047 $10^{14}\,\mathrm{cm^{-3}}$ within a few hours leading to values of the conductivity $\gtrapprox 10^{-3}\,\mathrm{S\,cm^{-1}}$ within the *p-n*
1048 junction of the device, as can be seen in Fig. 5.5(b). The simulated J-V characteristic due to PID
1049 is shown in Fig. 5.5(c). The first J-V curve shown in bright yellow, at time zero corresponds to
1050 the device in the absence of the shunt. Below the threshold value of $\sigma_{\mathrm{shunt}} < 10^{-3}\,\mathrm{S\,cm^{-1}}$, only a

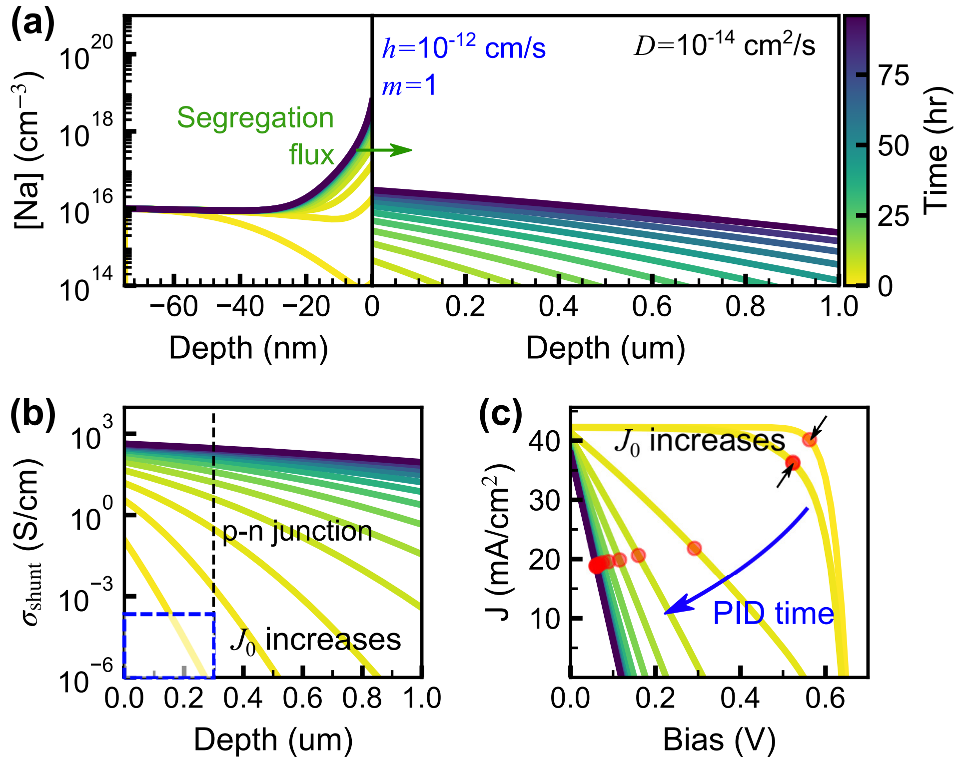

Figure 5.5: Simulated PID-s kinetics degradation for device stressed at 85 °C under a voltage equivalent to $0.5\,\mathrm{MV\,cm^{-1}}$. (a) Shows the corresponding Na concentration profiles as a function of PID stress indicated in color scale. Accumulation at the Si interface occurs due to the effect of the segregation flux allowing only a fraction of Na to sink into the n^{+}-Si emitter. In Si, Na transport is entirely governed by diffusion. For the selected value of the diffusion coefficient of Na in the SF ($10^{-14}\,\mathrm{cm^2/s}$), Na reaches the *p*-*n* junction of the devices in a few hours. (b) The corresponding conductivity from the Na concentration in the Si emitter, estimated from spreading resistance measurements by Korol [97], (c) Simulated J-V characteristic as a function of PID time for device. For short times, before the conductivity reaches the value of $10^{-3}\,\mathrm{S\,cm^{-1}}$, the device loses efficiency by increased recombination. Indicated in red circles is the maximum power point P_{mpp} for each curve.

1051 loss of fill factor is observed. This is assumed to be due to an increase in the diode recombination
1052 current. Once this threshold is surpassed, an unambiguous decrease in R_{sh} is seen at further times,
1053 as expected in PID-s. Note that the $42\,\text{mA}/\text{cm}^2$ short circuit current (J_{sc}) is due to the fact that no
1054 surface recombination current is considered for the contacts of the cell. This fact does not change
1055 the analysis, since the kinetics is estimated normalizing with respect to the initial performance
1056 metrics (e.g. R_{sh} and P_{mpp}) of the device.

1057 5.4 Bounding the value of the diffusion coefficient of Na in the 1058 SF

1059 From the simulated J-V characteristic like the one shown in Fig. 5.5, it can be seen that a
1060 threshold value of the conductivity at the vicinity of the *p*-*n* junction is required in order to observe
1061 PID. This indicates that, in order to observe PID, the diffusion length of Na in Si should be around
1062 the value of the depth of the *p*-*n* junction. It follows that this requirement can be used to set the
1063 bounds of the diffusivity of Na in the stacking fault, by using order of magnitude analysis.

1064 Robust device simulations require full 3D implementation to avoid current collection losses
1065 artificially introduced by reduction of current pathways in 2D simulations. This increases the com-
1066 putational load due to the large number of elements required to adequately capture the physics
1067 on elements of very dissimilar scales. For instance, the dimensions of the quasi-2D shunt give
1068 elements with minimum mesh size of 5 nm, while the distance between finger electrodes is 1 mm.
1069 To reduce computational time, when working with numerous parameter scans, we recreated the
1070 FEM model, by means a, Machine Learning algorithm that uses the concentration profiles as pre-

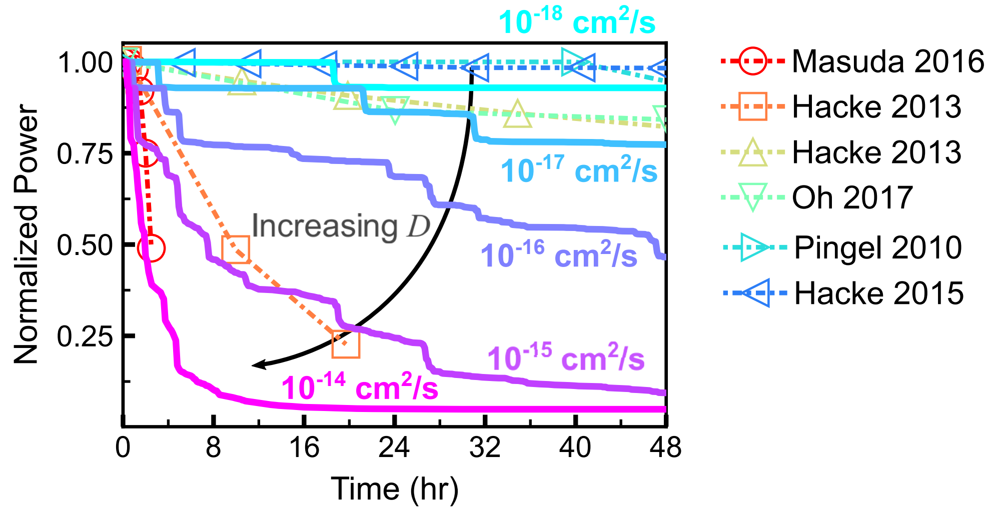

Figure 5.6: Simulated PID-s progression as a function of Na diffusivity in the stacking fault D_{SF} for a PV module stressed at 85 °C and a voltage stress equivalent to a 0.5 MV cm^{-1} in the SiN_x film. Failure time decreases with increasing D_{SF}, from being less than 10 %, within the timescale of the simulation for $D_{SF} = 10^{-18}\,cm^2/s$, to less than 4 h in the case of $D_{SF} = 10^{-14}\,cm^2/s$. For reference, experimental PID-s reported for similar temperatures and device architectures are plotted alongside: Masuda et al. [35] (2016), Hacke et al. [36] (2013), Oh et al. [37] (2017), Pingel et al. [5] (2010), Hacke et al. [38] (2015).

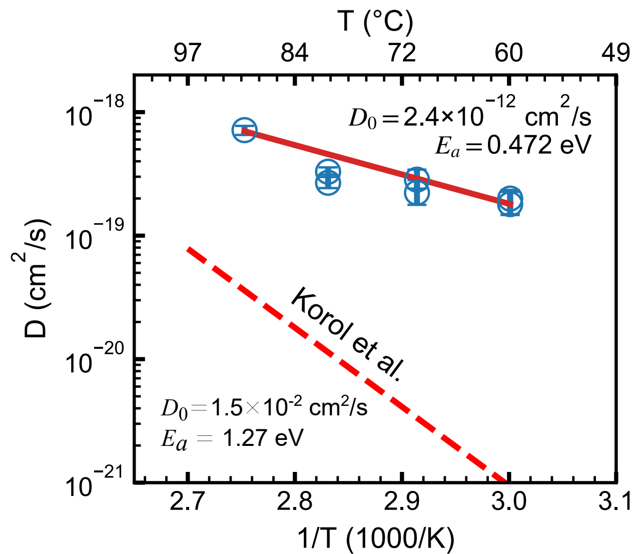

Figure 5.7: Arrhenius relationship for the diffusion coefficient of Na in Si, as estimated from fitting SIMS profiles of thermally diffused Na in n-Si wafers. For reference, the dashed red curve represents an extrapolation from from Arrhenius curves within the range of 350 to 800 °C by [97]. Adapted from Clenney et al. [109].

dictors and previously computed P_{mpp} as targets. This is justified, since device simulations do not explicitly incorporate ion transport kinetics, and the characteristic J-V is only a function of the shunt conductivity for the geometry shown in Fig. 5.4, albeit this approach is specific to the device geometry defined in 5.3. To implement this, we used the Scikit-learn [110] library distributed with Python to train a Random Forest regressor with a set of 121 concentration profiles ($\approx$70 %) an their respective P_{mpp} from a total sample size of 172 simulations. We tested the regressor against the remaining dataset of 52 profiles ($\approx$30 %) with their respective P_{mpp}, from which we got a coefficient of determination [111] $R^2 = 0.999$ for P_{mpp}.

In order to bound the values of D_{SF}, we used the trained model to predict the decay in the maximum power from the simulated concentration profiles of devices stressed according to the parameters in Table 5.1. The diffusion coefficient of Na in the SF is varied logarithmically from 10^{-18} to $10^{-14}\,\mathrm{cm^2/s}$. Fig. 5.6 shows the simulated power output (P_{mpp}) normalized to the initial P_{mpp} as a function of PID time, for different values of D_{SF}. As expected, failure time decreases with increasing D_{SF}, from a few hours for $D_{\mathrm{SF}} = 10^{-14}\,\mathrm{cm^2/s}$, to the order of days for $D_{\mathrm{SF}} = 10^{-18}\,\mathrm{cm^2/s}$. Overlayed in Fig. 5.6 are experimental degradation times reported for p-Si PV modules stressed under similar conditions reported by Pingel et al. [5], Masuda et al. [35], Hacke et al. [36], Oh et al. [37], and Hacke et al. [38]. Comparison with literature data for PID-susceptible devices like the ones reported by Masuda et al. [35], indicates that the upper bound for D_{SF} is of the order of $10^{-14}\,\mathrm{cm^2/s}$. It is notable that the devices which experience faster degradation kinetics (Masuda et al. [35] and Hacke et al. [36]) are multi-crystalline Si modules, whereas devices exhibiting smaller degradation rates (Pingel et al. [5], Oh et al. [37], and Hacke et al. [38]) are mono-crystalline devices. Recent results from *ab-initio* calculations on the interstitial barrier for Na diffusion in intrinsic stacking faults suggested that diffusion along the extend defects

might have a larger energy penalty than bulk diffusion [112]. This result seemed to indicate that the mechanism behind shunt decoration is dominated by bulk diffusion followed by segregation to the intrinsic SF. Fig. 5.7 shows the Arrhenius relationship of Na diffusivity in Si as obtained by fitting the diffusion profiles of Na measured by SIMS [109]. Based on SIMS measurements, the expected diffusivity of Na in the bulk of Si is $\approx 3 \times 10^{-19}\,\mathrm{cm^2/s}$ at 85 °C [109], which contrasts with the upper bound of $10^{-14}\,\mathrm{cm^2/s}$ required to match the degradation kinetics seen on multicrystalline samples [35]. Our result indicates that segregation to the SF from bulk-diffused Na is incompatible with the timescales associated with degradation in PID-prone devices. This suggests a diffusive mechanism through the SF as described by the DFT calculations by Ziebarth et al. [113], in which the energetic barrier for interstitial diffusion along the SF is lowered for a filled defect, driven by an increase in the Si–Si bond distance.

5.5 Finite Source Analysis

The considerable amount of Na accumulation in SiN_x near the Si interface shown in Fig. 5.5 (reaching concentrations $> 10^{18}\,/\mathrm{cm^{-3}}$) is in part due to the low value of h ($10^{-12}\,\mathrm{cm/s}$) used in the simulation. However, a significant contribution to the accumulation comes from the fact that we have assumed an infinite reservoir of Na^+ keeping the concentration C_s fixed at all times. A more physical assumption is to consider the effect of a finite source by means of Eq. (4.18),

$$J_{\mathrm{source}} = kS$$

where a constant flux of Na^+ at the source is given by the product of a rate of ingress k and a surface concentration S.

Table 5.2: Parameters taken as the reference base case in PID kinetics simulations

Parameter	Value	Units	Consideration
T	85	°C	Accelerated testing
E	10^4	V/cm	Within the order of magnitude of the upper bound in Table 2.1.
D_{SiN}	4×10^{-16}	cm^2/s	Ref. [62] (at 85 °C).
D_{SF}	10^{-14}	cm^2/s	Upper bound from Sec. 5.4.
S	10^{10}	cm^{-2}	Two order of magnitude less than intentionally contaminated devices in Wilson et al. [32].
k	10^{-4}	s^{-1}	Depletion of the source within the first 24 h.
h	10^{-12}	$cm\,s^{-1}$	Inefficient leakage to Si
m	1	–	No jump discontinuity.
L_{SiN}	75	nm	Ref. [34]
L_{Si}	1	µm	Capture the emitter thickness.

1113 The value of k can be defined based upon whether depletion of the source occurs during
1114 the time scale of the simulation or not, whereas S can be taken from experimental estimations on
1115 the surface concentration like the ones given by Naumann et al. [104], Wilson et al. [32] and Snow
1116 et al. [69].

1117 As shown in Fig. 4.5, the consideration of a finite source leads to (1) less accumulation at
1118 the SiN_x/Si interface and, (2) depletion of the source within the timescale of the simulation.

1119 To understand the effect of individual variations of the parameters D_{SF}, S, k, E and h from
1120 the base case indicated in Table 5.2, we performed PID kinetics simulations using a finite source

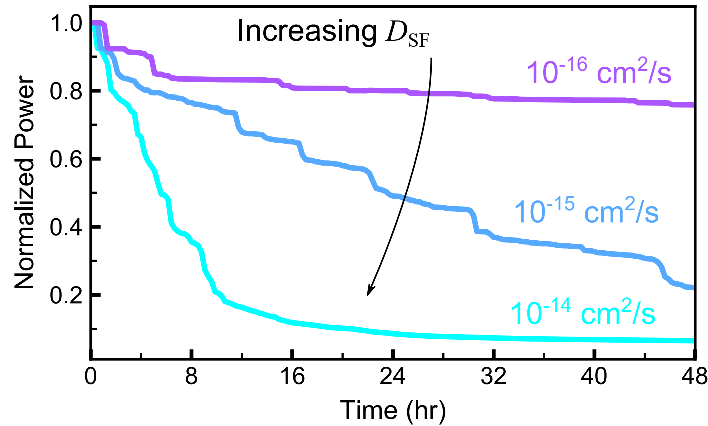

Figure 5.8: Simulated PID-kinetics as a function of D_{SF} (indicated by the color scale).

1121 boundary condition and varying one parameter at a time in logarithmic intervals.

1122 In Fig. 5.8, the simulated kinetics of PID-s is shown for different values of D_{SF}, indicated
1123 in color scale. As could be expected, larger values of D_{SF} result in a more rapid accumulation of Na
1124 at the *p*-*n* junction of the device leading to faster degradation rates. This is by far the parameter that
1125 induces the most significant variation in the degradation kinetics of p-Si PV modules. Depending
1126 on the quality of the initial wafer and the manufacturing quality control during the formation of the
1127 emitter, the number of SF defects can vary from device to device, leading to effective variations
1128 in D_{SF}. Furthermore, it is expected for multi-crystalline Si devices to have grain boundaries with
1129 different defect orientations, with respect to the typical 54° orientation of the {111} SF in mono-
1130 crystalline Si. Some of these orientations would lead to shorter SF path lengths to the emitter
1131 junction. This could explain difference on the effective D_{SF}, which would be averaged over the
1132 crystallite boundaries at the surface of the emitter.

1133 In Fig. 5.9 the simulated time series of PID is plotted for different values of the surface
1134 source concentration, S indicated by the color scale. It can be observed that even for a variation

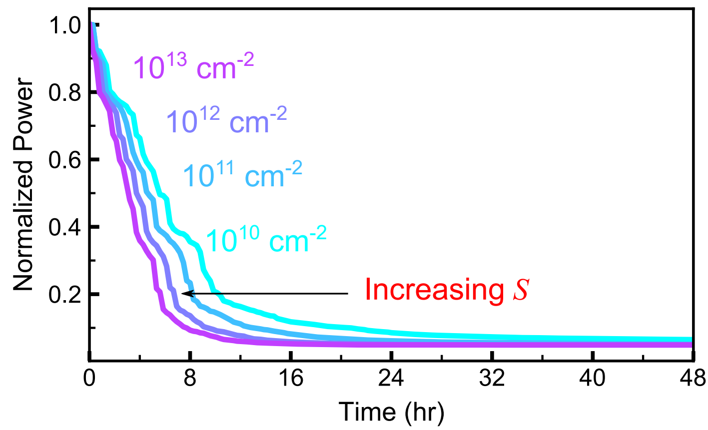

Figure 5.9: Simulated PID-kinetics as a function of the surface concentration of Na at the source S (indicated by the color scale).

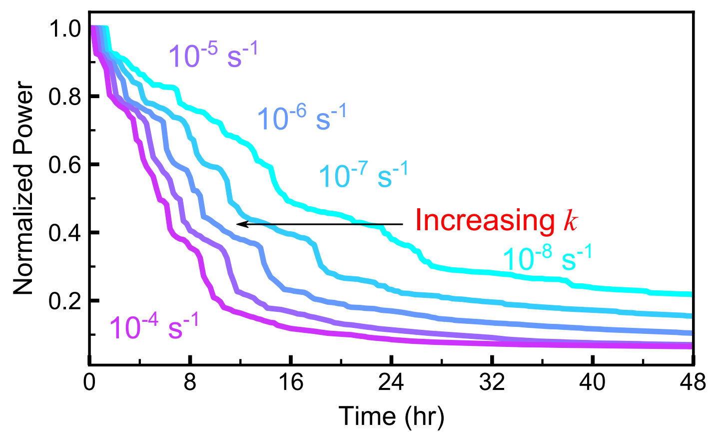

Figure 5.10: Simulated PID-kinetics as a function of the rate of ingress of Na at the source k (indicated by the color scale)

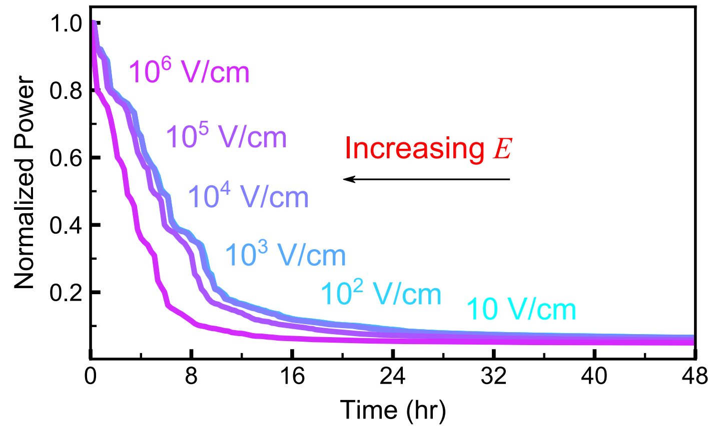

Figure 5.11: Simulated PID-kinetics as a function of the magnitude of the electric field in SiN_x E (indicated by the color scale).

1135 of three orders of magnitude in S, the equivalent time required to reach a 50 % degradation of the
1136 initial power output is still within the range of 4 to 8 hours. Nevertheless, the degradation reaches
1137 almost the same level, regardless of the value of S, after ~ 20 h of PID stress.

1138 In contrast, in Fig. 5.10 it is shown that the rate of ingress of Na to the SiN_x has a significant
1139 impact on the magnitude and the rate of degradation of the PV module. It can be seen that the
1140 time required to reach a 50 % degradation varies from around 16 h for $k = 10^{-8}\,\mathrm{s}^{-1}$, to ≈ 8 h for
1141 $k = 10^{-5}\,\mathrm{s}^{-1}$. An increase in the flux from the source leads to a larger accumulation of Na in
1142 the SiN_x film, compared with lower values of k. Since the magnitude of the segregation flux is
1143 dependent on the difference of the Na concentration at both sides of the SiN_x/Si interface, a larger
1144 value of the concentration at the SiN_x increases the magnitude of the flux to the Si emitter. This
1145 explains why larger values of k increase the rate and the magnitude of degradation of the module.

1146 As discussed in Sec. 1.4, it is expected that the magnitude of the electric field E in SiN_x
1147 determines the amount of drift of Na through the dielectric and hence, a reduction of E should
1148 translate to a decrease in the decay rate. In Fig. 5.11 the simulated PID time series of a PV modules

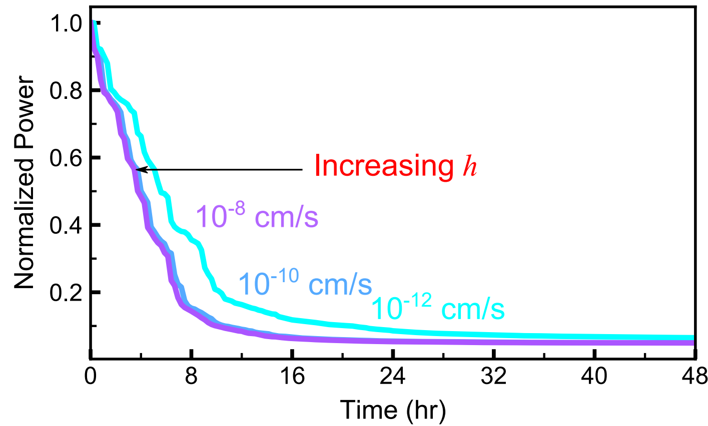

Figure 5.12: Simulated PID-kinetics as a function of the magnitude of the surface mass transfer coefficient h at the SiN_x/Si interface (indicated by the color scale).

is shown, as a function of E, indicated in color scale. It can be observed that, indeed, a reduction of the E from 10^6 to 10^5 MV/cm leads to a < 4 h delay in the time the device is expected to degrade 50 % with respect to the initial value. Nevertheless, variations in the degradation kinetics for for $E < 10^4$ MV/cm are minimal. This behavior is explained by the fact that, at 85 °C, the diffusion coefficient of Na^+ in SiN_x is such, that transit time can occur in less than 36 h for $E < 10^4$ MV/cm, as can be seen in Fig. 3.4. This indicates that it is likely that highly resistive SiN_x films preclude the fabrication of PID-robust devices. It might be possible that the energetic barrier for Na^+ diffusion in less resistive SiN_x can be larger compared to high resistivity SiN_x, leading to a decrease in the rate of decay with respect to the indicated in Fig. 5.11.

In Fig. 5.12, the variation in the simulated PID kinetics as a function of the surface mass transfer coefficient h at the SiN_x/Si interface is shown. It can be observed that for $h > 10^{-10}$ cm/s, the difference in the time series of PID becomes negligible. The effect of h is conflated with the relative values of D in the SiN_x film and in the SF, as well as with the relative Na concentrations at both sides of the SiN_x/Si interface.

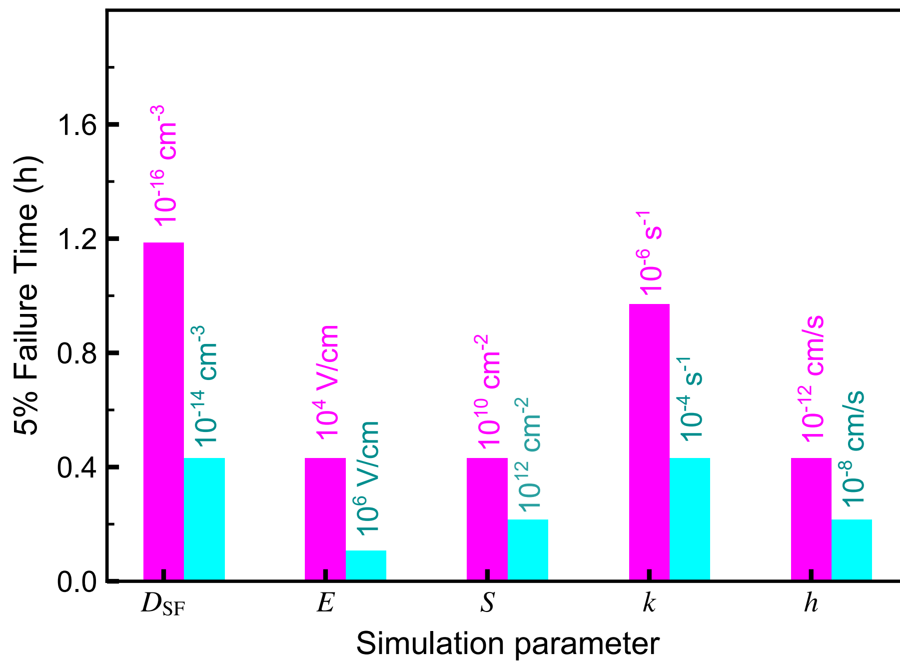

Figure 5.13: Estimated time required to reach a 5 % performance degradation in a p-Si PV module due to potential induced degradation as a function of (1) the diffusion coefficient of Na in the stacking fault D_{SF}, (2) the electric field in the SiN_x E, (3) the surface concentration of ions at the source S, (4) the rate of ingress of Na from the source k, (5) the segregation surface mass transfer coefficient at the SiN_x/Si interface h. For comparison, a "high" and a "low" value of each parameter is shown with a 2 orders of magnitude variation in each case.

1163 To quantitatively compare the effect of the variation in the transport parameters, we esti-
1164 mate the time required to incur in a 5 % decrease in the initial power output (τ_5) for each of the
1165 time series shown in Figs. 5.8, 5.9, 5.10, 5.11 and 5.12. The comparison is made for a two orders
1166 of magnitude variation of each parameter with respect to the base case shown in Tab. 5.2. The
1167 values are plotted in Fig. 5.13. It can be seen that τ_5 decreases almost 75 % when increasing E
1168 from 10^4 to 10^6 V/cm which is the largest percentage change between the five parameters. Nev-
1169 ertheless, it has has been shown that below 10^4 V/cm, diffusive transport dominates leading to a
1170 negligible change in the kinetics of PID-s, for the SiN_x composition analyzed in this work. The
1171 second largest change occurs when varying D_{SF} from 10^{-16} to 10^{-14} cm^2/s, which results in a
1172 ≈ 64 % reduction in τ_5. Similarly τ_5 drops ≈ 55 %, when increasing k from 10^{-6} to 10^{-4} s^{-1}.
1173 Finally, τ_5 drops ≈ 50 % when increasing S from 10^{10} to 10^{12} /cm^2, which is just about the same
1174 amount it decreases when varying h from 10^{-12} to 10^{-8} cm/s. These results indicate that control
1175 over the electric field in SiN_x is very important, particularly in film compositions that have lower
1176 Na diffusivities. Additionally the diffusion coefficient of Na remains a significant parameter which
1177 could be subject of improvement by using monocrystalline Si wafers and through optimization of
1178 the process of emitter diffusion [9]. A final remark is that, the considerable change in τ_5 introduced
1179 by the variation of k suggests that engineering the encapsulant/SiN_x interface might be a potential
1180 workaround to increase segregation at the polymer, and hence increase the robustness of the device
1181 against PID.

1182 ## 5.6 Summary

1183 We developed a framework to model PID-s degradation kinetics that describes the kinetics
1184 of shunt formation and the decay in the power output as a function of the diffusivity of Na in
1185 the in the PV module, surface concentration and rate of ingress of Na at the EVA/SiN_x interface,
1186 segregation surface mass transfer coefficient, and the string bias. This parametrization can be
1187 correlated with the bill of materials in the module. Extension to estimate the kinetics of R_{sh} decay
1188 is straightforward. We identified that the shunt conductivity around the *p*-*n* junction of the device
1189 must be above $10^{-3}\,S\,cm^{-1}$ in order to observe PID. Furthermore, we established an upper bound
1190 for the diffusivity of Na in the stacking fault on the order of $10^{-14}\,cm^2/s$, which suggests that
1191 diffusion occurs along the SF.

1192 We established that finite source simulations could be advantageous to avoid unphysical
1193 accumulation of Na across the interface. By simulating the effect of varying one parameter at a
1194 time, we were able to identify that D_{SF} has the largest impact on the kinetics of PID. This indicates
1195 that the crystallinity and number concentration of SF in the emitter can average to an effective
1196 diffusion coefficient. It is expected then, that quality control during the emitter formation could
1197 help decrease the susceptibility to PID. Notably, the kinetics of PID is very sensitive to the rate
1198 of ingress of Na in the SiN_x. This means that interface design between the encapsulant and SiN_x
1199 is very likely to reduce the impact of PID in Si PV modules, by increasing segregation to the
1200 encapsulant. We also identified that, for highly resistive SiN_x, the reduction of E has a limiting
1201 effect on PID, due to the large value of the diffusivity of Na associated to the Si-N composition we
1202 studied.

Overall, this framework has enabled us to identify the rate limiting processes in PID. Further fitting of the degradation time series to accelerated PID experiments will allow us to determine more accurate values on the parameter space. Our model provides a description of the PID-s physics which renders not only the time series of the power decay, but also the kinetics of Na transport and J-V characteristic of stressed devices. This will enable reference with multiple characterization techniques (e.g. BTS measurements, SIMS characterization, I-V characterization), to validate the sensitivity to the different components in the module and. Upon parameter refinement, this framework will be of use in the design of PID-robust PV modules.

Chapter 5, in part, is being prepared for submission in *IEEE Journal of Photovoltaics* under the title “Finite Element Simulation of Potential Induced Degradation Kinetics in p-Si Solar Modules” by E. Martinez-Loran. G. von Gastrow, J. Clenney, R. Meier, P. Bandaru, Mariana I. Bertoni, D.P. Fenning. The dissertation/thesis author was the primary investigator and author of this paper.

6 | Summary and Suggestions for Future Work

A framework for the characterization and modeling of potential-induced degradation has been developed for p-Si photovoltaic modules. The proposed methodology includes quantification methods to determine the transport kinetics of Na in the passivation layers of Si solar cells using measurement techniques that enable characterization at device operating temperatures. The advantage of this measurement is that it can provide a more accurate parametrization of ion kinetics with respect to the extrapolation of the diffusivities from measurements at higher temperature ranges, which can incur orders of magnitude variations in the estimated diffusion coefficient.

Transport in SiN_x films with index of refraction 1.89 (at 600 nm) reveals that anti-reflective coatings with this Si–N composition, are not an effective barrier against Na diffusion in silicon photovoltaic modules.

A numerical solution to the transport of charged species in dielectrics was developed which can describe the ingress of Na contamination in silicon photovoltaic modules. The advantage of the numerical solution is that: (1) it can solve Poison and Nernst-Planck's equations self consistently to completely describe the kinetics of Na transport for contamination levels consistent with PID,

(2) extension of the solution to stacks of materials can be implemented through first order kinetics segregation fluxes [96], (3) It allows to reference the numerical results with electrical measurements and other quantitative experimental techniques to characterize the concentration of Na ions (e.g. secondary-ion mass spectroscopy).

A complete framework to describe the kinetics of potential-induced degradation was proposed which uses transport simulations to estimate the resistivity profile of a metallic shunt in the emitter of a photovoltaic module. This model has allowed us to set an upper bound of $10^{-14}\,\mathrm{cm^2 s}$ (at 85 °C) on the diffusivity of Na in the Si emitter. This result indicates that bulk diffusion, which occurs with $D \approx 3 \times 10^{-19}\,\mathrm{cm^2/s}$ at the simulated temperature [109], is not the predominant mechanism in PID-prone devices. Instead, transport is dominated by diffusion through the SF as suggested by *ab-initio* studies by Ziebarth et al. [113].

6.1 Applications of PID kinetics quantification and modeling

The methodology developed to quantify the kinetics of Na transport in SiN_x is of interest to other device architectures and dielectric compositions. Determination of transport kinetics is applicable to other semiconductor architectures like perovskite PV devices, which are very attractive for solar energy harvesting [114].

The general goal of this modeling framework is to be able to parametrize PID-s in terms of the materials used in the photovoltaic module and the operating conditions. This model will provide guidance in the design of ion blocking layers that can reduce the ingress of Na to the emitter of the module by means of (1) reduction of the drift and, (2) interface design to increase segregation on the outermost layers of materials in the device.

6.2 Future work

6.2.1 Quantification of composition-dependent transport in SiN_x

Based on the voltage divider model, modification of the Si to N composition in SiN_x films impacts PID kinetics by changing the electrical resistivity of the film and hence, the magnitude of the electric field driving transport. Nevertheless, transport of Na can also be influenced by local electrostatic interactions determined by the coordination environment of $(N–Si–N)^-$ in the film [115]. To quantify this effect, the trapping corrected BTS method can be used to study sodium transport in SiN_x films as a function of Si to N composition. It would be expected that SiN_x of higher Si content [33] would experience a higher activation energy for diffusion.

6.2.2 Incorporation of environmental factors

To adequately reproduce accelerated testing protocols, incorporation of temperature- and humidity-activated resistivity [3] values is required. This could help elucidate whether transport in the polymer encapsulants can be enhanced by an electrochemical reaction at elevated water contents, in addition to the electrostatic considerations of this model.

PID kinetics simulations will be of use to better understand the applicability of accelerated testing protocols. Accelerated testing assumes long term damage can be characterized by continuous application of temperature, voltage and humidity stress to the PV modules. Under regular operation, such extreme conditions do not occur. Diurnal variations can be implemented on our transport modeling framework to account for realistic ingress of Na under conditions closer to field operation.

6.2.3 Three-dimensional considerations

The present model assumes that Na transport is predominantly occurring in the direction normal to the material interfaces which simplifies some of the derivations and saves computing resources. Nevertheless, three-dimensional extension can be easily implemented, and can provide further information on the effect of in-plane diffusion, especially in the context of interfacial oxide layers that might play a significant role in reducing the ingress of Na contamination to the Si emitter.

6.2.4 PID-recovery

The process of PID recovery has been reported experimentally in p-Si PV modules by means of the application of a thermal stress with and without the reversal of the electric field in the PV module [5, 11, 14, 15, 28, 35, 103, 116, 117]. While full PID recovery is usually not observed, the process remains poorly understood from a physical perspective.

The present model considers that transport of Na impurities in the Si emitter of PV devices is dominated by 1D diffusion along the direction normal to the SiN_x/Si interface. Under these conditions, the typical negative concentration gradients inside the silicon emitter preclude out-diffusion as proposed by Lausch et al. [11]. In the context of this model, we hypothesize that recovery could be possible for a specific combination of source concentrations and recovery electric fields. A full combinatorial analysis on the parameter space could shed light on such conditions. An alternative answer might arise from the three-dimensional consideration of transport kinetics, where out-diffusion to the bulk of Si might explain thermal PID recovery. In this sense, Density Functional Theory studies have shown that, once Na occupies interstitial positions in the

1294 SF, there is a large barrier to diffuse back into the bulk [112], which explains the irreversibility of
1295 this degradation mode.

1296 6.2.5 Incorporation of SiN_x trap kinetics

1297 In our trapping corrected BTS method we considered the effect of bulk traps in SiN_x cap-
1298 turing, driven by the applied voltage stress. The rate at which traps are filled is dependent on the
1299 magnitude of the applied field, and the energy position of the traps with respect to the conduction
1300 band edge of SiN_x as prescribed by Frenkel-Poole emission current [63]:

$$J = C_1 E \exp\left\{-\frac{q}{k_B T}\left[\phi_1 - \left(\frac{qE}{\pi\epsilon_0\epsilon_d}\right)^{1/2}\right]\right\}, \tag{6.1}$$

1301 where E is the electric field, ϕ_1 is the barrier height of the trap with respect to the conduction band
1302 edge, ϵ_d is the dynamic dielectric constant of SiN_x and the proportionality constant C_1 is a function
1303 of the density of the trapping centers.

1304 During operating conditions, the voltage differential in the SiN_x anti-reflective coating,
1305 albeit low, might be enough to fill a finite concentration of bulk traps with electrons leading to
1306 positive image charges in the semiconductor. Based upon the 1 V saturation flatband voltage shift
1307 (see Fig. 3.2) from our BTS measurements at $1\,\mathrm{MV\,cm^{-1}}$ and Eq. (6.1), we assumed that the
1308 concentration of occupied traps at $E = 10\,\mathrm{kV\,cm^{-1}}$ typically used for our simulations, will be at
1309 least two orders of magnitude less. Hence, we neglected the concentration of trapping centers in
1310 the computation of image charges in PID degradation kinetics. Nevertheless, this aspect could
1311 be of interest for SiN_x compositions with larger concentration of traps. To characterize this, we
1312 propose to fit ΔV_{FB} in SiN_x MIS capacitors without intentional Na contamination to the flatband
1313 voltage obtained by integration of Frenkel-Poole current in Eq. (6.1), to extract C_1 and ϕ_1. This

1314 will allow us to determine the extent of positive image charges in Na transport simulations, which
1315 will modify the electric potential at the SiN_x/Si interface and consequently Na accumulation and
1316 ingress to the Si emitter.

A | Derivation for the characteristic time for drift-diffusion

We defined the characteristic time for drift-diffusion as the solution to the equation

$$L = 2\sqrt{D\tau_c} + \mu E \tau_c$$

τ_c is then given by the solution to the quadratic equation

$$\mu^2 E^2 \tau_c^2 - 2(\mu E L + 2D)\tau_c + L^2 = 0, \tag{A.1}$$

which is given by

$$\tau_c = \frac{L}{\mu E} + \frac{2D}{\mu^2 E^2} \pm 2\frac{\sqrt{\mu E L D + D^2}}{\mu^2 E^2}. \tag{A.2}$$

Rearranging the terms within the square root term:

$$\tau_c = \frac{L}{\mu E} + \frac{2D}{\mu^2 E^2} \pm \frac{2D}{\mu^2 E^2}\left(1 + \frac{\mu E L}{D}\right)^{1/2}. \tag{A.3}$$

Equation (A.3) can be further simplified to

$$\tau_c = \frac{L}{\mu E} + \frac{2D}{\mu^2 E^2}\left[1 \pm \left(1 + \frac{\mu E L}{D}\right)^{1/2}\right]. \tag{A.4}$$

1324 Writing the mobility term explicitly ($\mu = qD/k_{\mathrm{B}}T$):

$$\tau_c = \frac{L}{D}\left(\frac{k_{\mathrm{B}}T}{qE}\right) + \frac{2}{D}\left(\frac{k_{\mathrm{B}}T}{qE}\right)^2 \left\{1 \pm \left[1 + \left(\frac{qE}{k_B T}\right)L\right]^{1/2}\right\}. \tag{A.5}$$

1325 Equation (A.5) can also be expressed in term of the thermal voltage $v_{\mathrm{th}} \equiv k_{\mathrm{B}}T/q$:

$$\tau_c = \frac{L}{D}\left(\frac{v_{\mathrm{th}}}{E}\right) + \frac{2}{D}\left(\frac{v_{\mathrm{th}}}{E}\right)^2 \left\{1 \pm \left[1 + \left(\frac{E}{v_{\mathrm{th}}}\right)L\right]^{1/2}\right\}. \tag{A.6}$$

1326 The solution to the equation (3.8) assumes that the drift flux μEC is in fact considerable
1327 with respect to the diffusive flux $-D\nabla^2 C$. Equation (A.6) depends on the inverse of E. This causes
1328 $\tau_c \to \infty$ as $E \to 0$, which is not physical because the diffusive term dominates as $E \to 0$. Then the
1329 solution needs to be given by the lowest bound of the time between (A.6) and the characteristic
1330 diffusion time L/D.

1331 # B | Derivation of the spatial part of Nernst-
1332 Planck equation in the weak form

1333 Behind scenes, the weak formulation of a PDE works by transforming the differential op-
1334 erator to a variational problem [81, 82, 118]. Discretization prescribes formulating the problem
1335 $L(x) = f$ in matrix form. The solution u in the vector space V is then given by:

$$Au = f. \tag{B.1}$$

1336 The function space V has the minimum requirements of being equipped with a norm $\|\cdot\|$ to compute
1337 distances within vectors, and we require that every Cauchy sequence in V converges to an element
1338 in the same space (Banach space) [119]. The variational formulation states that this problem is
1339 equivalent to finding u such that

$$[Au](v) = f(v) \tag{B.2}$$

1340 for all v in the vector space V. In the FEM, u are called *trial functions* and v are known as *test*
1341 *functions*. An additional requirement is placed on V so that for all test functions v^2 and $\|v^2\|$ have
1342 finite integrals over the volume (Sobolev space) [81].

1343 The finite-element-method approach to integrate the spatial part of the coupled Poisson-
1344 Nernst-Planck system with the finite element method is to write it in the variational formulation.

1345 The right hand side of Eq. (2.1) and Poisson's equation can be written in terms of trial

1346 functions

$$L_{\mathrm{NP}}[u_c] \equiv \nabla \cdot (D \nabla u_c) + \mu u_c \nabla \cdot \nabla u_p + \mu \nabla u_c \cdot \nabla \phi(u_p, t), \quad \text{(B.3a)}$$

$$L_{\mathrm{P}}[u_p] \equiv \nabla \cdot \nabla u_p + \frac{q}{\epsilon_{\mathrm{ins}}} u_c \quad \text{(B.3b)}$$

1347 where u_c, u_p are trial functions for the concentration and electric potential respectively, L_{NP} and

1348 L_{NP} are the differential operators for the spatial part of (2.1) and for Poisson's equation, respec-

1349 tively

1350 Multiplying L by the test function v and integrating over the volume Ω:

$$A_{\mathrm{NP}}(u,v) \equiv D \int_{\Omega} \nabla \cdot (\nabla u_c) v_c d\Omega + \mu \int_{\Omega} u_c \nabla \cdot \nabla u_p v_c d\Omega + \mu \int_{\Omega} \nabla u_c \cdot \nabla u_p v_c d\Omega \quad \text{(B.4a)}$$

$$A_{\mathrm{P}}(u,v) \equiv \int_{\Omega} \nabla \cdot \nabla u_p v_p d\Omega + \frac{q}{\epsilon_{\mathrm{ins}}} \int_{\Omega} u_c v_p d\Omega \quad \text{(B.4b)}$$

1351

1352 The order of the derivatives of Laplacian terms in (B.4) can be reduced by integrating by

1353 parts and using Gauss theorem (See Appendix D):

$$A_{\mathrm{NP}}(u,v) \equiv -D \int_{\Omega} \nabla u_c \cdot \nabla v_c d\Omega + D \int_{\partial\Omega} (\nabla u_c \cdot \hat{\mathbf{n}}) v_c ds - \mu \int_{\Omega} \nabla u_p \cdot \nabla (u_c v_c) \Omega$$
$$+ \mu \int_{\partial\Omega} (\nabla u_p \cdot \hat{\mathbf{n}}) u_c v_c ds + \mu \int_{\Omega} \nabla u_c \cdot \nabla u_p v_c d\Omega, \quad \text{(B.5)}$$

1354 for $A_{\mathrm{NP}}(u,v)$ and

$$A_{\mathrm{P}}(u,v) \equiv -\int_{\Omega} (\nabla u_p \cdot \nabla v_p) d\Omega + \int_{\partial\Omega} (\nabla u_p \cdot \hat{\mathbf{n}}) v_p ds + \frac{q}{\epsilon_{\mathrm{ins}}} \int_{\Omega} u_c v_p d\Omega \quad \text{(B.6)}$$

1355 for $A_{\mathrm{P}}(u,v)$.

Expanding $\nabla(u_c v_c) = u_c \nabla v_c + v_c \nabla u_c$ in (B.5):

$$A_{\mathrm{NP}}(u,v) \equiv -D\int_{\Omega} \nabla u_c \cdot \nabla v_c d\Omega + D\int_{\partial\Omega} (\nabla u_c \cdot \hat{\mathbf{n}})\, v_c ds - \mu \int_{\Omega} \nabla u_p \cdot u_c \nabla v_c \Omega$$
$$- \cancel{\mu \int_{\Omega} \nabla u_p \cdot v_c \nabla u_c \Omega} + \mu \int_{\partial\Omega} (\nabla u_p \cdot \hat{\mathbf{n}})\, u_c v_c ds + \cancel{\mu \int_{\Omega} \nabla u_c \cdot \nabla u_p v_c d\Omega},$$

The bilinear forms can now be written as

$$A_{\mathrm{NP}} = -D\int_{\Omega} \nabla u_c \cdot \nabla v_c d\Omega + D\int_{\partial\Omega} (\nabla u_c \cdot \hat{\mathbf{n}})\, v_c ds - \mu \int_{\Omega} u_c \nabla u_p \cdot \nabla v_c \Omega + \mu \int_{\partial\Omega} (\nabla u_p \cdot \hat{\mathbf{n}})\, u_c v_c ds \tag{B.7a}$$

$$A_{\mathrm{P}} = -\int_{\Omega} (\nabla u_p \cdot \nabla v_p)\, d\Omega + \int_{\partial\Omega} (\nabla u_p \cdot \hat{\mathbf{n}})\, v_p ds + \frac{q}{\epsilon_{\mathrm{ins}}} \int_{\Omega} u_c v_p d\Omega \tag{B.7b}$$

C | Derivation of the TR-BDF2 time-stepping in the weak form

We will use the results from Appendix B to derive the time stepping system in the variational form. We start by defining Equations (4.6) and (4.7) in terms of the trial functions for the concentration u_c and the electric potential u_p, followed by multiplication by the test functions v_c and v_p and subsequently, by integration within the simulation volume Ω [82].

For the TR step we have

$$\int_\Omega u_c^{n+\gamma} v_c d\Omega - \gamma \frac{\Delta t_n}{2} \int_\Omega \langle F^{n+\gamma}(u_c,u_p),(v_c,v_p)\rangle d\Omega = \int_\Omega u_c^n v_c d\Omega + \gamma \frac{\Delta t_n}{2} \int_\Omega \langle F^n(u_c,u_p),(v_c,v_p)\rangle d\Omega, \tag{C.1}$$

and for the BDF2 step

$$\int_\Omega u_c^{n+1} v_c d\Omega - \frac{1-\gamma}{2-\gamma}\Delta t_n \int_\Omega \langle F^{n+1}(u_c,v_c),(v_c,v_p)\rangle d\Omega = \frac{1}{\gamma(2-\gamma)} \int_\Omega u_c^{n+\gamma} v_c d\Omega - \frac{(1-\gamma)^2}{\gamma(2-\gamma)} \int_\Omega u_c^n v_c d\Omega, \tag{C.2}$$

where F refers to the spatial part of the problem $\partial C/\partial t = F(C,\phi,x)$, and we have defined the inner product

$$\langle F(u_c,u_p),(v_c,v_p)\rangle \equiv \overbrace{F_c(u_c,u_p)v_c}^{\text{Nernst-Planck}} + \underbrace{F_c(u_c,u_p)v_p}_{\text{Poisson}} \tag{C.3}$$

1369 Equations (C.1) and (C.2) can be expressed in terms of the linear forms (B.7).

1370 For the TR step

$$\int_\Omega u_c^{n+\gamma} v_c d\Omega - \gamma \frac{\Delta t_n}{2} \left(A_{\mathrm{NP}}^{n+\gamma} + A_{\mathrm{P}}^{n+\gamma} \right) = \int_\Omega u_c^n v_c d\Omega + \gamma \frac{\Delta t_n}{2} (A_{\mathrm{NP}}^n + A_{\mathrm{P}}^n),$$

1371 and for the BDF2 step

$$\int_\Omega u_c^{n+1} v_c d\Omega - \frac{1-\gamma}{2-\gamma} \Delta t_n \left(A_{\mathrm{NP}}^{n+1} + A_{\mathrm{P}}^{n+1} \right) = \frac{1}{\gamma(2-\gamma)} \int_\Omega u_c^{n+\gamma} v_c d\Omega - \frac{(1-\gamma)^2}{\gamma(2-\gamma)} \int_\Omega u_c^n v_c d\Omega.$$

1372

1373 # D | Writing the weak form of Laplacian terms

1374 Re-formatting the weak form for Laplacian terms $\nabla \cdot \nabla u$ is quite useful to reduce the order
1375 of the PDE and, to introduce Neumann boundary conditions. The starting equation for the weak
1376 form is

$$\int_{\Omega} \nabla \cdot (\nabla u) v d\Omega \tag{D.1}$$

1377 We use the result from taking the divergence of $v\nabla u$:

$$\nabla \cdot (v\nabla u) = v\nabla \cdot \nabla u + \nabla v \cdot \nabla u.$$

1378 to integrate by parts Eq. (D.1)

$$\int_{\Omega} \nabla \cdot (\nabla u) v d\Omega = \int_{\Omega} \nabla \cdot (v\nabla u) d\Omega - \int_{\Omega} (\nabla v \cdot \nabla u) d\Omega$$

1379 Applying the Gauss theorem to the first term on the RHS:

$$\int_{\Omega} \nabla \cdot (v\nabla u) d\Omega = \int_{\partial\Omega_D \cup \partial\Omega_N} (\nabla u \cdot \hat{\mathbf{n}})\, v ds, \tag{D.2}$$

1380 where $\partial\Omega_D \cup \partial\Omega_N$ is the union of the Dirichlet and Neumann surfaces. Typically, v is defined such
1381 that the integral over the Dirichlet part of the surface vanishes. Then

$$\int_{\Omega} \nabla \cdot (\nabla u) v d\Omega = -\int_{\Omega} (\nabla u \cdot \nabla v)\, d\Omega + \int_{\partial\Omega_N} (\nabla u \cdot \hat{\mathbf{n}})\, v ds. \tag{D.3}$$

1382 The Neumann BC $\mathbf{g} = \nabla u$ can then be imposed on the second term on the RHS of (D.3).

References

[1]D. C. Jordan and S. R. Kurtz, "Photovoltaic degradation rates—an analytical review", Progress in Photovoltaics: Research and Applications **21**, 12 (2013).

[2]M. Köntges, S. Kurtz, C. Packard, U. Jahn, K. A. Berger, K. Kato, T. Friesen, H. Liu, and M. V. Iseghem, *Review of failures of photovoltaic modules*, Report IEA-PVPS T13-01:2014 (International Energy Agency Photovoltaic Power Systems Programme, Mar. 2014).

[3]G. R. Mon and R. G. Ross, "Electrochemical degradation of amorphous-silicon photovoltaic modules", in Proc. 18th IEEE PVSC (1985), pp. 1142–1149.

[4]J. H. Wohlgemuth, M. Conway, and D. H. Meakin, "Reliability and performance testing of photovoltaic modules", in Conference Record of the Twenty-Eighth IEEE Photovoltaic Specialists Conference, Anchorage, AK, USA (2000), pp. 1483–1486.

[5]S. Pingel, O. Frank, M. Winkler, S. Daryan, T. Geipel, H. Hoehne, and J. Berghold, "Potential induced degradation of solar cells and panels", in 2010 35th IEEE Photovoltaic Specialists Conference, Honolulu, HI, USA (2010), pp. 002817–002822.

[6]R. Swanson, M. Cudzinovic, D. DeCeuster, V. Desai, J. Jürgens, N. Kaminar, W. Mulligan, L. Rodrigues-Barbarosa, D. Rose, D. Smith, A. Terao, and K. Wilson, "The surface polarization effect in high-efficiency silicon solar cells", in Proceedings of the 15th International Photovoltaic Science & Engineering Conference (2005), pp. 410–413.

[7]P. Hacke, K. Terwilliger, R. Smith, S. Glick, J. Pankow, M. Kempe, S. K. I. Bennett, and M. Kloos, "System voltage potential-induced degradation mechanisms in PV modules and methods for test", in 2011 37th IEEE Photovoltaic Specialists Conference, Seattle, WA, USA (2011), pp. 000814–000820.

[8]F. Ebneali, S. Tatapudi, G. TamizhMani, and Ieee, "Potential induced degradation of pre-stressed photovoltaic modules: influence of polarity, surface conductivity and temperature", in 2013 IEEE 39th Photovoltaic Specialists Conference (2013), pp. 1548–1553.

[9]V. Naumann, D. Lausch, A. Graff, M. Werner, S. Swatek, J. Bauer, A. Hahnel, O. Breitenstein, S. Grosser, J. Bagdahn, and C. Hagendorf, "The role of stacking faults for the formation of shunts during potential-induced degradation of crystalline Si solar cells", Physica Status Solidi-Rapid Research Letters **7**, 315 (2013).

[10]B. Jaeckel, M. Cosic, and J. Arp, "Investigation of c-Si modules degradation and recovery effect under high potentials: CV-PID", in 2014 IEEE 40th Photovoltaic Specialist Conference (PVSC), Denver, CO, USA (2014), pp. 937–942.

1415 [11]D. Lausch, V. Naumann, A. Graff, A. Hahnel, O. Breitenstein, C. Hagendorf, and J. Bagdahn, "Sodium outdiffusion from stacking faults as root cause for the recovery process of potential-induced degradation (PID)", in Proceedings of the 4th International Conference on Crystalline Silicon Photovoltaics, Vol. 55, edited by A. Weeber, A. Aberle, R. Brendel, A. Cuevas, S. Glunz, G. Hahn, J. Poortmans, P. J. Ribeyron, and R. Sinton, Energy Procedia (2014), pp. 486–493.

1420 [12]V. Naumann, D. Lausch, A. Hähnel, J. Bauer, O. Breitenstein, A. Graff, M. Werner, S. Swatek, S. Großer, J. Bagdahn, and C. Hagendorf, "Explanation of potential-induced degradation of the shunting type by Na decoration of stacking faults in Si solar cells", Sol. Energy Mater. Sol. Cells **120**, 383 (2014).

1424 [13]V. Naumann, D. Lausch, A. Hähnel, O. Breitenstein, and C. Hagendorf, "Nanoscopic studies of 2D-extended defects in silicon that cause shunting of Si-solar cells", Physica Status Solidi (c) **12**, 1103 (2015).

1427 [14]M. B. Koentopp, M. Krober, and C. Taubitz, "Toward a PID test standard: understanding and modeling of laboratory tests and field progression", IEEE J. Photovolt. **6**, 252 (2016).

1429 [15]A. Schulze, M. B. Koentopp, and C. Taubitz, "A drift and diffusion model for PID-s in solar modules", IEEE J. Photovolt. **10**, 1 (2020).

1431 [16]N. G. Dhere, N. S. Shiradkar, and E. Schneller, "Evolution of leakage current paths in MC-Si PV modules from leading manufacturers undergoing high-voltage bias testing", IEEE J. Photovolt. **4**, 654 (2014).

1434 [17]M. Schütze, M. Junghänel, M. B. Koentopp, S. Cwikla, S. Friedrich, J. W. Müller, and P. Wawer, "Laboratory study of potential induced degradation of silicon photovoltaic modules", in 2011 37th IEEE Photovoltaic Specialists Conference, Seattle, WA, USA (2011), pp. 000821–000826.

1437 [18]P. Hacke, M. Kempe, K. Terwilliger, S. Glick, N. Call, S. Johnston, and S. Kurtz, "Characterization of multicrystalline silicon modules with system bias voltage applied in damp heat", in Presented at the 25th European Photovoltaic Solar Energy Conference and Exhibition, 6-10 September 2010 (2010), pp. 3760–3765.

1441 [19]V. Naumann, D. Lausch, S. Großer, M. Werner, S. Swatek, C. Hagendorf, and J. Bagdahn, "Microstructural analysis of crystal defects leading to potential-induced degradation (PID) of Si solar cells", in PV Asia Pacific Conference 2012, Vol. 33, Energy Procedia (2013), pp. 76–83.

1445 [20]D. E. Carlson, R. Romero, F. Willing, D. Meakin, L. Gonzalez, R. Murphy, H. R. Moutinho, and M. Al-Jassim, "Corrosion effects in thin-film photovoltaic modules", Prog. Photovoltaics Res. Appl. **11**, 377 (2003).

1448 [21]P. Hacke, R. Smith, K. Terwilliger, G. Perrin, B. Sekulic, and S. Kurtz, "Development of an IEC test for crystalline silicon modules to qualify their resistance to system voltage stress", Progress in Photovoltaics **22**, 775 (2014).

1451 [22]Z. Boksay, M. Varga, and A. Wikby, "Surface conductivity of leached glass", J. Non-Cryst. Solids **17**, 349 (1975).

1453 [23]S. Jonai and A. Masuda, "Origin of Na causing potential-induced degradation for p-type crystalline Si photovoltaic modules", AIP Adv. **8**, 115311 (2018).

1455 [24]M. Schütze, M. Junghänel, O. Friedrichs, R. Wichtendahl, M. Scherff, J. Müller, and P. Wawer,
1456 "Investigations of potential induced degradation of silicon photovoltaic modules", in 26th Euro-
1457 pean Photovoltaic Solar Energy Conference and Exhibition, Hamburg (2011), pp. 3097–3102.

1458 [25]V. Naumann, D. Lausch, and C. Hagendorf, "Sodium decoration of PID-s crystal defects af-
1459 ter corona induced degradation of bare silicon solar cells", in 5th International Conference on
1460 Silicon Photovoltaics, Silicon PV 2015, Vol. 77, Energy Procedia (2015), pp. 397–401.

1461 [26]J. Kapur, K. M. Stika, C. S. Westphal, J. L. Norwood, and B. Hamzavytehrany, "Prevention of
1462 potential-induced degradation with thin ionomer film", IEEE J. Photovolt. **5**, 219 (2015).

1463 [27]V. Naumann, K. Ilse, and C. Hagendorf, "On the discrepancy between leakage currents and
1464 potential-induced degradation of cristalline silicon modules", in 28th European Photovoltaic
1465 Solar Energy Conference and Exhibition, Paris, France (2013), pp. 2994–2997.

1466 [28]S. Koch, J. Berghold, B. Abdullah, C. Hinz, and P. Grunow, "Prediction model for potential
1467 induced degradation effects on crystalline silicon cells", in 29th European Photovoltaic Solar
1468 Energy Conference and Exhibition, Amsterdam (2014), pp. 3327–3333.

1469 [29]C. Taubitz, M. Schütze, M. Kröber, and M. B. Köntopp, "Potential induced degradation: model
1470 calculations and correlation between laboratory tests and outdoor occurrence", in 29th Euro-
1471 pean Photovoltaic Solar Energy Conference and Exhibition, Amsterdam, Netherlands (2014),
1472 pp. 2490–2494.

1473 [30]L. Svob, "Solubility and diffusion coefficient of sodium and potassium in silicon", Solid-State
1474 Electron. **10**, 991 (1967).

1475 [31]V. M. Korol, V. P. Astakhov, S. A. Vedenyapin, and A. V. Zastavnoi, "Formation of a donor
1476 profile in silicon upon simultaneous implantation of phosphorus and sodium ions", Journal of
1477 Surface Investigation-X-Ray Synchrotron and Neutron Techniques **5**, 358 (2011).

1478 [32]M. Wilson, A. Savtchouk, P. Edelman, D. Marinskiy, and J. Lagowski, "Drift characteristics of
1479 mobile ions in SiN_x films and solar cells", Sol. Energy Mater. Sol. Cells **142**, 102 (2015).

1480 [33]A. K. Sinha and T. E. Smith, "Electrical properties of Si-N films deposited on silicon from
1481 reactive plasma", J. Appl. Phys. **49**, 2756 (1978).

1482 [34]H. Nagel, M. Glatthaar, and S. Glunz, "Quantitative assessment of the local leakage current in
1483 PV modules for degradation prediction", in 31st European Photovoltaic Solar Energy Confer-
1484 ence and Exhibition, Hamburg, Germany (2013), pp. 1825–1829.

1485 [35]A. Masuda, M. Akitomi, M. Inoue, K. Okuwaki, A. Okugawa, K. Ueno, T. Yamazaki, and
1486 K. Hara, "Microscopic aspects of potential-induced degradation phenomena and their recovery
1487 processes for p-type crystalline Si photovoltaic modules", Curr. Appl Phys. **16**, 1659 (2016).

1488 [36]P. Hacke, R. Smith, K. Terwilliger, S. Glick, D. Jordan, S. Johnston, M. Kempe, and S. Kurtz,
1489 "Acceleration factor determination for potential-induced degradation in crystalline silicon PV
1490 modules", in 2013 ieee international reliability physics symposium, International Reliability
1491 Physics Symposium (2013).

1492 [37]W. Oh, S. Bae, S. I. Chan, H. S. Lee, D. Kim, and N. Park, "Field degradation prediction of po-
1493 tential induced degradation of the crystalline silicon photovoltaic modules based on accelerated
1494 test and climatic data", Microelectron. Reliab. **76**, 596 (2017).

1495 [38]P. Hacke, S. Spataru, K. Terwilliger, G. Perrin, S. Glick, S. Kurtz, and J. Wohlgemuth, "Accel-
1496 erated testing and modeling of potential-induced degradation as a function of temperature and
1497 relative humidity", IEEE J. Photovolt. **5**, 1549 (2015).

1498 [39]D. Lausch, V. Naumann, O. Breitenstein, J. Bauer, A. Graff, J. Bagdahn, and C. Hagendorf,
1499 "Potential-induced degradation (PID): introduction of a novel test approach and explanation of
1500 increased depletion region recombination", IEEE J. Photovolt. **4**, 834 (2014).

1501 [40]M. Bahr and K. Lauer, "Analysis of activation energies and decay-time constants of potential-
1502 induced degraded crystalline silicon solar cells", in 5th International Conference on Silicon
1503 Photovoltaics, SiliconPV 2015, Vol. 77, edited by G. Hahn, Energy Procedia (2015), pp. 2–7.

1504 [41]M. A. Islam, M. Hasanuzzaman, and N. Abd Rahim, "A comparative investigation on in-situ and
1505 laboratory standard test of the potential induced degradation of crystalline silicon photovoltaic
1506 modules", Renewable Energy **127**, 102 (2018).

1507 [42]J. V. Dalton and J. Drobek, "Structure and sodium migration in silicon nitride films", J. Elec-
1508 trochem. Soc. **115**, 865 (1968).

1509 [43]T. E. Burgess, J. C. Baum, F. M. Fowkes, R. Holmstrom, and G. A. Shirn, "Thermal diffusion of
1510 sodium in silicon nitride shielded silicon oxide films", J. Electrochem. Soc. **116**, 1005 (1969).

1511 [44]B. Yurash and B. E. Deal, "A method for determining sodium content of semiconductor pro-
1512 cessing materials", J. Electrochem. Soc. **115**, 1191 (1968).

1513 [45]E. Yon, W. H. Ko, and A. B. Kuper, "Sodium distribution in thermal oxide on silicon by radio-
1514 chemical and MOS analysis", IEEE Trans. Electron Devices **ED-13**, 276 (1966).

1515 [46]R. J. Kriegler and T. F. Devenyi, "Direct measurement of Na^+ ion mobility in SiO_2 films", Thin
1516 Solid Films **36**, 435 (1976).

1517 [47]J. P. Stagg, "Drift mobilities of Na^+ and K^+ ions in SiO_2 films", Appl. Phys. Lett. **31**, 532
1518 (1977).

1519 [48]G. Greeuw and J. F. Verwey, "The mobility of Na^+, Li^+, and K^+ ions in thermally grown SiO_2
1520 films", J. Appl. Phys. **56**, 2218 (1984).

1521 [49]B. E. Deal, P. J. Fleming, and P. L. Castro, "Electrical properties of vapor-deposited silicon
1522 nitride and silicon oxide films on silicon", J. Electrochem. Soc. **115**, 300 (1968).

1523 [50]A. L. S. Loke, C. Ryu, C. P. Yue, J. S. H. Cho, and S. S. Wong, "Kinetics of copper drift in
1524 PECVD dielectrics", IEEE Electron Device Lett. **17**, 549 (1996).

1525 [51]F. Lanckmans and K. Maex, "Use of a capacitance voltage technique to study copper drift dif-
1526 fusion in (porous) inorganic low-k materials", Microelectron. Eng. **60**, Materials for Advanced
1527 Metallization, 125 (2002).

1528 [52]R. S. Bonilla and P. R. Wilshaw, "Potassium ions in SiO_2: electrets for silicon surface passiva-
1529 tion", J. Phys. D: Appl. Phys. **51**, 025101 (2017).

1530 [53]K. J. Weber and H. Jin, "Improved silicon surface passivation achieved by negatively charged
1531 silicon nitride films", Appl. Phys. Lett. **94**, 063509 (2009).

1532 [54]G. v. Gastrow, J. Scharf, J. Clenney, E. M. Loran, R. Meier, M. I. Bertoni, and D. P. Fenning,
1533 "Evaluation of carrier trapping in SiN_x towards ion migration measurements", in 2019 IEEE
1534 46th Photovoltaic Specialists Conference (PVSC), Chicago, IL, USA (2019), pp. 2017–2020.

1535 [55]D. A. Buchanan and D. Felnhofer, “Defects in high-k gate dielectric stacks”, in, edited by E.
1536 Gusev (Springer, 2006) Chap. On the Characterization of Electronically Active Defects in High-
1537 *k* Gate Dielectrics, pp. 41–59.

1538 [56]E. H. Nicollian and J. R. Brews, *MOS (metal oxide semiconductor) physics and technology*
1539 (Wiley, 1982).

1540 [57]R. W. Balluffi, S. M. Allen, and W. C. Carter, *Kinetics of materials* (Wiley, 2005).

1541 [58]D. K. Jaiswal, A. Kumar, and R. R. Yadav, “Analytical solution to the one-dimensional advection-
1542 diffusion equation with temporally dependent coefficients”, J. Water Resour. Prot., 76 (2011).

1543 [59]A. Piccirillo, “Physical-electrical properties of silicon nitride deposited by PECVD on III–V
1544 semiconductors”, J. Electrochem. Soc. **137**, 3910 (1990).

1545 [60]M. Junghänel, A. Kux, M. Schädel, and M. Scherff, “Solar cell, solar cell manufacturing method
1546 and testing method”, EN, U.S. pat. US 2011/0308602 A1 (Dec. 22, 2011).

1547 [61]R. Winter, J. Ahn, P. C. McIntyre, and M. Eizenberg, “New method for determining flat-band
1548 voltage in high mobility semiconductors”, J. Vac. Sci. Technol., B **31**, 030604 (2013).

1549 [62]G. von Gastrow, E. Martinez-Loran, J. Scharf, J. Clenney, R. Meier, P. Bandaru, M. I. Bertoni,
1550 and D. P. Fenning, “Quantification of sodium ion migration in SiN_x by flatband-potential mon-
1551 itoring at device operating temperatures”, Phys. Status Solidi A. (2020).

1552 [63]S. M. Sze, “Current transport and maximum dielectric strength of silicon nitride films”, J. Appl.
1553 Phys. **38**, 2951 (1967).

1554 [64]D. J. DiMaria, “The properties of electron and hole traps in thermal silicon dioxide layers grown
1555 on silicon”, in The Physics of SiO_x and its Interfaces: International Topical Conference on
1556 the Physics of SiO_2 and Its Interfaces Held at the IBM Thomas J. Waston Research Center,
1557 Yorktown Heights, New York, USA, edited by S. T. Pantelides (1978), pp. 160–178.

1558 [65]T. L. Chu, J. R. Szedon, and C. H. Lee, “The preparation and C-V characteristics of Si–Si_3N_4
1559 and Si–SiO_2–Si_3N_4 structures”, Solid-State Electron. **10**, 897 (1967).

1560 [66]G. J. M. Janssen, M. K. Stodolny, B. B. Van Aken, J. Löffler, M. W. P. E. Lamers, K. J. J.
1561 Tool, and I. G. Romijn, “Minimizing the polarization-type potential-induced degradation in
1562 PV modules by modification of the dielectric antireflection and passivation stack”, IEEE J.
1563 Photovolt. **9**, 608 (2019).

1564 [67]W. D. Kingery, H. K. Bowen, and R. Uhlmann D, *Introduction to ceramics* (John Wiley & Sons,
1565 New York, 1976), p. 1056.

1566 [68]P. Hacke, R. Smith, K. Terwilliger, S. Glick, D. Jordan, S. Johnston, M. Kempe, and S. Kurtz,
1567 “Testing and analysis for lifetime prediction of crystalline silicon PV modules undergoing
1568 degradation by system voltage stress”, in 2012 38th IEEE Photovoltaic Specialists Conference,
1569 Austin, TX, USA, Vol. 3 (2012), pp. 246–253.

1570 [69]E. H. Snow, A. S. Grove, B. E. Deal, and C. T. Sah, “Ion transport phenomena in insulating
1571 films”, J. Appl. Phys. **36**, 1664 (1965).

1572 [70]C. T. Naber, “A method for reducing mobile electric charge in MNOS structures”, J. Elec-
1573 trochem. Soc. **116**, 1282 (1969).

1574 [71]M. Kuhn and D. J. Silversmith, "Ionic contamination and transport of mobile ions in MOS
1575 structures", J. Electrochem. Soc. **118**, 966 (1971).

1576 [72]T. W. Hickmott, "The use of thermally stimulated ionic currents with a hyperbolic heating rate
1577 to measure sodium motion in rf-sputtered SiO_x films", Appl. Phys. Lett. **22**, 267 (1973).

1578 [73]P. K. Nauta and M. W. Hillen, "Investigation of mobile ions in MOS structures using the TSIC
1579 method", J. Appl. Phys. **49**, 2862 (1978).

1580 [74]J. Oh, B. Dauksher, S. Bowden, G. Tamizhmani, P. Hacke, and J. D'Amico, "Further studies on
1581 the effect of SiN_x refractive index and emitter sheet resistance on potential-induced degrada-
1582 tion", IEEE J. Photovolt. **7**, 437 (2017).

1583 [75]S. P. Harvey, J. A. Aguiar, P. Hacke, H. Guthrey, S. Johnston, and M. Al-Jassim, "Sodium ac-
1584 cumulation at potential-induced degradation shunted areas in polycrystalline silicon modules",
1585 IEEE J. Photovolt. **6**, 1440 (2016).

1586 [76]S. P. Harvey, J. Moseley, A. Norman, A. Stokes, B. Gorman, P. Hacke, S. Johnston, and M.
1587 Al-Jassim, "Investigating PID shunting in polycrystalline silicon modules via multiscale, mul-
1588 titechnique characterization", Progress in Photovoltaics **26**, 377 (2018).

1589 [77]A. Golovnev and S. Trimper, "Exact solution of the Poisson-Nernst-Planck equations in the
1590 linear regime", J. Chem. Phys. **131**, 114903 (2009).

1591 [78]A. Golovnev and S. Trimper, "Steady state solution of the Poisson–Nernst–Planck equations",
1592 Phys. Lett. A **374**, 2886 (2010).

1593 [79]A. Golovnev and S. Trimper, "Analytical solution of the Poisson-Nernst-Planck equations in
1594 the linear regime at an applied DC-voltage", J. Chem. Phys. **134**, 154902 (2011).

1595 [80]M. Pabst, "Analytical solution of the Poisson-Nernst-Planck equations for an electrochemical
1596 system close to electroneutrality", J. Chem. Phys. **140**, 224113 (2014).

1597 [81]K. Bathe, *Finite element procedures* (Prentice Hall, 2006).

1598 [82]A. Logg, K.-A. Mardal, G. N. Wells, et al., *Automated solution of differential equations by the
1599 finite element method* (Springer, 2012).

1600 [83]R. E. Bank, W. M. Coughran, W. Fichtner, E. H. Grosse, D. J. Rose, and R. K. Smith, "Transient
1601 simulation of silicon devices and circuits", IEEE Trans. Comput.-Aided Design Integr. Circuits
1602 Syst. **4**, 436 (1985).

1603 [84]M. J. Johnson and C. L. Gardner, *An interface method for semiconductor process simulation*,
1604 edited by W. M. Coughran, J. Cole, P. Llyod, and J. K. White, Vol. 58, The IMA Volumes in
1605 Mathematics and its Applications (Springer New York, 1994), pp. 33–47.

1606 [85]M. E. Hosea and L. F. Shampine, "Analysis and implementation of TR-BDF2", Appl. Numer.
1607 Math. **20**, Method of Lines for Time-Dependent Problems, 21 (1996).

1608 [86]L. Bonaventura and A. D. Rocca, "Unconditionally strong stability preserving extensions of the
1609 TR-BDF2 method", J. Sci. Comput. **70**, 859 (2016).

1610 [87]D. Britz, O. Østerby, and J. Strutwolf, "Damping of Crank–Nicolson error oscillations", Com-
1611 put. Biol. Chem. **27**, 253 (2003).

1612 [88]M. S. Alnæs, J. Blechta, J. Hake, A. Johansson, B. Kehlet, A. Logg, C. Richardson, J. Ring,
1613 M. E. Rognes, and G. N. Wells, "The FEniCS project version 1.5", Archive of Numerical Soft-
1614 ware **3** (2015).

1615 [89]A. Logg and G. N. Wells, "DOLFIN: automated finite element computing", ACM Trans. Math.
1616 Software **37** (2010).

1617 [90]A. Logg, G. N. Wells, and J. Hake, "DOLFIN: a C++/Python Finite Element Library", in *Auto-*
1618 *mated solution of differential equations by the finite element method, volume 84 of lecture notes*
1619 *in computational science and engineering*, edited by A. Logg, K.-A. Mardal, and G. N. Wells
1620 (Springer, 2012) Chap. 10.

1621 [91]R. C. Kirby and A. Logg, "A compiler for variational forms", ACM Trans. Math. Software **32**
1622 (2006).

1623 [92]A. Logg, K. B. Ølgaard, M. E. Rognes, and G. N. Wells, "FFC: the FEniCS Form Compiler", in
1624 *Automated solution of differential equations by the finite element method, volume 84 of lecture*
1625 *notes in computational science and engineering*, edited by A. Logg, K.-A. Mardal, and G. N.
1626 Wells (Springer, 2012) Chap. 11.

1627 [93]K. B. Ølgaard and G. N. Wells, "Optimisations for quadrature representations of finite element
1628 tensors through automated code generation", ACM Trans. Math. Software **37** (2010).

1629 [94]M. S. Alnæs, A. Logg, K. B. Ølgaard, M. E. Rognes, and G. N. Wells, "Unified form language: a
1630 domain-specific language for weak formulations of partial differential equations", ACM Trans.
1631 Math. Software **40** (2014).

1632 [95]G. H. Frischat, "Sodium diffusion in SiO_2 glass", J. Am. Ceram. Soc. **51**, 528 (1968).

1633 [96]D. A. Antoniadis, "Impurity redistribution in SiO_2-Si during oxidation: a numerical solution
1634 including interfacial fluxes", J. Electrochem. Soc. **126**, 1939 (1979).

1635 [97]V. M. Korol, "Sodium-ion implantation into silicon", Physica Status Solidi a-Applied Research
1636 **110**, 9 (1988).

1637 [98]J. Yang, W. He, F. Wang, C. Chen, H. Yang, H. Wang, M. Ding, and S. Zhang, "Diffusion and
1638 drift of sodium ions in PID-affected mono-crystalline silicon solar modules", in 2018 IEEE 7th
1639 World Conference on Photovoltaic Energy Conversion (WCPEC) Waikoloa Village, HI, USA
1640 (2018), pp. 1081–1085.

1641 [99]P. Hacke, K. Terwilliger, S. Glick, R. Smith, G. Perrin, S. Kurtz, N. Bosco, and J. Wohlgemuth,
1642 "Application of the terrestrial photovoltaic module accelerated test-to-failure protocol", in 2014
1643 IEEE 40th Photovoltaic Specialist Conference (PVSC), Denver, CO, USA (2014), pp. 930–936.

1644 [100]S. Spataru, P. Hacke, D. Sera, C. Packard, T. Kerekes, and R. Teodorescu, "Temperature-
1645 dependency analysis and correction methods of in situ power-loss estimation for crystalline
1646 silicon modules undergoing potential-induced degradation stress testing", Progress in Photo-
1647 voltaics **23**, 1536 (2015).

1648 [101]P. Hacke, K. Terwilliger, S. Glick, G. Tamizhmani, S. Tatapudi, C. Stark, S. Koch, T. Weber,
1649 J. Berghold, S. Hoffmann, M. Koehl, S. Dietrich, M. Ebert, and G. Mathiak, "Interlaboratory
1650 study to determine repeatability of the damp-heat test method for potential-induced degradation
1651 and polarization in crystalline silicon photovoltaic modules", IEEE J. Photovolt. **5**, 94 (2015).

1652 [102]W. Luo, P. Hacke, J. P. Singh, J. Chai, Y. Wang, S. Ramakrishna, A. G. Aberle, and Y. S.
1653 Khoo, "In-situ characterization of potential-induced degradation in crystalline silicon photo-
1654 voltaic modules through dark i–v measurements", IEEE J. Photovolt. **7**, 104 (2017).

1655 [103]C. Taubitz, M. Kröber, M. Schütze, and M. B. Köntopp, "Kinetic description and modeling of
1656 potential induced degradation", in 28th European Photovoltaic Solar Energy Conference and
1657 Exhibition, Paris, France (2013), pp. 3321–3323.

1658 [104]V. Naumann, C. Hagendorf, S. Grosser, M. Werner, and J. Bagdahn, "Micro structural root
1659 cause analysis of potential induced degradation in c-Si solar cells", in SiliconPV: April 03-05,
1660 Vol. 27, Energy Procedia (2012), pp. 1–6.

1661 [105]H. Nagel, A. Metz, and K. Wangemann, "Crystalline si solar cells and modules featuring ex-
1662 cellent stability against potential-induced degradation", in 26th European Photovoltaic Solar
1663 Energy Conference and Exhibition, Hamburg, Germany (2011), pp. 3107–3112.

1664 [106]T. M. Kuan, C. C. Huang, L. G. Wu, Y. C. Chan, and C. Y. Yu, "Process optimization for poten-
1665 tial induced degradation improvement on cell level", in 2013 ieee 39th photovoltaic specialists
1666 conference, tampa, fl, usa, IEEE Photovoltaic Specialists Conference (2013), pp. 2224–2226.

1667 [107]T. Niewelt, A. Richter, T. C. Kho, N. E. Grant, R. S. Bonilla, B. Steinhauser, J.-I. Polzin, F.
1668 Feldmann, M. Hermle, J. D. Murphy, S. P. Phang, W. Kwapil, and M. C. Schubert, "Taking
1669 monocrystalline silicon to the ultimate lifetime limit", Sol. Energy Mater. Sol. Cells **185**, 252
1670 (2018).

1671 [108]P. P. Altermatt, J. O. Schumacher, A. Cuevas, M. J. Kerr, S. W. Glunz, R. R. King, G. Heiser, and
1672 A. Schenk, "Numerical modeling of highly doped Si:P emitters based on Fermi–Dirac statistics
1673 and self-consistent material parameters", J. Appl. Phys. **92**, 3187 (2002).

1674 [109]J. Clenney, R. Meier, E. Martinez-Loran, G. von Gastrow, D. P. Fenning, and M. Bertoni, "In-
1675 sights into na^+ diffusion in silicon cells under PV operating conditions", Sol. Energy Mater Sol.
1676 (To be submitted), To be submitted (2020).

1677 [110]F. Pedregosa, G. Varoquaux, A. Gramfort, V. Michel, B. Thirion, O. Grisel, M. Blondel, P.
1678 Prettenhofer, R. Weiss, V. Dubourg, J. Vanderplas, A. Passos, D. Cournapeau, M. Brucher,
1679 M. Perrot, and E. Duchesnay, "Scikit-learn: machine learning in Python", Journal of Machine
1680 Learning Research **12**, 2825 (2011).

1681 [111]S. Glantz and B. Slinker, *Primer of applied regression & analysis of variance* (McGraw-Hill
1682 Education, 2012).

1683 [112]J.-S. Park and M. K. Y. Chan, "Mechanism of Na accumulation at extended defects in Si from
1684 first-principles", J. Appl. Phys. **123**, 161560 (2018).

1685 [113]B. Ziebarth, M. Mrovec, C. Elsässer, and P. Gumbsch, "Potential-induced degradation in solar
1686 cells: Electronic structure and diffusion mechanism of sodium in stacking faults of silicon", J.
1687 Appl. Phys. **116**, 093510 (2014).

1688 [114]H. J. Snaith, "Present status and future prospects of perovskite photovoltaics", Nat. Mater. **17**,
1689 372 (2018).

1690 [115]J. W. Osenbach and S. S. Voris, "Sodium diffusion in plasma-deposited amorphous oxygen-
1691 doped silicon nitride (a-SiON:H) films", J. Appl. Phys. **63**, 4494 (1988).

[116]M. Schwark, K. Berger, R. Ebner, G. Ujvari, C. Hirschl, L. Neumaier, and W. Muhleisen, "Investigation of potential induced degradation (PID) of solar modules from different manufacturers", in IECON 2013 - 39th Annual Conference of the IEEE Industrial Electronics Society, Vienna, Austria, IEEE Industrial Electronics Society (2013), pp. 8090–8097.

[117]A. Masuda, Y. Hara, and S. Jonai, "Consideration on Na diffusion and recovery phenomena in potential-induced degradation for crystalline Si photovoltaic modules", Japanese Journal of Applied Physics **55**, 5 (2016).

[118]R. Burden and J. Faires, *Numerical analysis* (Brooks/Cole, Cengage Learning, 2011).

[119]M. Markin, *Elementary functional analysis*, De Gruyter Textbook (De Gruyter, 2018).